Annual Report for 1990
on NASA Grant NAGW-1983

Mapping Regional Freeze/Thaw Patterns with Satellite Microwave Radiometry

Submitted by: Anthony W. England, Principal Investigator
Brian Zuerndorfer, Graduate Student
John F. Galantowicz, Graduate Student
M. Craig Dobson, Co-Investigator
Fawwaz T. Ulaby, Co-Investigator

The Radiation Laboratory
Department of Electrical Engineering
and Computer Science
The University of Michigan
Ann Arbor, Michigan 48109-2122
(313)-763-5534

Period of Performance: January 1, 1990 - December 31, 1990
Reporting date: October 1, 1990

Contents:

Products of this year's effort:

England, A.W., Radiobrightness of diurnally heated, freezing soil, IEEE Trans.Geosci. Remote Sensing, 28, pp.464-476, 1990.

Zuerndorfer, B., and A.W. England, Radiobrightness decision criteria for freeze/thaw boundaries, submitted to IEEE Trans.Geosci. Remote Sensing, 1990.

Zuerndorfer, B., A.W. England, and F.T. Ulaby, An optimized approach to mapping freezing terrain with SMMR data, Proc. of IGARSS'90, College Park, MD, May 21-24, 1990.

England, A.W., The radiobrightness measurement of apparent thermal inertia, URSI Com. F Conference on Remote Sensing Signatures, Hyannis, MA, May 15-17, 1990.

England, A.W., B. Zuerndorfer, and J.F. Galantowicz, Proposed Michigan Earth Grid (MEG) format for world SSM/I data, Technical Memorandum, June, 1990.

1. Summary

Calendar year 1990 was the first year of a 3 year project to develop an operational algorithm for classifying frozen or thawed soils in the northern Great Plains with SSM/I data, and to examine the sensitivity of mesoscale climate models to frozen or thawed soil as a boundary condition. We had shown in an antecedent feasibility project that a combination of the 37 GHz radiobrightness and the 10.7 - 37 GHz spectral gradient of radiobrightness from SMMR would often permit discrimination among frozen and thawed soils. Limitations of the feasibility project were that corroborating ground data were extremely limited, and that the operational flight system is to be the SSM/I with its own spectral channels and overflight times rather than the SMMR. Specific objectives for the current project are:

1. To develop a theoretical model for the radiobrightness of diurnally heated, freezing and thawing soils.

2. To refine the decision criteria for freeze/thaw classification.

3. To use scale-space theory to recover high spatial resolution in the Freeze Map product.

4. To produce a temporal set of Freeze Maps for the northern Great Plains during the fall and winter of 1984.

5. To design and build radiometers for the 19.35, 37.0, and 85.5 GHz SSM/I channels as an SSM/I simulator.

6. To instrument a test site on the northern prairie with the SSM/I simulator and with various temperature and meteorological sensors. We will monitor freezing and thawing of the soil throughout a fall and winter to insure that we understand the process and its signature.

7. To develop an operational algorithm for producing freeze maps of the northern Great Plains from SSM/I data.

8. To investigate the sensitivity of mesoscale climate models to frozen or thawed soil as boundary conditions.

During this first year of the current project, we have completed objectives 1 through 4, and have reported our results in several publications. Objective 5 is partially complete: The radiometer design is complete, parts have been ordered, and the remote instrumentation controller for the radiometers and the ground sensors is under development. The system design will permit us to control and record data in our laboratory through a telephone line from a field site in North Dakota.

An essential activity, but one that was not part of our original proposal, we have supported the SSM/I user community through the SSM/I Products Working Team (SPWT) by supplying the National Snow and Ice Data Center (NSIDC) with candidate Earth grids for organizing world SSM/I data. We are also in the process of verifying resampling algorithms by converting satellite data to what we call the Michigan Earth Grid - 1 (MEG-1) format, and then resampling to recover, for example, a Mercator projection of a selected region without losing appreciable resolution.

2. Project Overview

Using data from the Nimbus-7 Scanning Multichannel Microwave Radiometer (SMMR) for a test area that included North Dakota and parts of the surrounding states and southern Canada, Zuerndorfer et. al. [1] showed that a combination of low 37 GHz radiobrightness, Tb(37), and a low spectral gradient of radiobrightness, $\partial Tb/\partial f$, where f is frequency, becomes an effective freeze indicator, or discriminant, for classifying frozen terrain. Frozen surfaces appear cold at 37 GHz, and exhibit a negative spectral gradient that is largely caused by volume scatter darkening at the shorter wavelengths. The spectral gradient is a linear, least-square fit to the 10.7, 18, and 37 GHz SMMR radiobrightnesses. A surface is classified as frozen only if both Tb(37) and $\partial Tb/\partial f$ are sufficiently low. A freeze map is generated by displaying the FI for each pixel location.

A fundamental problem with the FI algorithm was that radiobrightness measurements from different frequency channels with different spatial resolutions were required to estimate a spectral gradient. To make each radiobrightness value refer to a common area on the ground, data from each channel were compensated to a common spatial resolution. Without a priori surface information, the resolution of data at all frequencies were compensated to the (coarse) resolution of the lowest frequency data used in the spectral gradient estimate. Subsequently, all identified freeze/thaw boundaries were localized to the accuracy of the coarse-resolution data. However, by modelling the radiometer beampatterns as Gaussian, we used results from scale-space theory [2] to associate coarse-resolution freeze/thaw boundaries to fine-resolution 37 GHz boundaries (i.e., 37 GHz radiobrightness threshold crossings) [3]. Thus, freeze/thaw boundaries could be estimated at fine-resolution, but the boundary association process required human intervention.

A second fundamental problem occurred because diurnal insolation produces temperature gradients within the surface that altered SMMR noon and midnight spectral gradients [4]. In addition, time lags between air and surface temperatures produced offsets in measurements made at noon and midnight. Decision criteria for classifying surfaces, and identifying freeze/thaw boundaries, had to be developed to accommodate these day/night differences.

Over this past year, we have developed criteria for classifying frozen and thawed surfaces, and for locating freeze/thaw boundaries, through clustering and a standard unsupervised classification algorithm. The procedure differs from our previous work in that clustering and classification are unsupervised (i.e., autonomous), and the noon and midnight SMMR measurements are clustered separately. We also developed a simple, automated technique for extrapolating freeze/thaw boundary estimates from the coarse spatial resolution of the freeze map to the fine spatial resolution of the 37 GHz channel. The results of this work were presented in [13] and [14], and are summarized below.

2.1 *Radiobrightness of freezing soils*

Freezing and thawing soils exhibit unique radiometric characteristics. To examine these characteristics, diurnal insolation was modeled as 1-dimensional heating of a moist soil halfspace during a typical fall at a northern Great Plains site (Bismarck, ND). The 1-dimensional, heat flow equation is non-linear because both the enthalpy (the change in internal energy with temperature at constant pressure) and the thermal conductivity of freezing soils are non-linear functions of temperature. The problem is particularly difficult because phase boundaries propagate in time, and because soils, particularly clay-rich soils, freeze over a range of temperatures rather than at 0^{o} C--that is, they possess diffuse phase boundaries.

A modified Chernous'ko method was used to integrate the heat flow equation to obtain monthly thermal models during a typical September through December period. Diurnal radiobrightness curves at 10.7, 18, and 37 GHz were computed for each month. The 37 GHz radiobrightness best tracks soil surface temperature, the 10.7-37 GHz spectral gradient of thawed soils is strongly positive, the spectral gradient of frozen soils is slightly negative, and the midnight to noon spectral gradient is shifted by approximately +0.1 K/GHz by diurnal changes in the surface temperature and the thermal gradient. These observations support the use of SMMR's 37 GHz radiobrightness and its 10.7-37 GHz spectral gradient as discriminants in a frozen soil classifier for high latitude prairie. The work was reported in reference [4].

2.2 *Data Clustering*

The decision criteria for detecting freeze/thaw boundaries were based on clustering and unsupervised classification. Unsupervised classification, rather than supervised classification, was used because of the dearth of accurate ground measurements in our test area. All data from SMMR satellite passes that covered more than 67% of the test area were used for clustering, and were incorporated in the scatter diagrams of Figures 1-2. Sixteen noon SMMR passes and thirteen midnight passes met this criterion during our August to December test period. The 18 and 37 GHz averages of vertical and horizontal polarized radiobrightness data were resolution compensated to the (coarse) resolution of the 10.7 GHz channel. Data were re-sampled on a 97.5 km grid (i.e., at the resolution of the 10.7 GHz channel). Scatter diagrams for the noon and midnight data are shown by month in Figures 1a and 1b, respectively.

Migrating means clustering determined cluster centroids for the data of Figures 1a and 1b [5,6]. On the basis of data from our preliminary studies, surfaces were classified into three distinct types -- frozen, hot (and dry), and wet (and cool) -- and a fourth type that we call mixed. A frozen surface is characterized by relatively low spectral gradient and a low 37 GHz radiobrightness. Due to the influence of liquid water in the surface, a wet surface is characterized by a high spectral gradient [4] and low 37 GHz radiobrightness [7]. A hot surface has relatively less surface moisture, producing a "dry" surface dielectric constant similar to a frozen surface. Moreover, the relaxation frequency of free-water increases with temperature, further reducing the spectral gradients of hot surfaces. As a result, a hot surface has a relatively low spectral gradient and a high 37 GHz radiobrightness. A mixed surface has a combination of frozen, wet, and hot characteristics.

Prior to freezing, a surface region is a combination of wet (and cool) and hot (and dry). As freezing begins, the region includes locally frozen surfaces, and would be classified as mixed. Our freeze/thaw criteria lies within the mixed surface cluster in decision space, and represents maximum Tb(37) and $\partial Tb/\partial f$ values along the freeze/thaw boundary. That is, any surface point on the freeze/thaw boundary has at least one component, Tb(37) or $\partial Tb/\partial f$, equal to that of the freeze/thaw criteria. Equivalently, the FI algorithm [1] requires any surface point classified as frozen to have a 37 GHz radiobrightness and a spectral gradient that are less than those of the freeze/thaw criteria.

Cluster centroids determined for the data of Figures 1a and 1b are given in Table 1. Due to SMMR recording problems, limited midnight data were available during December of our test period. Within this limitation, the frozen surface cluster centroid has a lower spectral gradient and 37 GHz radiobrightness at noon than at midnight. Furthermore, because there were few wet surfaces at midnight during the test period, the wet and mixed surface types were inseparable for the midnight data.

Table 1. Cluster centroid in decision space

	NOON DATA		MIDNIGHT DATA	
Surface Type	37 GHz (K)	Gradient (K/GHz)	37 GHz (K)	Gradient (K/GHz)
Frozen	227	-.43	234	-.35
Hot	277	0.11	258	-.01
Wet	238	0.37		
Mixed	250	0.14	243	0.015

Bivariate normal distributions were fit to the cluster data. All data within three standard deviations of a cluster centroid were classified using a Mahanalobis minimum distance classifier (maximum likelihood classification). No preferential weightings of surface types were used. Constant-deviation, single-class ellipses were drawn in decision space for frozen, hot, and wet surfaces (at noon) and for frozen and hot surfaces (at midnight) using the classified data. The freeze/thaw criteria was determined by allowing the deviation of all ellipses to expand equally until all ellipses intersected. The resulting classification ellipses for noon and midnight SMMR data are shown in Figures 2a and 2b, respectively. The corresponding freeze/thaw criteria in decision space are shown in Table 2.

Table 2. Freeze/thaw criteria in decision space; σ are standard deviations of the data within the ellipses.

	37 GHz(K)	Refined 37 GHz(K)	Gradient(K/GHz)	Deviation σ at Intersection
Noon	252	249	0.0625	3.1
Midnight	247	244	-0.044	2.55

By viewing the freeze/thaw criteria derived from clustering as initial estimates for determining the freeze/thaw boundary, we refined the boundary criteria by requiring a minimum scatter of Tb(37) along that boundary. This constraint insures that boundaries in Tb(37) images correspond closely to FI boundaries. The process involves adjusting the Tb(37) component of the freeze/thaw criteria, T37, to minimize the sum square error, SSE, in,

$$SSE = \sum_{i=1}^{N} [Tb_i(37) - T37]$$

Equivalently, the refined T37 is the average 37 GHz radiobrightness on the boundary. The process is first-order since we do not reiterate SSE minimization with the refined criteria. The refined T37 for midnight data from October 24 and for noon data from December 11, are shown in Table 2.

2.3 *Boundary Localization and Automation*

Spectral gradients are regression slopes to SMMR 37 GHz, 18 GHz, and 10.7 GHz radiobrightness measurements. The nominal resolutions of these channels are 30 km, 60 km, and 97.5 km, respectively. Without compensating for the resolution differences between the channels, the spectral gradient estimates can be in error. For example, a non-zero gradient estimate can result from radiobrightnesses that are spatially variant but are locally constant over frequency. To avoid such errors, the image data were compensated to one common resolution -- the (coarse) resolution of the lowest frequency channel used in gradient estimation -- prior to clustering.

Freeze/thaw boundaries combine 37 GHz threshold crossings and spectral gradient threshold crossings. Corresponding 37 GHz threshold crossings occur in fine-resolution 37 GHz images, but not all 37 GHz threshold crossings represent freeze/thaw boundaries. Some are boundaries between moist and dry terrain. Boundary localization is a three-step process that identifies pixels in fine-resolution, 37 GHz images that correspond to freeze/thaw boundaries at coarse-resolution.

Step 1: Uncompensated 10.7 GHz, 18 GHz, and 37 GHz SMMR data are compensated to the resolution of the 10.7 GHz channel. Gaussian spatial filtering is appropriate for resolution compensation if the Fourier transform of the SMMR beampattern is (approximately) Gaussian [8]. Antenna data for the Nimbus-7 SMMR antenna are limited. However, we assume that the Seasat SMMR beampattern [9] approximates the Nimbus-7 SMMR beampattern, and justify Gaussian filtering by showing that the Fourier transform of the Seasat SMMR beampattern is approximately Gaussian (Figure 3). The Gaussian filters used to synthesize compensated data at resolution s2 from uncompensated data at resolution s1 are,

$$H(f,S) = e^{-(2fS)^2/2}$$

where the filter width, S, is,

$$S \equiv (s_2^2 - s_1^2)^{\frac{1}{2}}, \; s_2 > s_1$$

and f is spatial frequency. Values of S for different configurations of resolution compensation are shown in Table 3.

Table 3. Filter bandwidths for resolution compensation.

Nominal Resolution, s1	Synthesized Resolution, s2	Filter Bandwidth, S
30 km (Fine)	60 km (Medium)	51.96 km
30 km (Fine)	97.5 km (Coarse)	93.77 km
60 km (Medium)	97.5 km (Coarse)	78.885 km

Step 2: Using resolution compensated data, Tb(37) and $\partial Tb/\partial f$ are calculated for each image pixel at coarse-resolution. Boundaries in coarse-resolution, 37 GHz images are identified

where 37 GHz data satisfy the Tb(37) freeze/thaw criteria. Pixels along these 37 GHz image boundaries with $\partial Tb/\partial f$ at or below that of the freeze/thaw criteria are identified as freeze/thaw boundary pixels.

Step 3: Fine-resolution, freeze/thaw boundaries are determined by identifying those pixels in fine-resolution, 37 GHz data that satisfy the TB(37) freeze/thaw criteria and correspond to coarse-resolution freeze/thaw pixels of step 2. This process involves tracking boundary locations in 37 GHz images as the amount of resolution compensation is reduced. The resulting boundary locations in the fine-resolution 37 GHz images are best estimates of freeze/thaw boundaries in the sense that they are directly traceable to the coarse-resolution boundaries generated by clustering and maximum likelihood classification. The key to this process is that Gaussian image degradation of step 1 uniquely permits recovery of some fine-resolution information, a result derived in scale-space theory [2,10,11].

Unrefined freeze/thaw criteria (Table 2) were applied to SMMR data for midnight October 24 (Figure 4). Refined freeze/thaw criteria were also applied to the October data (Figure 5). The dark pixels in the freeze maps* (Figures 4a and 5a) correspond to surfaces with low FI value -- surfaces which are most likely frozen -- and freeze/thaw boundaries appear as a fuzzy white lines around these frozen regions. The dark pixels in the 37 GHz images (panels b, d, and f in Figures 4 and 5) correspond to surfaces of low 37 GHz radiobrightness. The fuzzy white lines around these dark regions are the boundary pixels that satisfy the Tb(37) freeze/thaw criterion. Some or all of these boundaries correspond with the coarse-resolution freeze/thaw boundaries of the freeze maps. Similarly, the dark pixels in the spectral gradient images (Figures 4c and 5c) correspond to surfaces with low spectral gradient, and the fuzzy white lines are boundary pixels that satisfy the $\partial Tb/\partial f$ freeze/thaw criterion. In all images, regions of no data are shown as white.

Comparing the "unrefined" images (Figure 4) with the "refined" images (Figure 5) shows that refined criteria generate coarse-resolution, 37 GHz boundaries that are located more closely to freeze map and spectral gradient boundaries. Moreover, refined fine-resolution, 37 GHz boundaries (Figure 5f) are more consistent with ground data than are unrefined 37 GHz boundaries (Figure 4f). Thus, freeze/thaw boundaries derived from refined criteria should be more accurate that those derived from unrefined criteria.

In the refined images of Figure 5, most sections of the coarse-resolution, 37 GHz boundary in the northwest corner of the test area (Figure 5b) correspond with boundaries of the freeze map (Figure 5a). These sections of 37 GHz boundary would be designated as freeze/thaw boundaries. None of the two other boundaries in Figure 5b correspond to any freeze map boundary, and are probably wet/dry boundaries. The freeze/thaw boundary in the coarse-resolution, 37 GHz radiobrightness image also corresponds to boundaries in medium-resolution and fine-resolution, 37 GHz images. That is, medium-resolution and fine-resolution freeze/thaw boundaries are the convoluted boundaries in the northwest corner of Figures 5d and 5f, respectively. Some boundaries are formed at fine-resolution that do not correspond to any boundary observed at coarse-resolution. These boundaries appear around dark radiobrightness "islands" in Figure 5f, and cannot be identified on the basis of the available information. Such boundaries are not part of the freeze/thaw boundary estimates.

Figure 6 represents automated boundary localization for the October midnight SMMR data. Figure 6a repeats the freeze map of Figure 5a, and Figure 6b shows the associated coarse-resolution, 37 GHz radiobrightness image. As before, 37 GHz boundaries are composed of pixels whose 37 GHz radiobrightness equals the Tb(37) component freeze/thaw criteria. However, the 37 GHz boundaries in Figure 6b consist of (fuzzy) white and black sections. Pixels along white boundaries have spectral gradients that are less than or equal to the $\partial Tb/\partial f$ component of the freeze/thaw criteria. That is, white boundaries are most likely to be freeze/thaw boundaries. Pixels

along black boundaries have larger spectral gradients and are less likely to be freeze/thaw boundaries.

In medium-resolution, 37 GHz radiobrightness images (Figure 6c), white boundaries are 37 GHz boundaries that are migrations of white boundaries at coarse-resolution (Figure 6b). Precise distances for boundary migration are calculated from ideal 37 GHz radiobrightness measurements and actual freeze/thaw boundary locations (i.e., radiobrightnesses and boundary locations hypothetically measured at infinitesimal resolution) [12]. While such ideal data is generally unavailable, the midnight and noon SMMR data permits a theoretical migration limit of $(s_2-s_1)/4$ for tracking a boundary from coarser-to-finer resolution images where s_1 and s_2 are the resolutions of finer and coarser resolution images, respectively (Table 3). As a result, white boundaries at medium-resolution (Figure 6c) must be within 9.325 km of white boundaries at coarse-resolution (Figures 6b and 6d). Repeating this process, white boundaries at fine-resolution (Figure 6d) must be within 7.5 km of white boundaries at medium-resolution (Figure 6c).

Frozen terrain is identified iteratively using fine-resolution data. First, pixels along white, fine-resolution boundaries (Figure 6d) are identified as "frozen" pixels. Second, pixels whose 37 GHz radiobrightnesses are less than or equal to the Tb(37) freeze/thaw criterion, and are contiguous to frozen pixels, are also identified as frozen. Third, the previous step is repeated until no additional pixels are identified as frozen. Fourth, the resulting collections of frozen pixels constitute regions of frozen terrain. Using this procedure, terrain identified as frozen is indicated by whitened regions in the northwest corner of the Figure 6e. Because freeze/thaw boundaries must be closed contours, the final freeze/thaw boundary (i.e., the edge of the identified frozen region) contains boundary sections that did not, previously, show strong freeze/thaw boundary indications. Nonetheless, the final freeze/thaw boundaries of Figure 6e represent the best fine-resolution estimates of the actual freeze/thaw boundaries.

2.4 *Temporal set of Freeze Maps*

Automated resolution recovery has been applied to Figures 7a through Figure 7i . Time summaries of the data are given in Table 4. These images show the growth and contraction of ground-freezing from October 24 to November 5, and again from November 27 to December 9. After December 9, the area remains frozen through the end of December.

Table 4. Time summary for images of Figure 7a through Figure 7i; measurement interval is the time interval between the current and the previous measurement.

Figure	Date	Time-of-Day	Interval (Days)
7a	October 24	Midnight	- -
7b	October 30	Midnight	6
7c	November 1	Noon	2.5
7d	November 5	Midnight	3.5
7e	November 27	Midnight	22
7f	November 29	Noon	2.5
7g	December 3	Midnight	3.5
7h	December 9	Midnight	6
7i	December 11	Noon	2.5

3. Michigan Earth Grid

The Michigan Earth Grid (MEG) is a resampling and storage scheme for DMSP SSM/I satellite data. The project was initiated at the spring meeting of the SSM/I Products Working Team (SPWT) as part of an effort to facilitate the processing, storage and distribution of SSM/I data for users in the geoscience community. The first objective of the MEG project was to design a CD-ROM storage format—the earth grid—to which SSM/I raw data could be resampled for condensed storage and easy retrieval. This aspect of the project was completed in June and the proposal is summarized in the appendices. SPWT has given tentative approval to the scheme listed in the appendices as MEG1.

The second objective of the MEG project will be the design of an algorithm to map the raw SSM/I data from the original beam centered sample points to points on the earth grid MEG1. The objective of this resampling is to improved upon nearest-neighbor resampling by interpolating in two dimensions to a high sample density before assigning radiometric values to MEG1 grid points. We are currently coding the transformation and will confirm its robustness with sample raw SSM/I data. In addition, since the storage scheme results in a geometry which cannot be directly projected as an image, an algorithm to produce Mercator images from the stored data set is also being developed. This work will be completed by the next SPWT meeting in mid-October.

4. Modeling Microwave Emission from Moist Soils

The model of microwave emissions from soil developed by Tony England for freeze-thaw discrimination has been modified in order to examine radiobrightness thermal inertia, or RTI. RTI is in general a measure of the degree to which soil moisture decreases the amplitude of diurnal soil temperature variations. In this study, we have defined the RTI parameter as the twelve hour change in radiobrightness at a particular microwave frequency. The model estimates first the thermal response of the soil to diurnal heating and secondly the soil's microwave emissions. The results of the thermal model are shown in Figures 8 and 9. It is clear that moisture content decreases the range of surface temperatures and temperature gradients.

Direct thermal effects and the effect of dielectric constant change with temperature combine to produce distinct diurnal radiobrightness signatures as a function of soil moisture, as shown in Figures 10 and 11. We see that moisture content has a marked effect on the profiles -- especially at 37 and 85.5 GHz. In addition, since the angle of incidence is high (53°), the effect of emissivity change in high moisture soils produces an inversion of the diurnal wave at the higher frequencies for horizontally polarized radiation. Figures 12 through 17 show the relationships between soil moisture and the twelve hour radiobrightness difference for all combinations of polarization and frequency. It can be seen that the 2:00 am/pm difference shows maximum sensitivity to soil moisture and that the 85.5 GHz H-polarized signal is the most sensitive overall. A paper to report this work is currently being completed for submission to IEEE Geoscience and Remote Sensing.

5. SSM/I Freeze Thaw and Soil Moisture Field Study

A field study slated to begin in the mid to late summer of 1991 will examine the effects of moisture and freezing on microwave emissions from soils. The objective of the study is to verify the theoretical models developed by Tony England and Brian Zuerndorfer as described in previous sections. The following briefly describes the experiment plan and the highlights of current work.

5.1 *Field Study Measurements and Plan*

The experiment location is at an agricultural site associated with the University of North Dakota. Since the objectives require a long period of uninterrupted measurement, the entire apparatus will be self-contained except for power and communications connections. In addition, although data acquisition will be automatic, a remote operation capability over telephone lines is being developed so that control can be arrested from the operating computer in North Dakota for trouble shooting and data dumps.

As currently envisioned, the types of measurements to be made fall into four categories. Firstly, radiometric measurements will be made with three microwave radiometers at 19.35 GHz, 37.0 GHz, and 85.5 GHz and an infrared radiometer. Secondly, subsoil measurements of temperature will be made at various depths with thermistors. In addition, subsoil measurements of soil moisture will be made in real time by low frequency electromagnetic probes (to be developed), and by conventional soil sample methods for periodic confirmation of probe accuracy. Thirdly, meteorologic measurements such as wind speed and direction, humidity, solar incident radiation, precipitation and snow cover are planned. Lastly, various measurements for internal temperature control are planned in order to maintain precise temperature conditions for the radiometers and the control unit.

5.2 *19.35, 37.0 and 85.5 GHz Radiometers*

The designs for the three microwave radiometers have been completed and the front-end components are currently on order from two vendors, Millitech and Electromagnetic Sciences. Block diagrams of the designs are shown in Figures 18, 19 and 20. The basic Dicke type radiometer was chosen for its simplicity and long term stability. Since we will not be able to calibrate frequently, the temperature of the radiometers must be precisely controlled to maintain gain stability. However, since temperature can be controlled with heaters and proper insulation and there is no constraint on measurement integration time, the overall degree of accuracy and precision of the radiometers should be high.

5.3 *Data Acquisition and Communications*

The remote location of the apparatus requires an elaborate control and communications system for the acquisition of data. We have developed a scheme with the help of a University of Michigan senior, Dan Burkel, who is currently designing software for the controlling computer. The system is outlined in Figure 18. The primary component is a Macintosh II computer which will continuously handle control and data acquisition in the field. Periodically, a Macintosh IIfx located in our offices will arrest control of the field unit from its operating system using remote communications software through high-speed modems. In this mode, an operator will be able to trouble shoot problems, monitor the acquisition of data using real-time displays and acquire data from the field unit's hard disk. The field unit will operate two I/O boards capable of measuring up to 64 voltage inputs and generating TTL and waveform output signals.

6. References

[1] Zuerndorfer, B.W., England, A.W., Dobson, C.M., and Ulaby, F.T., 1990, Mapping freeze/thaw boundaries with SMMR data, J. Agriculture and Forest Meteorology, Vol. 52, pp. 199-225.

[2] Witkin, A., 1983, Scale-space filtering, Proc. Int. Joint. Conf. Artif. Intell., Karlsruhe, West Germany, p. 1019-1021.

[3] Zuerndorfer, B.W., England, A.W., and Wakefield, G.H., 1989, The radiobrightness of freezing terrain, 1989 IEEE Int. Geosci. and Remote Sensing Symp., Vancouver, Canada.

[4] England, A.W., 1990, Radiobrightness of diurnally heated, freezing soil, IEEE Trans. Geosc. and Rem. Sens., GE-28, No. 4, pp. 464-476.

[5] Richards. J.A., 1986, Remote Sensing Digital Image Analysis , Springer-Verlag, Berlin.

[6] Clustering and classification was performed on a Sun-4 workstation using EASI software, version 4.1, from PCI, Inc. of Richmond Hill, Ontario (Canada).

[7] Hoekstra, P. and Delaney, A., 1974, Dielectric properties of soils at UHF and microwave frequencies, J. Geophys. Res. 79, pp. 1699-1708.

[8] Bracewell, R. N., 1986, The Fourier Transform and Its Applications, McGaw-Hill.

[9] Njoku, E.G., J.M. Stacey, and F.T. Barath, 1980, The Seasat Scanning Multichannel Microwave Radiometer (SMMR): Instrument description and performance, IEEE Trans. Ocean Engin. OE-5, pp. 100-115.

[10] Yuille, A., and T. Poggio, 1986, Scaling theorems for zero crossings, IEEE Trans. Patt. Anal. Mach. Intell., Vol. PAMI-8, No. 1, p. 15-25.

[11] Zuerndorfer, B. and G. H. Wakefield, 1990, Extensions of scale-space filtering to machine-sensing systems, IEEE Trans. Patt. Anal. Mach. Intell., Vol. 12, No., 9, pp. 868-882.

[12] Zuerndorfer, B. and G. H. Wakefield, 1990, Applications of scale-space filtering to signature analysis, IEEE Trans. Acoust. Speech Signal Process., under review.

[13] Zuerndorfer, B.W., A.W. England, and F.T Ulaby , 1990, An optimized approach to mapping freezing terrain with SMMR data, 1990 IEEE Int. Geosci. and Remote Sensing Symp., Washington, DC.

[14] Zuerndorfer, B.W. and A.W. England, 1990, Radiobrightness decision criteria for freeze/thaw boundaries, IEEE Trans. Geosc. and Rem. Sens., under review.

7. Figure Captions

Figure 1. Scatter diagram of $\partial Tb/\partial f$ versus Tf(37) throughout North Dakota and the surrounding region. Data were collected from 8/1/84 to 12/31/84. (a) is noon data, and (b) is midnight data.

Figure 2. Single class ellipses of $\partial Tb/\partial f$ versus Tb(37) throughout North Dakota and the surrounding region. Data were collected from 8/1/84 to 12/31/84. (a) is noon data, and (b) is midnight data.

Figure 3. Radiation pattern of Seasat SMMR antenna versus Gaussian model.

Figure 4. A comparison of reported air and soil temperatures with images of North Dakota and the surrounding region. Boundaries were determined using unrefined freeze/thaw criteria. Data were collected at midnight, October 24, 1984.

(a) Freeze map at coarse resolution
(b) 37 GHz radiobrightness at coarse resolution
(c) Spectral gradient at coarse resolution
(d) 37 GHz radiobrightness at medium resolution
(e) Air and soil temperatures
(f) 37 GHz radiobrightness at fine resolution

Figure 5. A comparison of reported air and soil temperatures with images of North Dakota and the surrounding region. Boundaries were determined using refined freeze/thaw criteria. Data were collected at midnight, October 24, 1984.

(a) Freeze map at coarse resolution
(b) 37 GHz radiobrightness at coarse resolution
(c) Spectral gradient at coarse resolution
(d) 37 GHz radiobrightness at medium resolution
(e) Air and soil temperatures
(f) 37 GHz radiobrightness at fine resolution

Figure 6. Automated images of North Dakota and the surrounding region. Boundaries were determined using refined freeze/thaw criteria. Data were collected at midnight, October 24, 1984.

(a) Freeze map at coarse resolution
(b) 37 GHz radiobrightness at coarse resolution
(c) 37 GHz radiobrightness at medium resolution
(d) 37 GHz radiobrightness at fine resolution
(e) Classified frozen ground at fine resolution

Figure 7. Automated images of classified frozen ground of North Dakota and the surrounding region. Data were collected at irregular intervals from 10/24/84 through 12/11/84.

(a) Midnight, 10/24/84
(b) Midnight, 10/30/84
(c) Noon, 11/1/84
(d) Midnight, 11/5/84
(e) Midnight, 11/27/84
(f) Noon, 11/29/84
(g) Midnight, 12/3/84
(h) Midnight, 12/9/84
(i) Midnight, 12/11/84

Figure 8. July through August diurnal surface temperature variation for 7.5%, 15% and 25% moist soils (compared by weight to dry weight). Based upon a theoretical model of a diurnally heated, homogeneous halfspace having the constitutive properties of a typical sandy loam.

Figure 9. July through August diurnal surface temperature gradient variation for 7.5%, 15% and 25% moist soils.

Figure 10. July diurnal variation in the 12 hour radiobrightness difference at vertical polarization for 10.7, 19.35, 37.0 and 85.5 GHz radiation and 7.5%, 15% and 25% moist soils.

Figure 11. Like Figure 10 except for horizontally polarized radiation.

Figure 12. Relationship between the 12 hour change in radiobrightness and soil moisture for noon/midnight, 2:00am/pm, 4:30am/pm and 6:00am/pm observation times and 19.35 GHz, vertically polarized radiation.

Figure 13. Like Figure 12 except 19.35 GHz, horizontally polarized radiation.

Figure 14. Like Figure 12 except 37.0 GHz, vertically polarized radiation.

Figure 15. Like Figure 12 except 37.0 GHz, horizontally polarized radiation.

Figure 16. Like Figure 12 except 85.5 GHz, vertically polarized radiation.

Figure 17. Like Figure 12 except 85.5 GHz horizontally polarized radiation.

Figure 18. Block diagram of the 19.35 GHz radiometer design. Fundamental parameters are listed at the upper left and line power and voltage values are listed next to the line where appropriate. The control unit interface is indicated by the gray box.

Figure 19. Like Figure 18 except 37.0 GHz radiometer.

Figure 20. Like Figure 18 except 85.5 GHz radiometer.

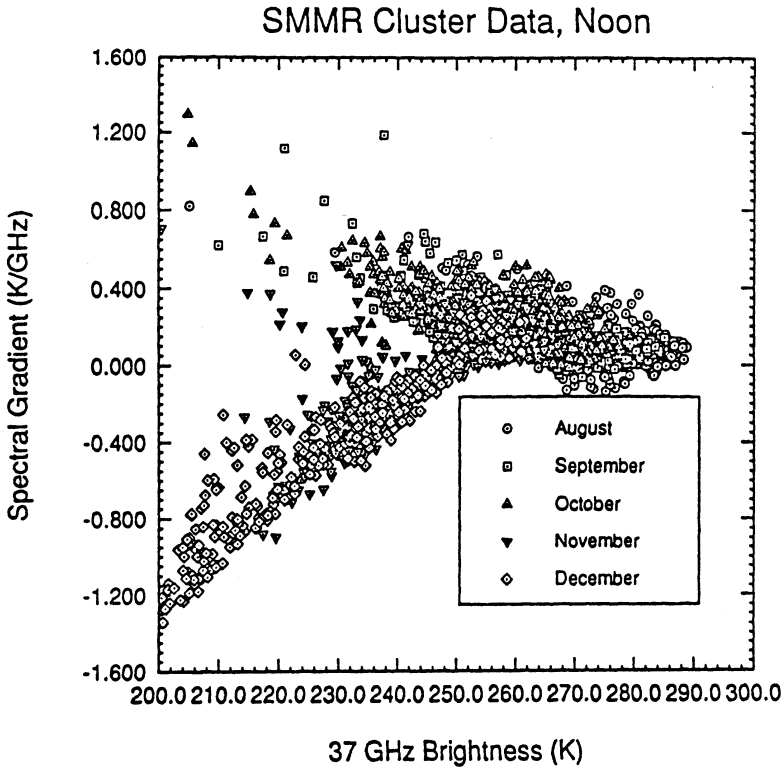
SMMR Cluster Data, Noon
Spectral Gradient (K/GHz)
1.600
1.200
0.800
0.400
0.000
-0.400
-0.800
-1.200
-1.600
200.0 210.0 220.0 230.0 240.0 250.0 260.0 270.0 280.0 290.0 300.0
37 GHz Brightness (K)
August
September
October
November
December

Fig. 1.a

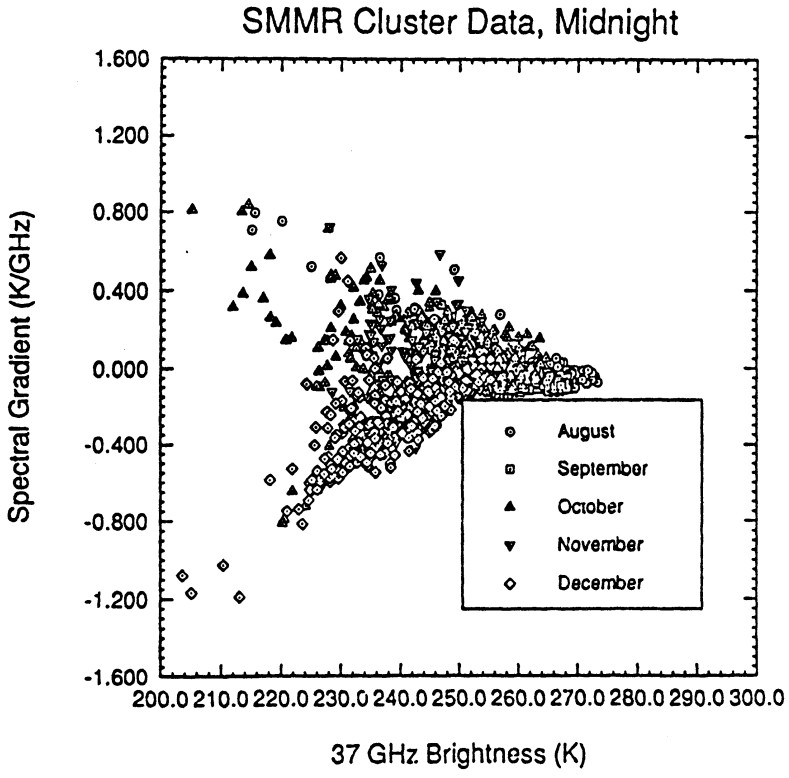
SMMR Cluster Data, Midnight
Spectral Gradient (K/GHz)
1.600
1.200
0.800
0.400
0.000
-0.400
-0.800
-1.200
-1.600
200.0 210.0 220.0 230.0 240.0 250.0 260.0 270.0 280.0 290.0 300.0
37 GHz Brightness (K)
August
September
October
November
December

Fig. 1 b

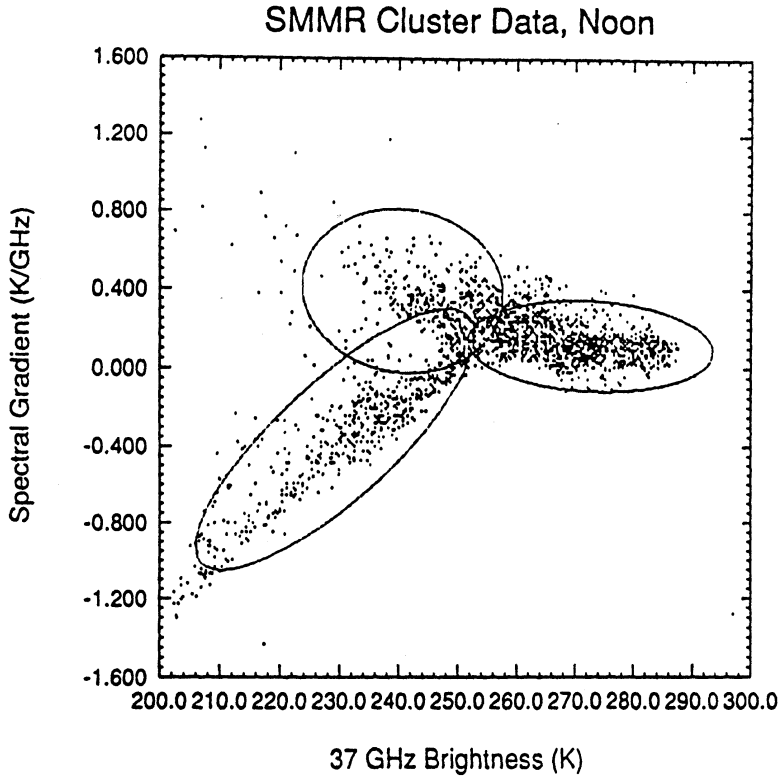
SMMR Cluster Data, Noon
Spectral Gradient (K/GHz)
1.600
1.200
0.800
0.400
0.000
-0.400
-0.800
-1.200
-1.600
200.0 210.0 220.0 230.0 240.0 250.0 260.0 270.0 280.0 290.0 300.0
37 GHz Brightness (K)

Fig. 2a

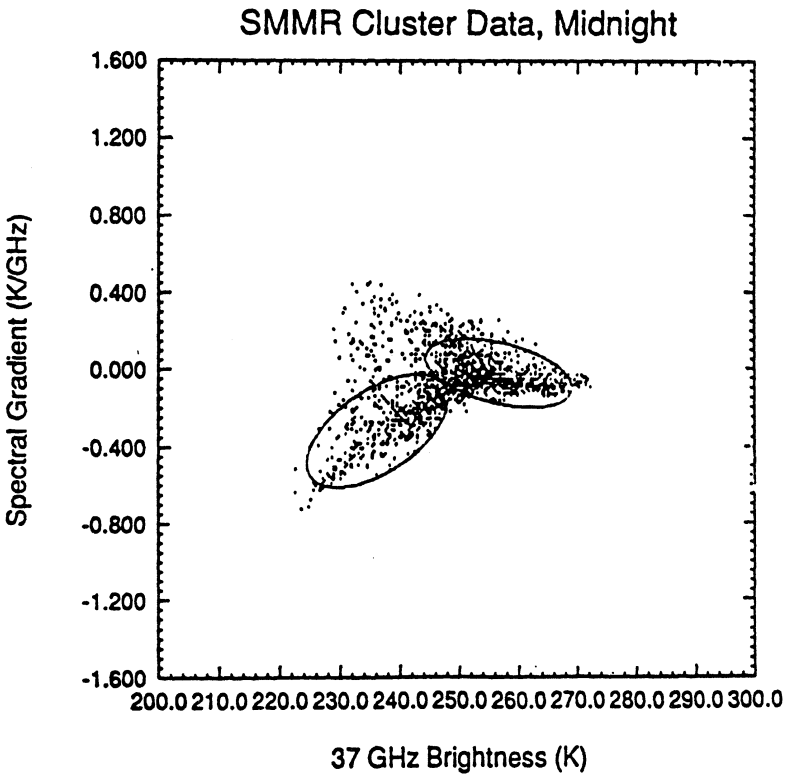
SMMR Cluster Data, Midnight
Spectral Gradient (K/GHz)
1.600
1.200
0.800
0.400
0.000
-0.400
-0.800
-1.200
-1.600
200.0 210.0 220.0 230.0 240.0 250.0 260.0 270.0 280.0 290.0 300.0
37 GHz Brightness (K)

Fig. 2b

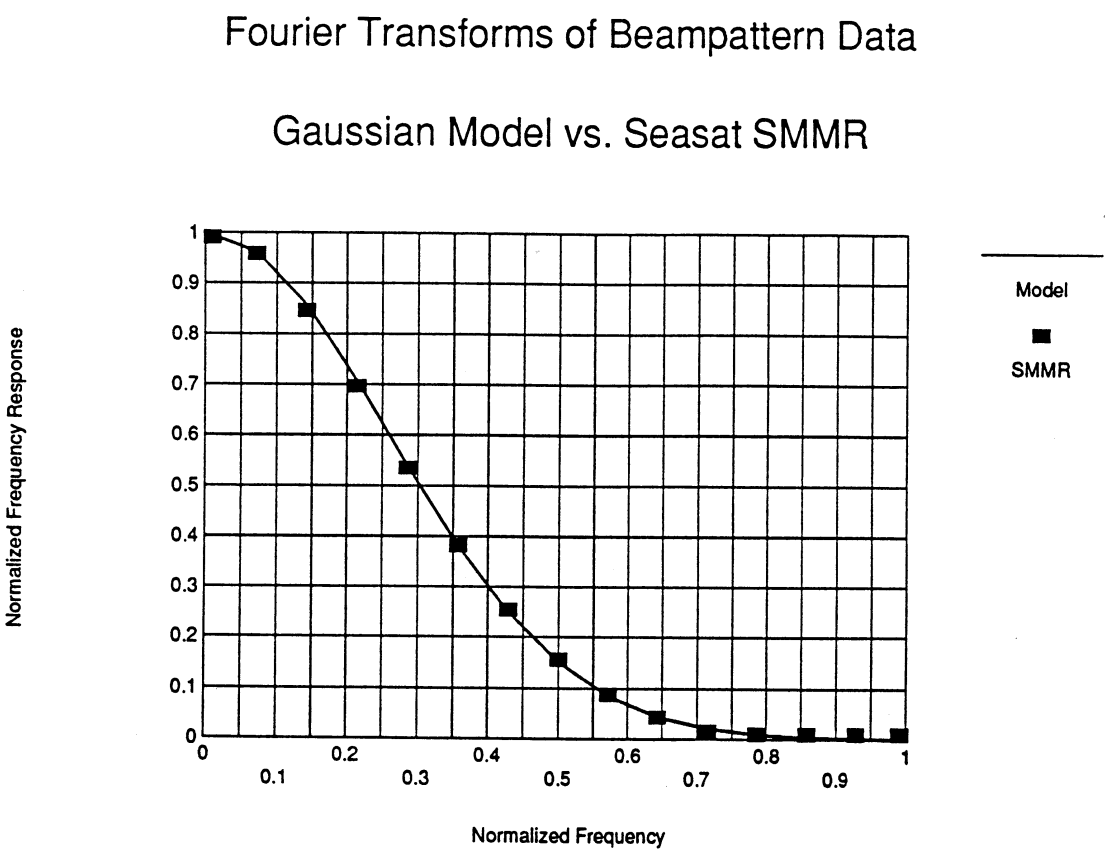
Fourier Transforms of Beampattern Data
Gaussian Model vs. Seasat SMMR
Normalized Frequency Response
1
0.9
0.8
0.7
0.6
0.5
0.4
0.3
0.2
0.1
0
0
0.1
0.2
0.3
0.4
0.5
0.6
0.7
0.8
0.9
1
Normalized Frequency
Model
SMMR

Fig. 3

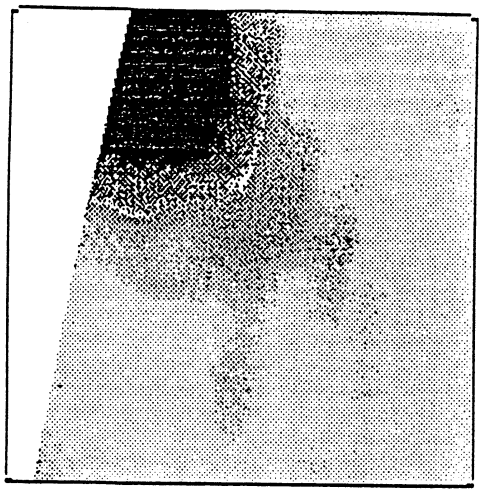

Fig. 4a

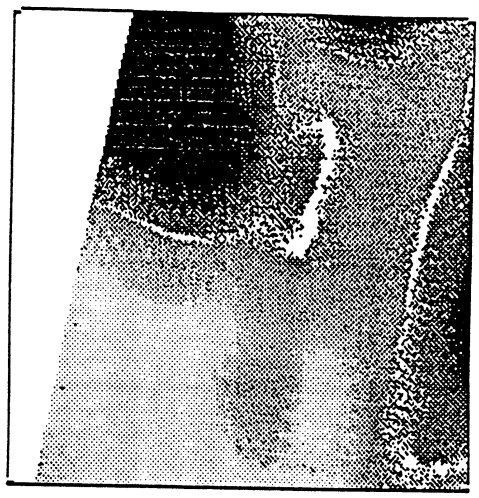

Fig. 4b

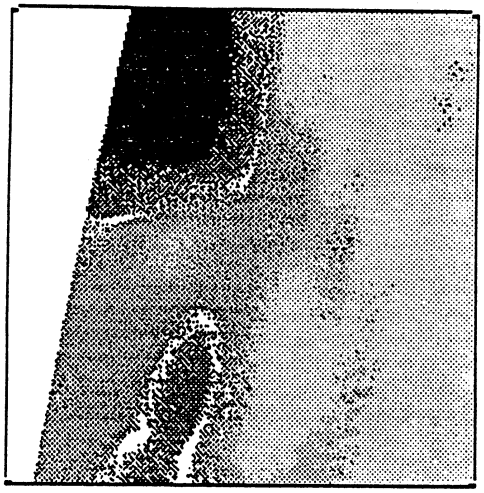

Fig. 4c

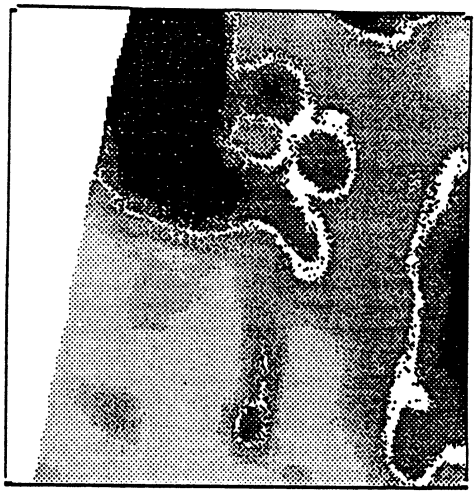

Fig. 4d

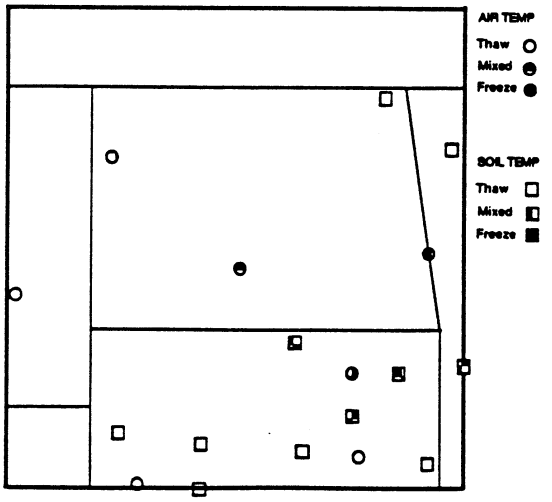

Fig. 4e

Fig. 4f

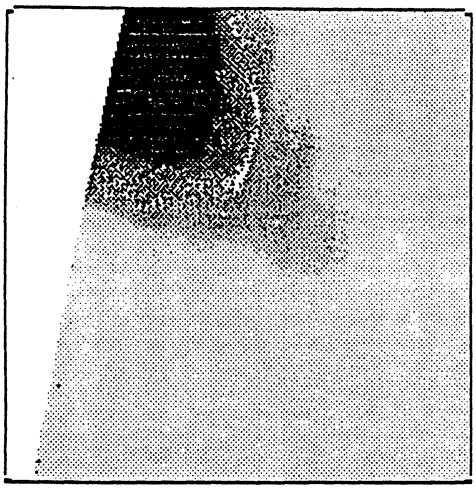

Fig. 5 a

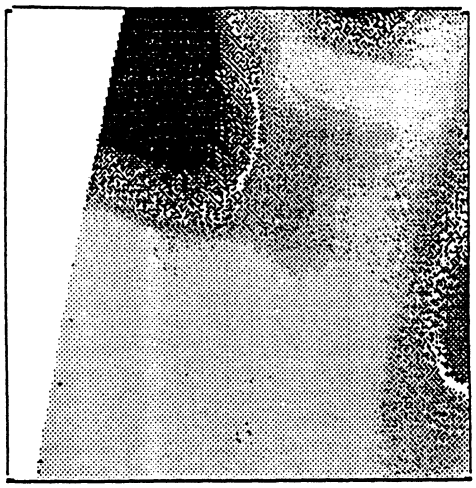

Fig. 5 b

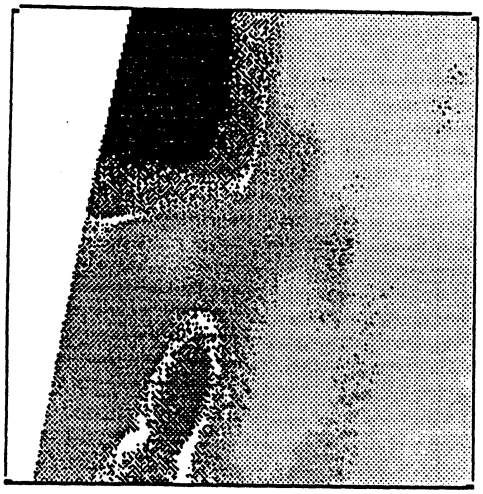

Fig. 5 c

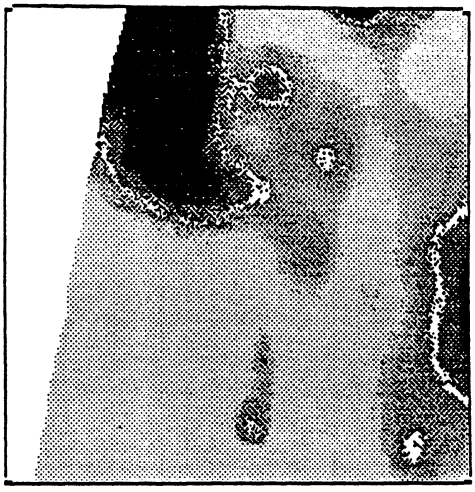

Fig. 5 d

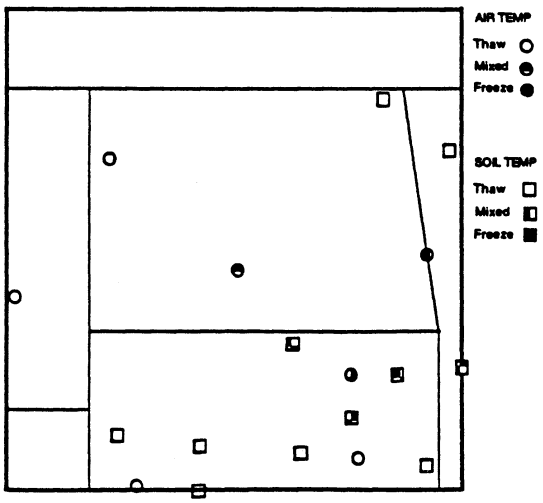

Fig. 5 e

Fig. 5 f

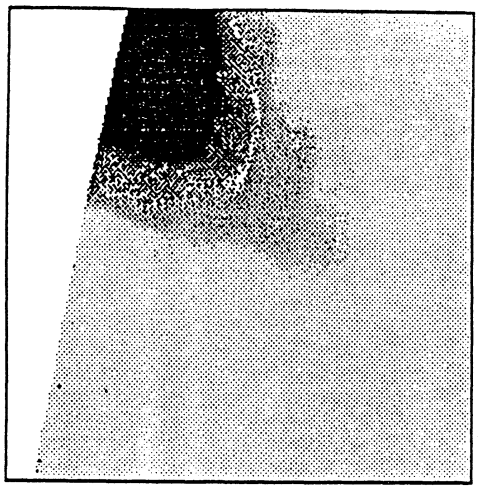

Fig. 6.a

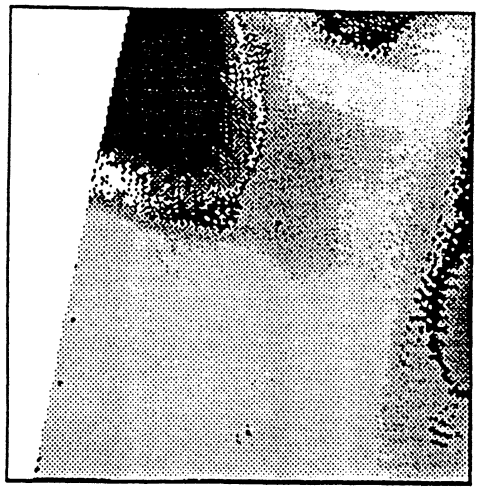

Fig. 6.b

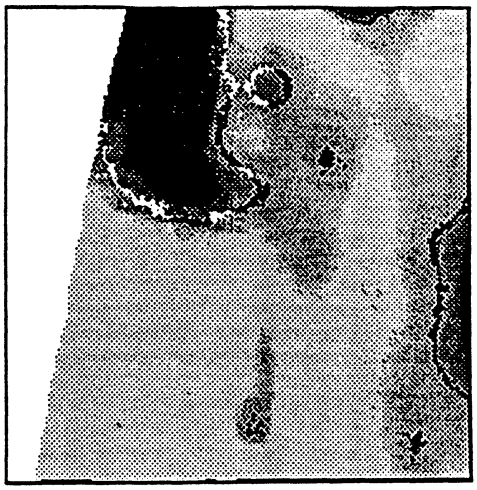

Fig. 6.c

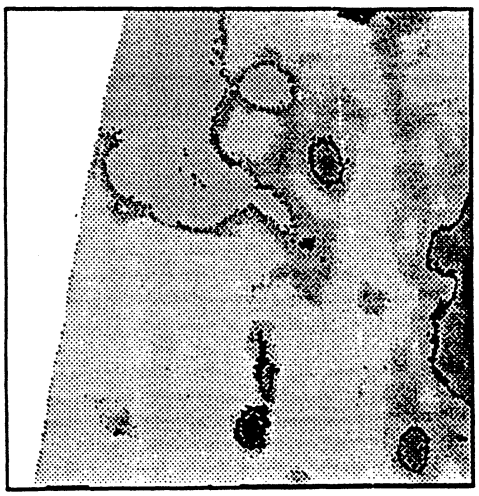

Fig. 6.e

Fig. 6.d

Fig. 7a

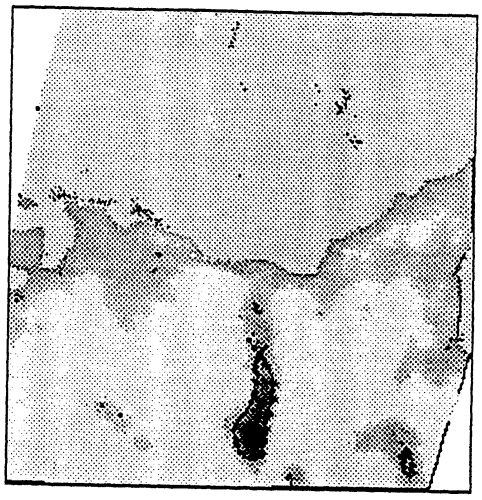

Fig. 7b

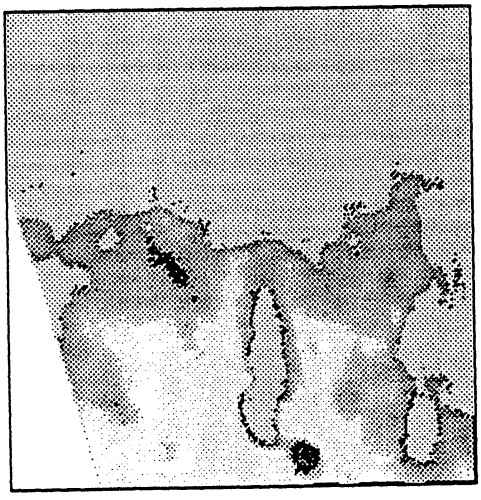

Fig. 7c

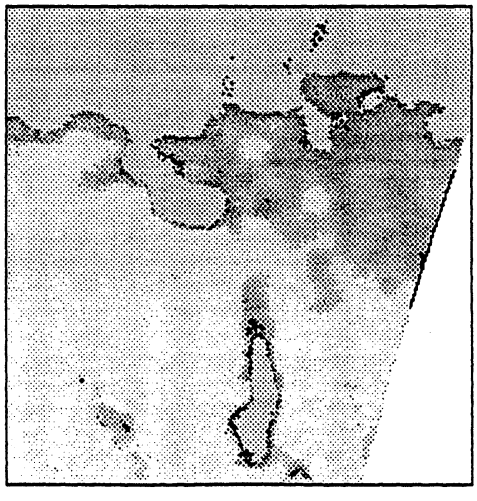

Fig. 7d

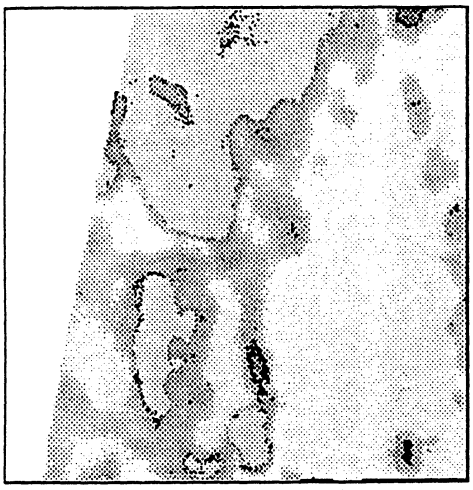

Fig. 7 e

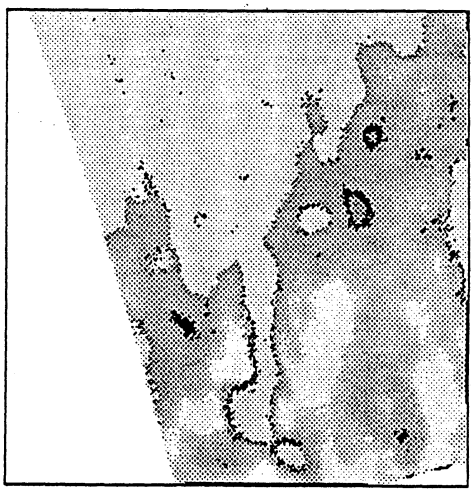

Fig. 7 f

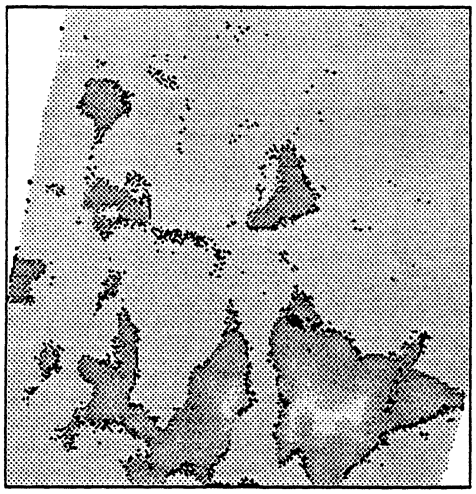

Fig. 7 g

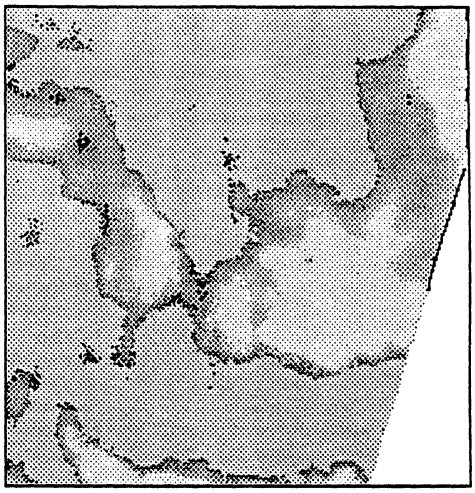

Fig. 7h

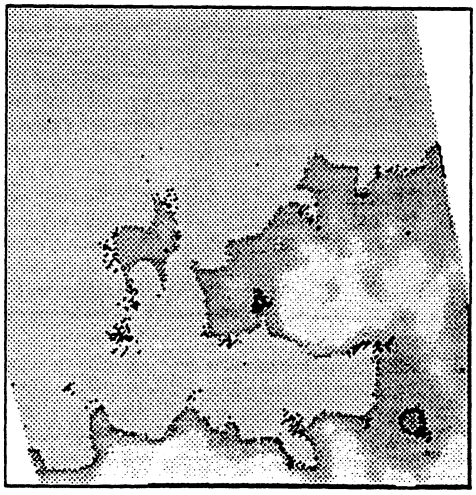

Fig. 7 i

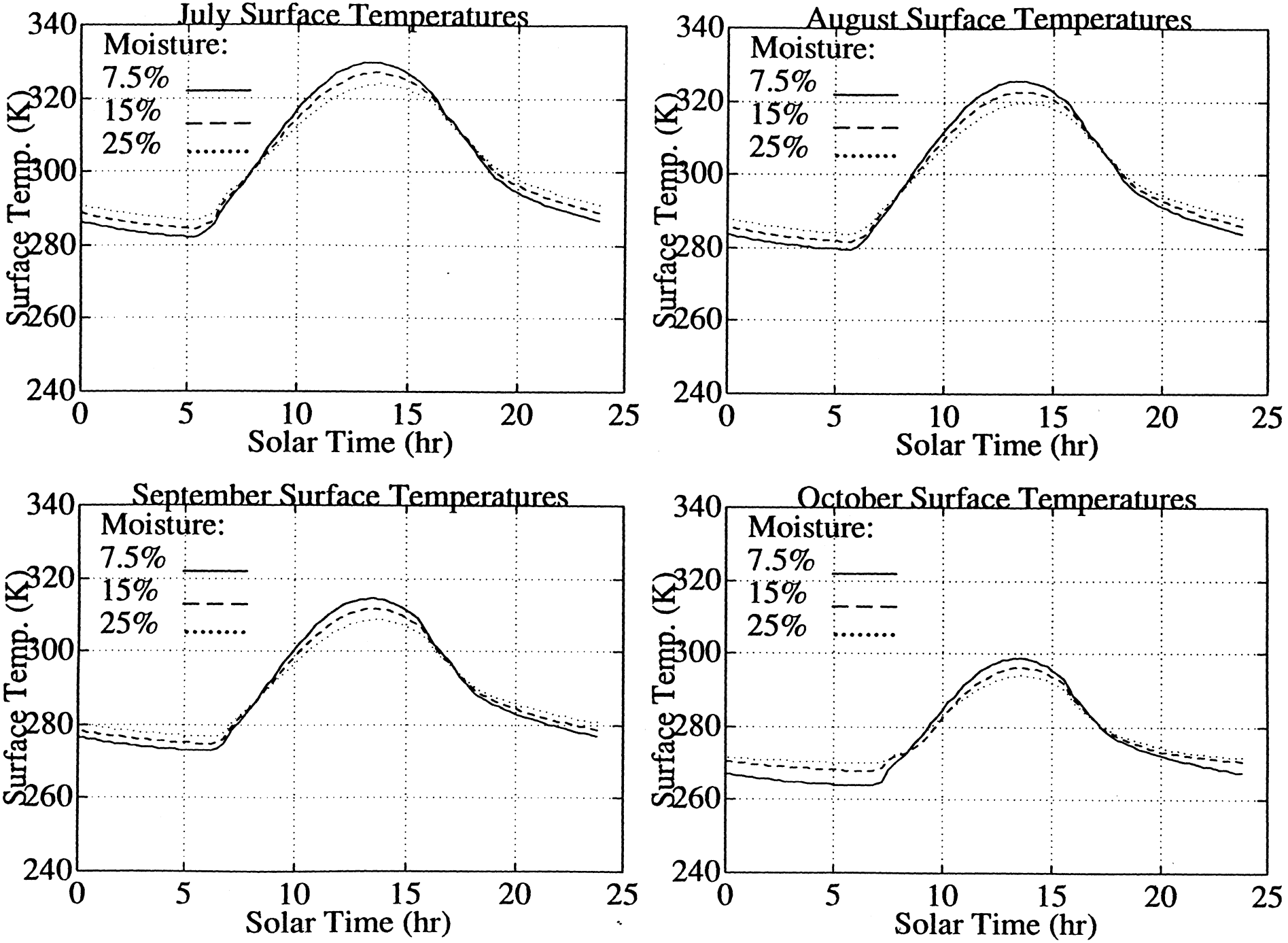
July Surface Temperatures
August Surface Temperatures
September Surface Temperatures
October Surface Temperatures
Moisture:
7.5%
15%
25%
Surface Temp. (K)
Solar Time (hr)
340
320
300
280
260
240
0
5
10
15
20
25

Fig. 8

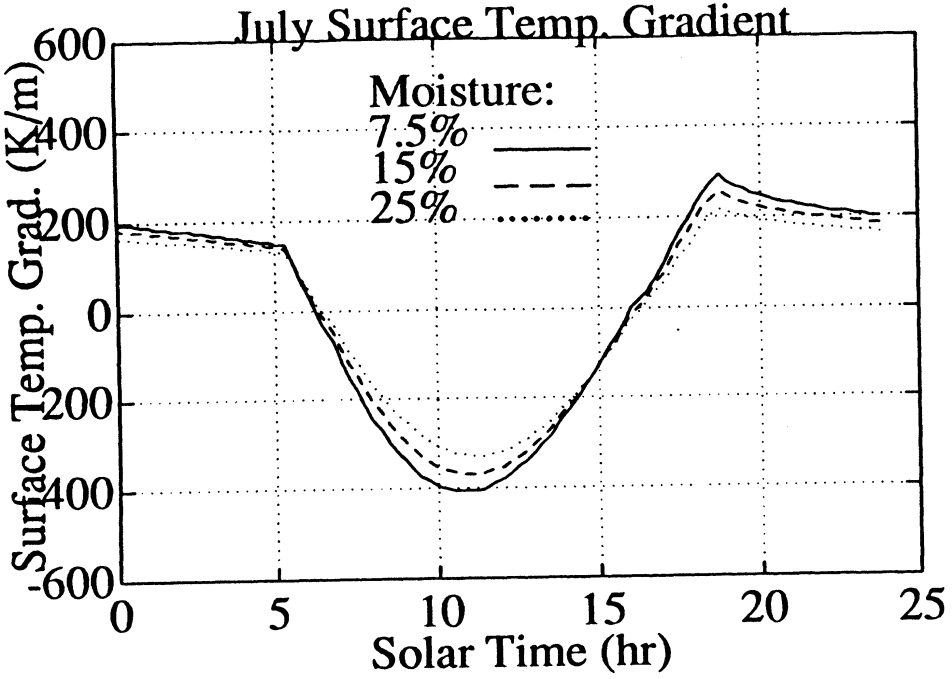
July Surface Temp. Gradient
Moisture:
7.5%
15%
25%
Surface Temp. Grad. (K/m)
600
400
200
0
-200
-400
-600
0
5
10
15
20
25
Solar Time (hr)

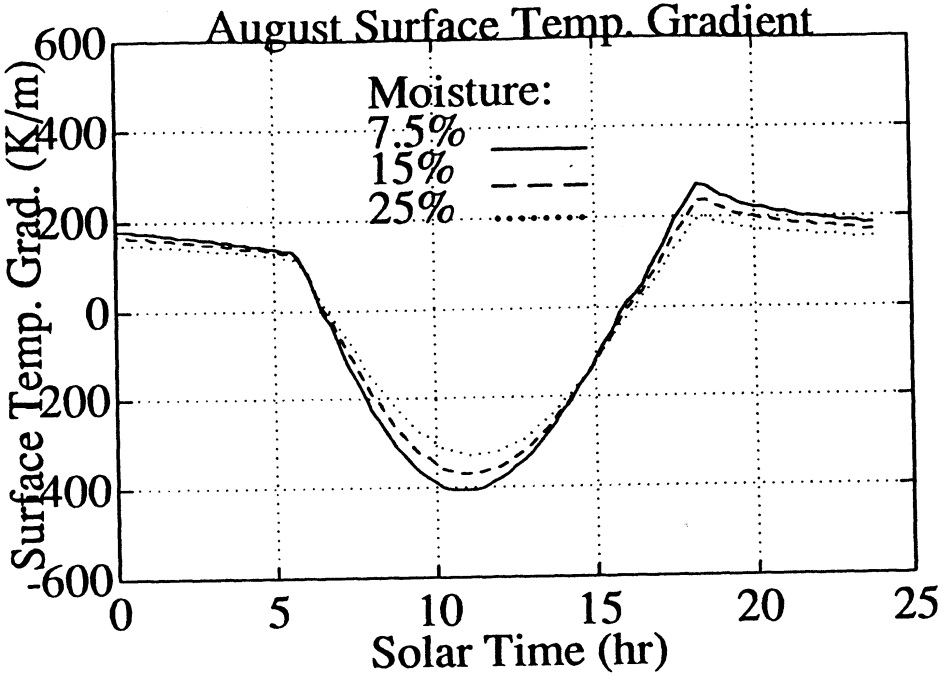
August Surface Temp. Gradient
Moisture:
7.5%
15%
25%
Surface Temp. Grad. (K/m)
600
400
200
0
-200
-400
-600
0
5
10
15
20
25
Solar Time (hr)

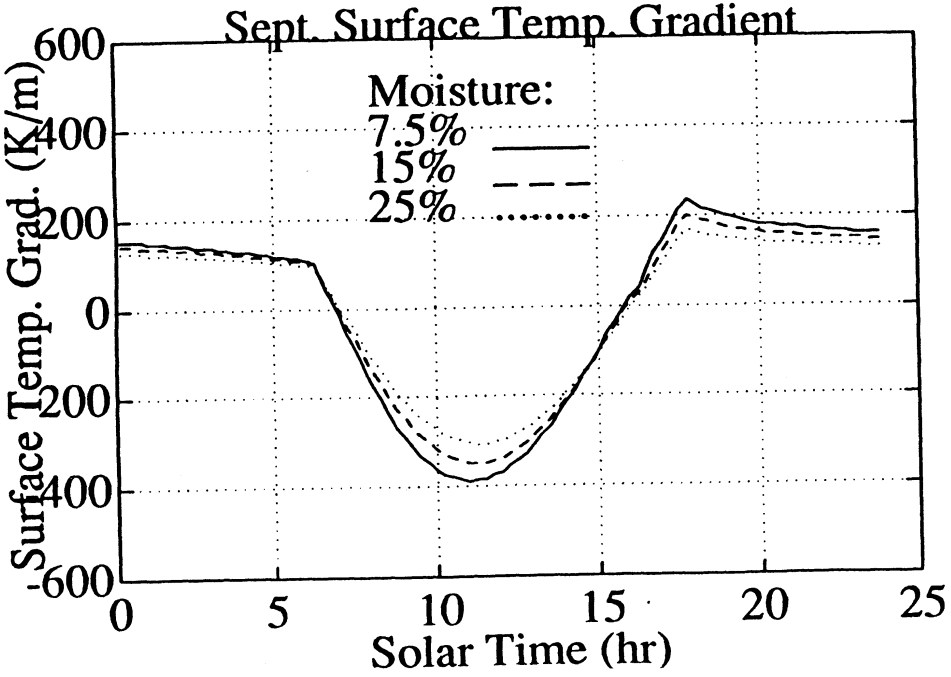
Sept. Surface Temp. Gradient
Moisture:
7.5%
15%
25%
Surface Temp. Grad. (K/m)
600
400
200
0
-200
-400
-600
0
5
10
15
20
25
Solar Time (hr)

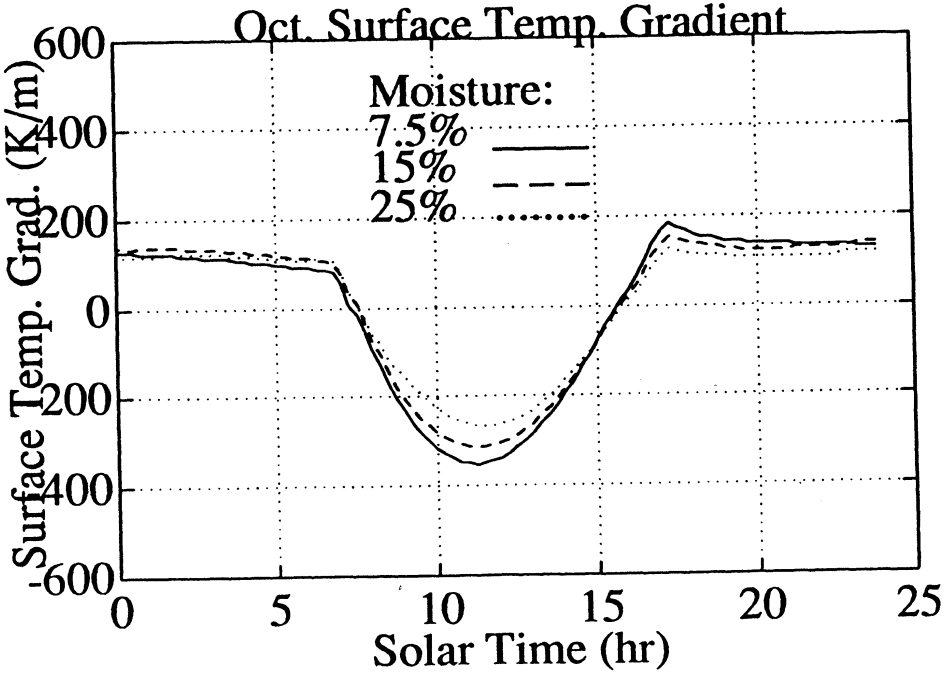
Oct. Surface Temp. Gradient
Moisture:
7.5%
15%
25%
Surface Temp. Grad. (K/m)
600
400
200
0
-200
-400
-600
0
5
10
15
20
25
Solar Time (hr)

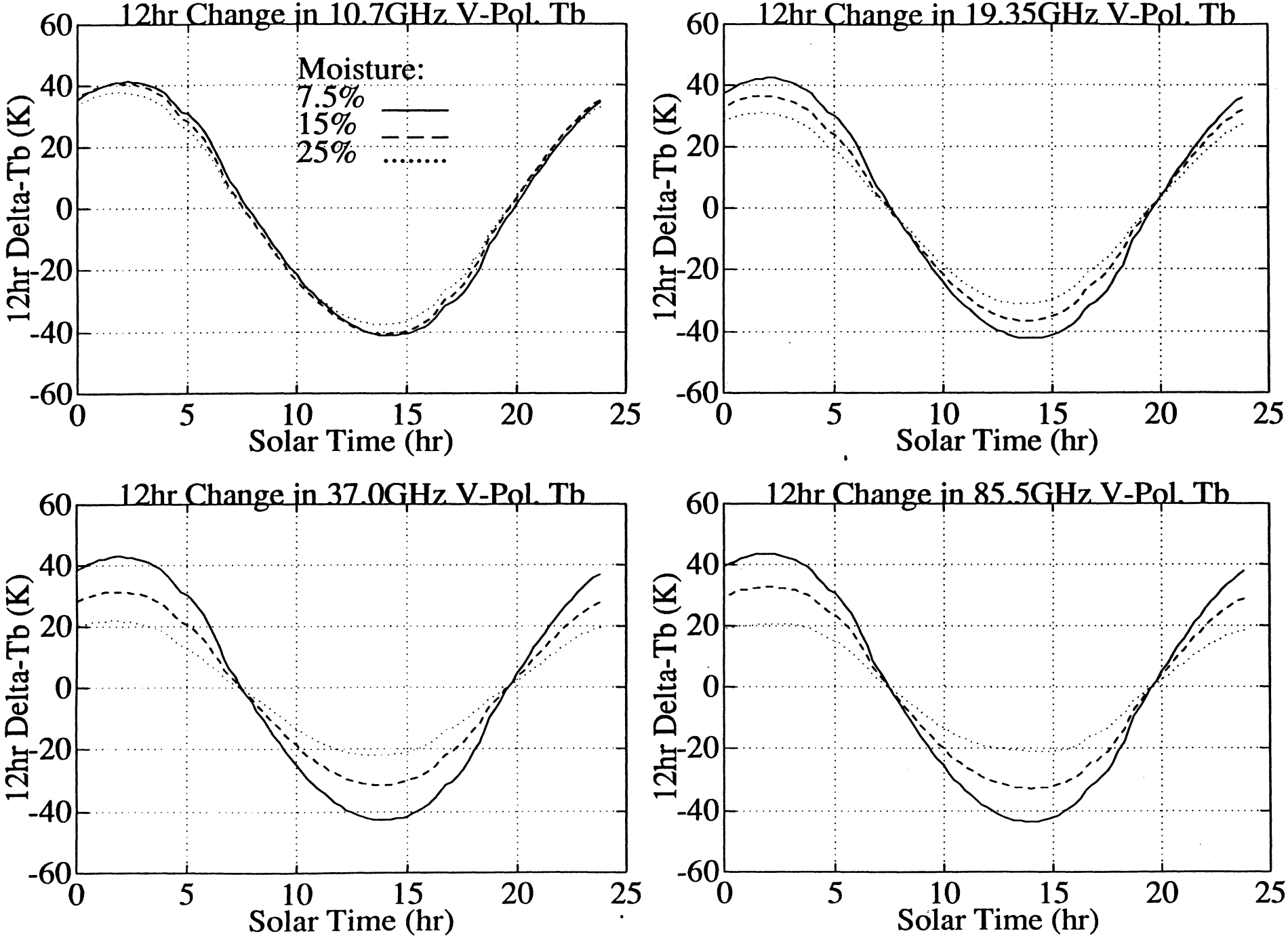
12hr Change in 10.7GHz V-Pol. Tb
Moisture:
7.5%
15%
25%
12hr Delta-Tb (K)
Solar Time (hr)
12hr Change in 19.35GHz V-Pol. Tb
12hr Delta-Tb (K)
Solar Time (hr)
12hr Change in 37.0GHz V-Pol. Tb
12hr Delta-Tb (K)
Solar Time (hr)
12hr Change in 85.5GHz V-Pol. Tb
12hr Delta-Tb (K)
Solar Time (hr)

Fig. 10

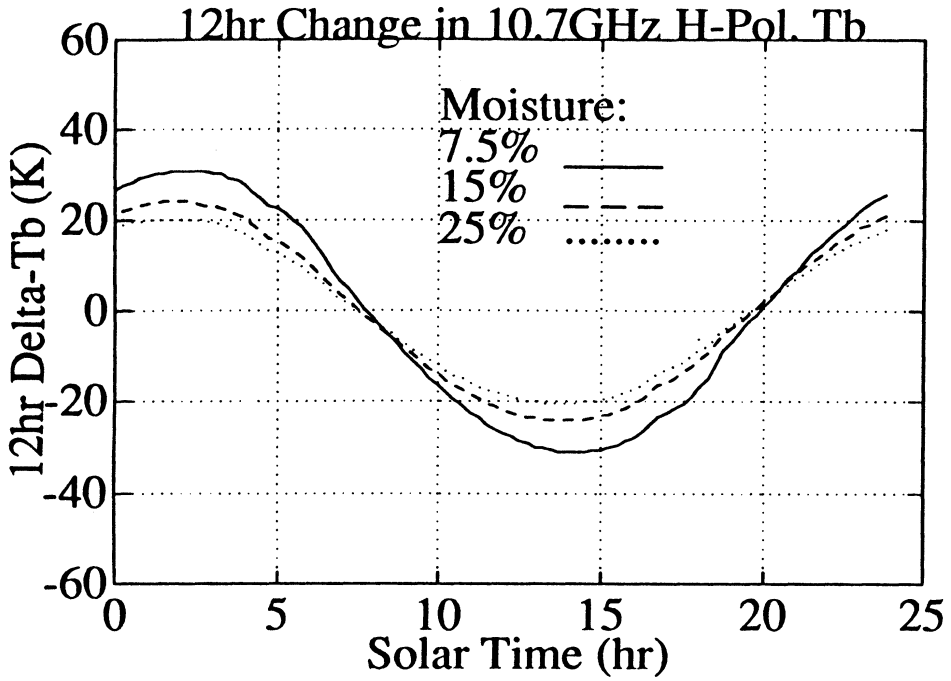
12hr Change in 10.7GHz H-Pol. Tb
Moisture:
7.5%
15%
25%
12hr Delta-Tb (K)
Solar Time (hr)
60
40
20
0
-20
-40
-60
0
5
10
15
20
25

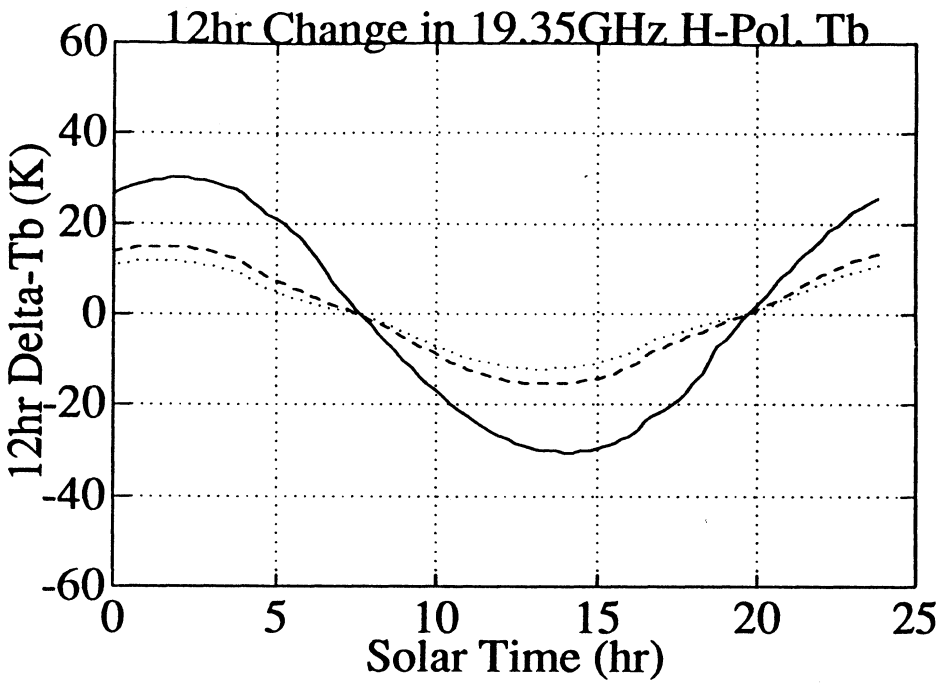
12hr Change in 19.35GHz H-Pol. Tb
12hr Delta-Tb (K)
Solar Time (hr)
60
40
20
0
-20
-40
-60
0
5
10
15
20
25

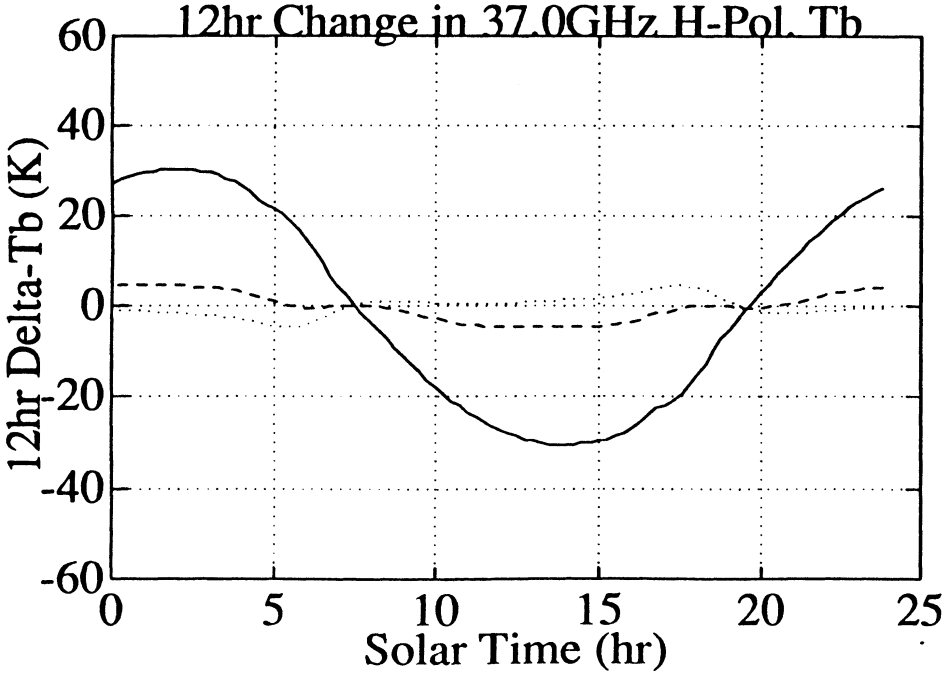
12hr Change in 37.0GHz H-Pol. Tb
12hr Delta-Tb (K)
Solar Time (hr)
60
40
20
0
-20
-40
-60
0
5
10
15
20
25

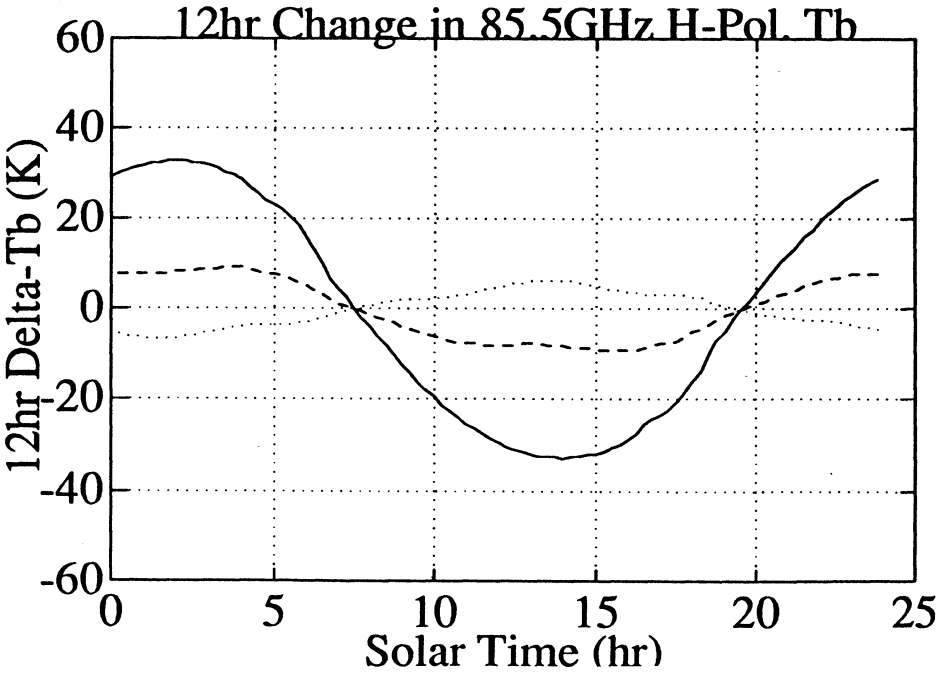
12hr Change in 85.5GHz H-Pol. Tb
12hr Delta-Tb (K)
Solar Time (hr)
60
40
20
0
-20
-40
-60
0
5
10
15
20
25

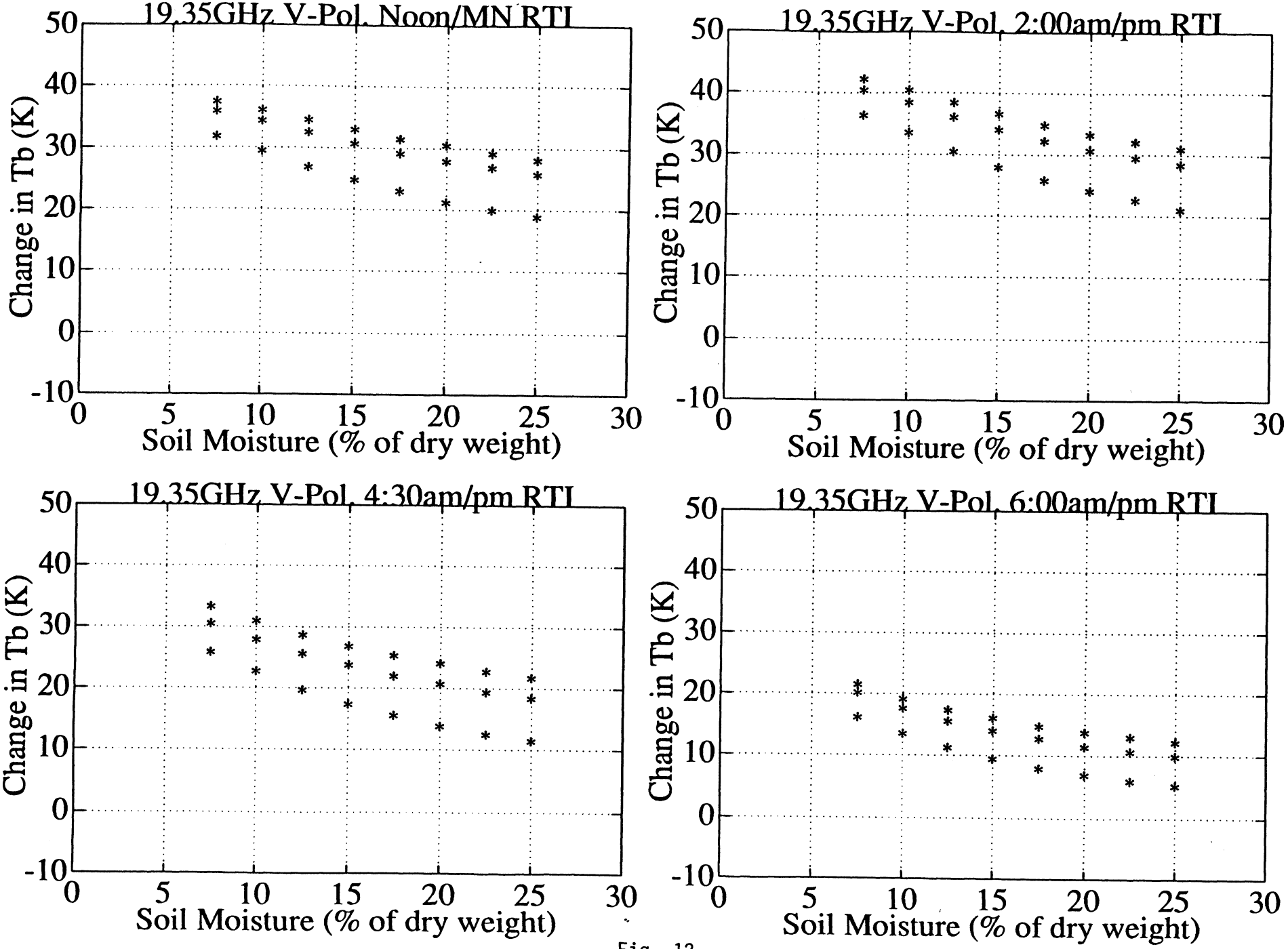
19.35GHz V-Pol, Noon/MN RTI
19.35GHz V-Pol, 2:00am/pm RTI
19.35GHz V-Pol, 4:30am/pm RTI
19.35GHz V-Pol, 6:00am/pm RTI
Change in Tb (K)
Soil Moisture (% of dry weight)
50
40
30
20
10
0
-10
0
5
10
15
20
25
30

Fig. 12

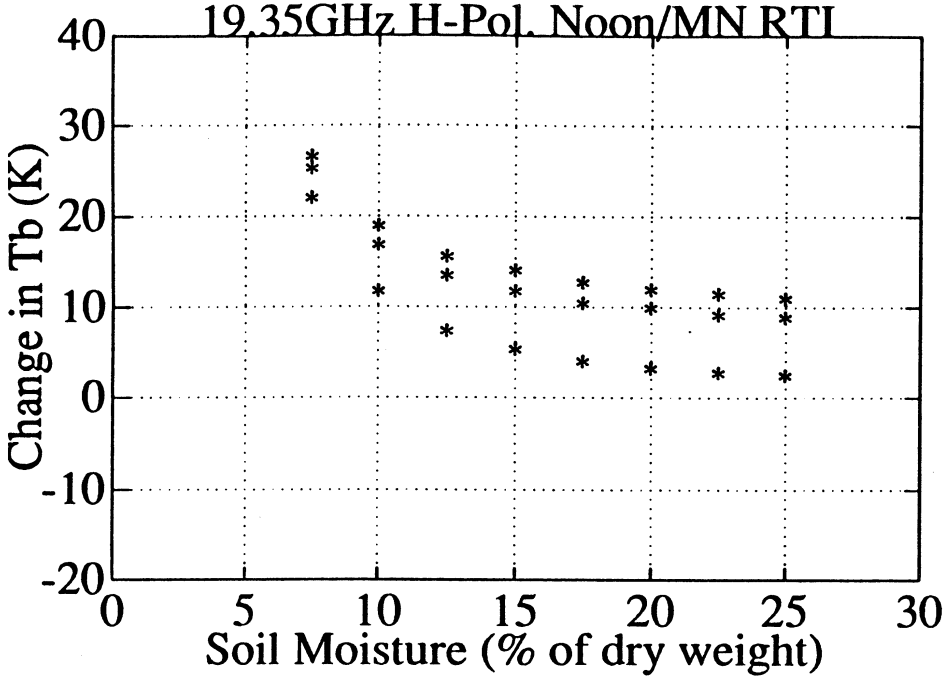
19.35GHz H-Pol. Noon/MN RTI
Change in Tb (K)
Soil Moisture (% of dry weight)

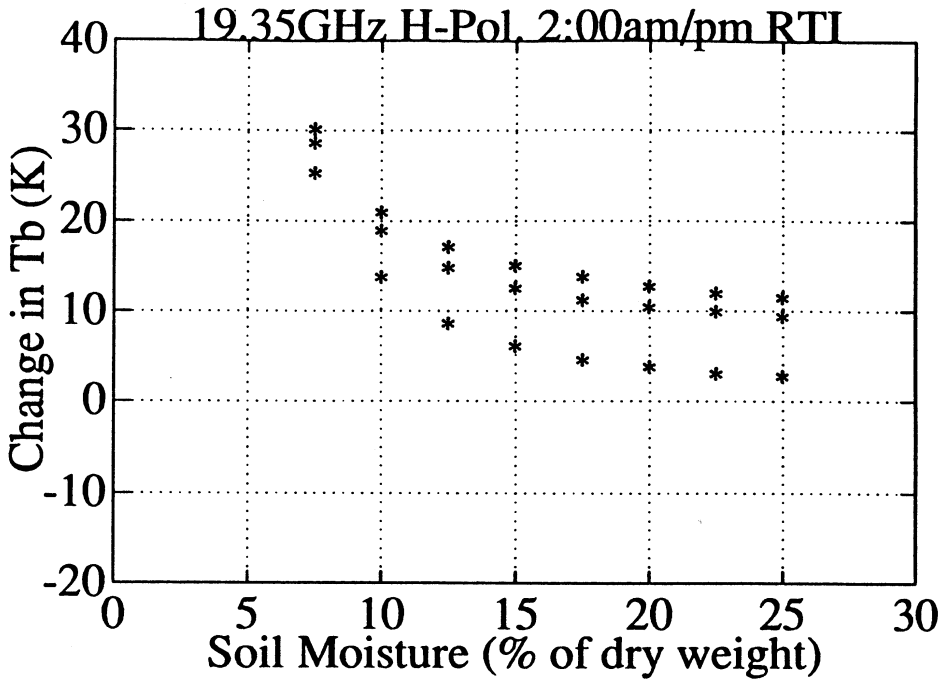
19.35GHz H-Pol. 2:00am/pm RTI
Change in Tb (K)
Soil Moisture (% of dry weight)

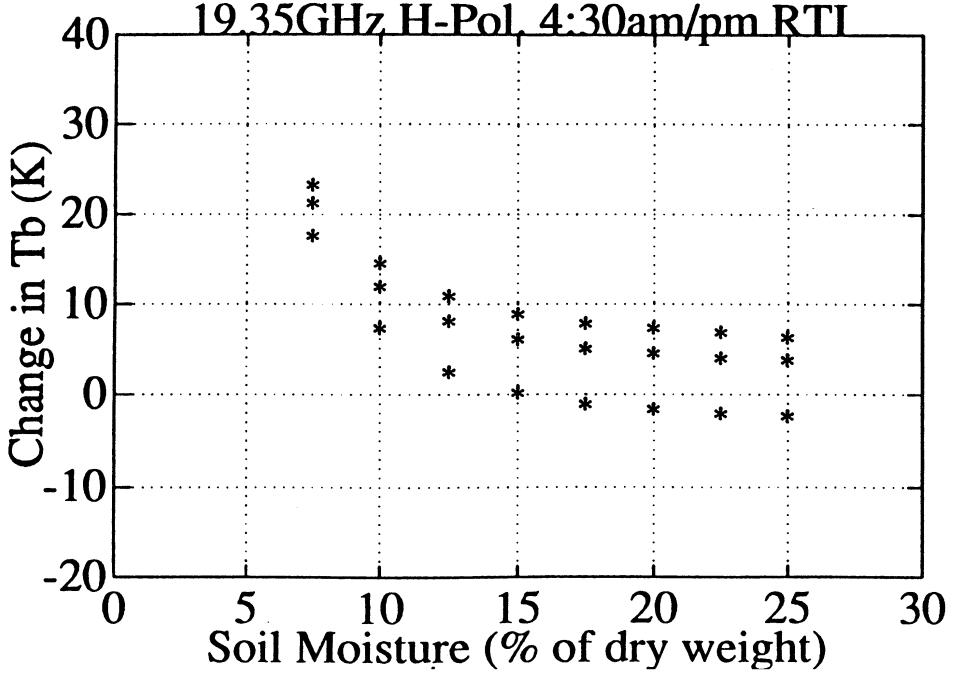
19.35GHz H-Pol. 4:30am/pm RTI
Change in Tb (K)
Soil Moisture (% of dry weight)

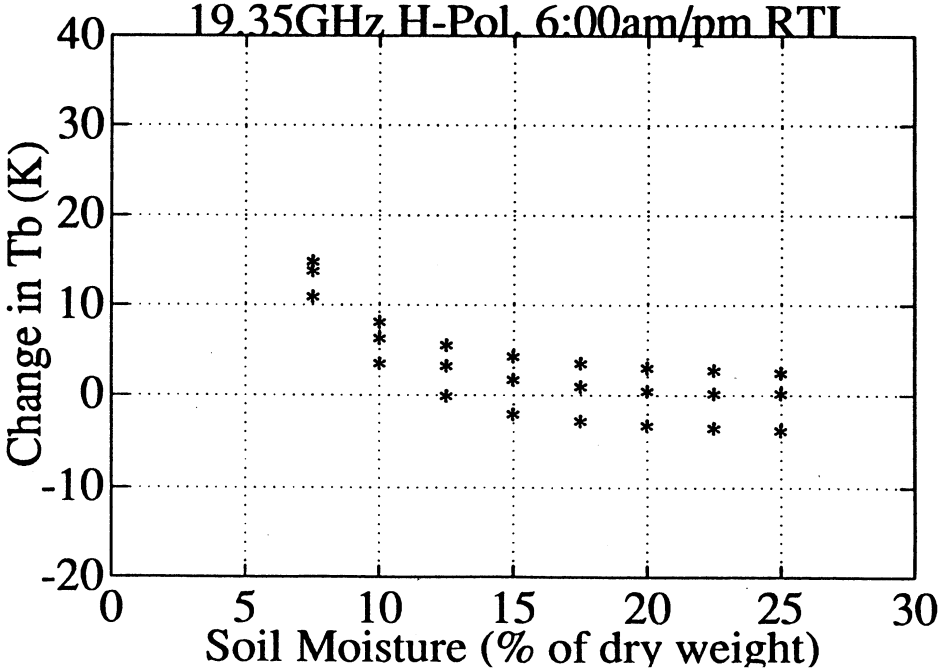
19.35GHz H-Pol. 6:00am/pm RTI
Change in Tb (K)
Soil Moisture (% of dry weight)

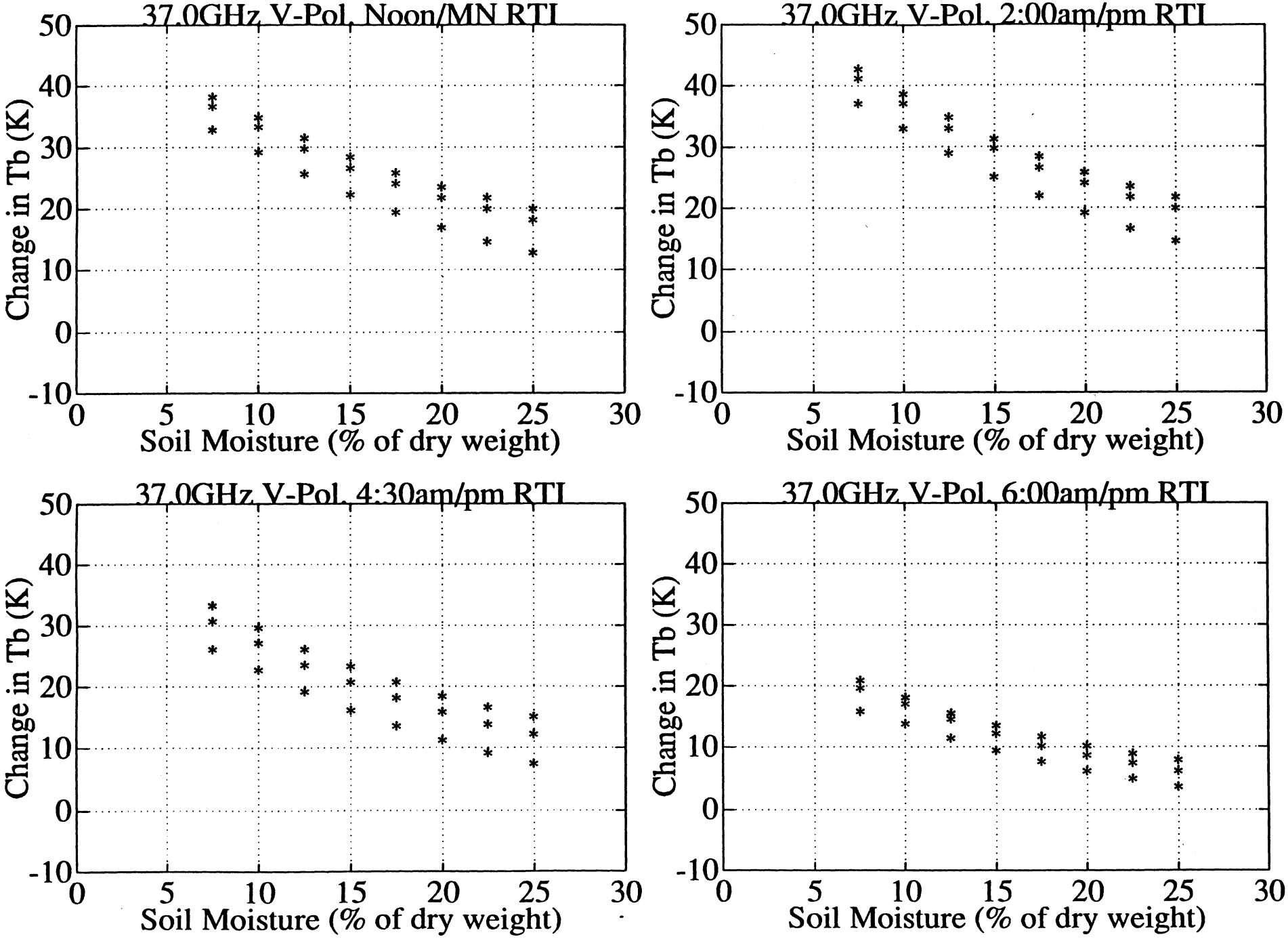
37.0GHz V-Pol, Noon/MN RTI
37.0GHz V-Pol, 2:00am/pm RTI
37.0GHz V-Pol, 4:30am/pm RTI
37.0GHz V-Pol, 6:00am/pm RTI
Change in Tb (K)
Soil Moisture (% of dry weight)
50
40
30
20
10
0
-10
0
5
10
15
20
25
30

Fig. 14

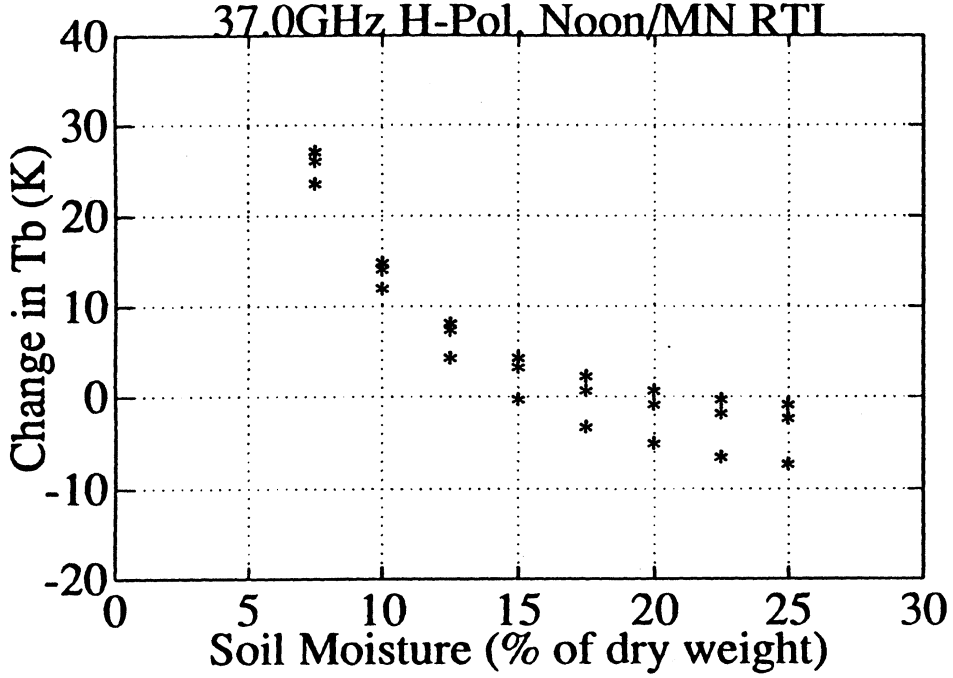
37.0GHz H-Pol, Noon/MN RTI
Change in Tb (K)
Soil Moisture (% of dry weight)

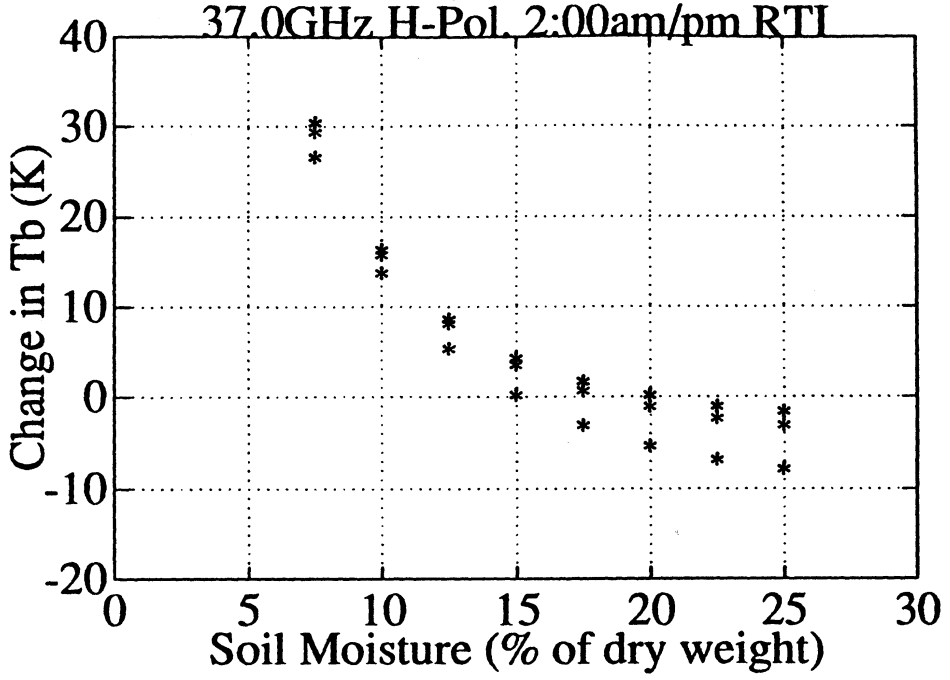
37.0GHz H-Pol, 2:00am/pm RTI
Change in Tb (K)
Soil Moisture (% of dry weight)

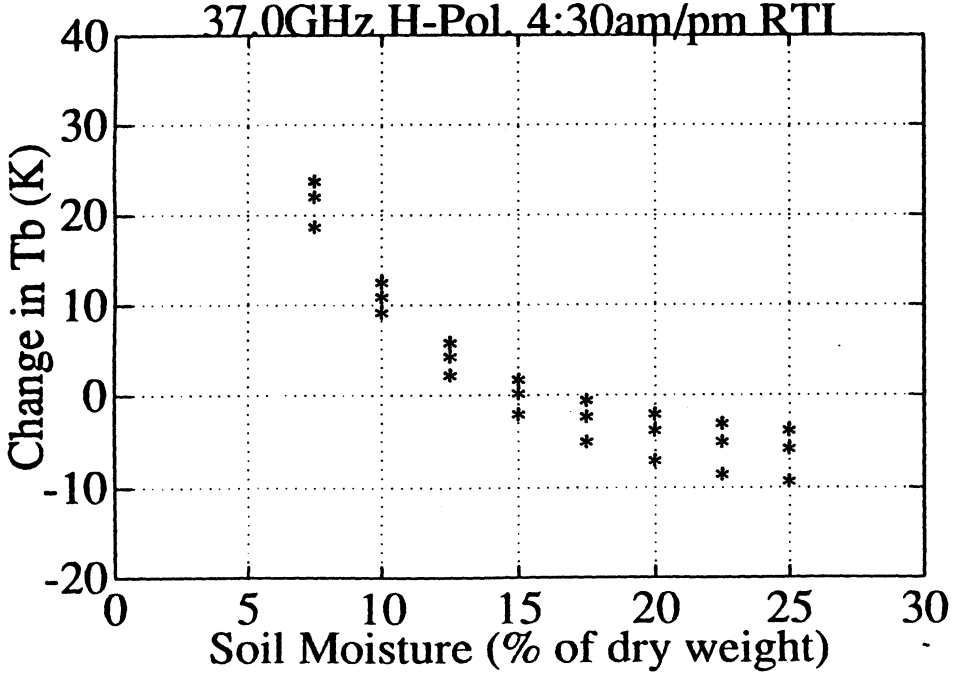
37.0GHz H-Pol, 4:30am/pm RTI
Change in Tb (K)
Soil Moisture (% of dry weight)

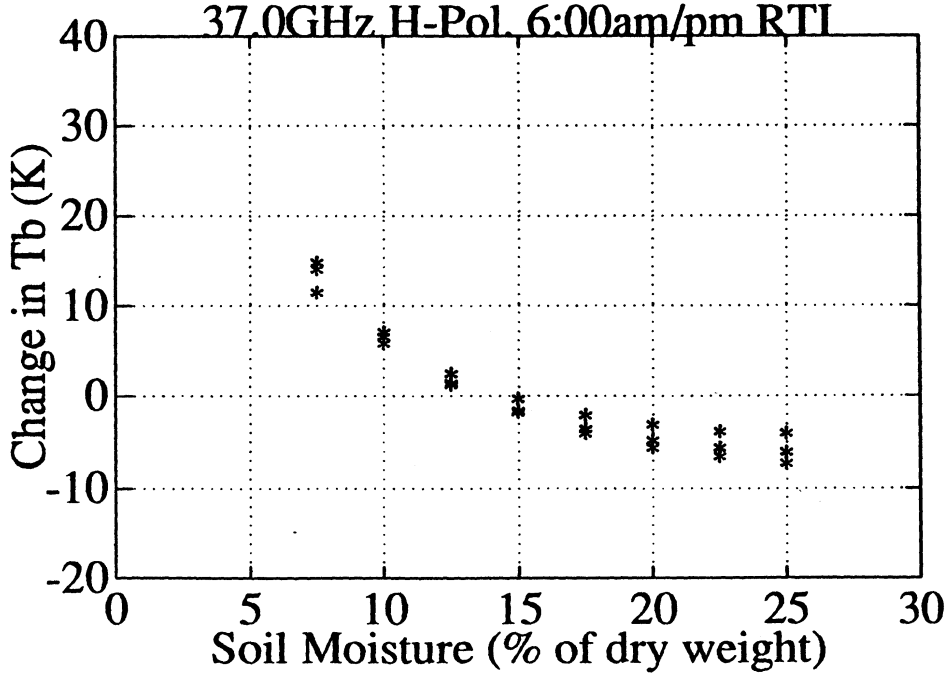
37.0GHz H-Pol, 6:00am/pm RTI
Change in Tb (K)
Soil Moisture (% of dry weight)

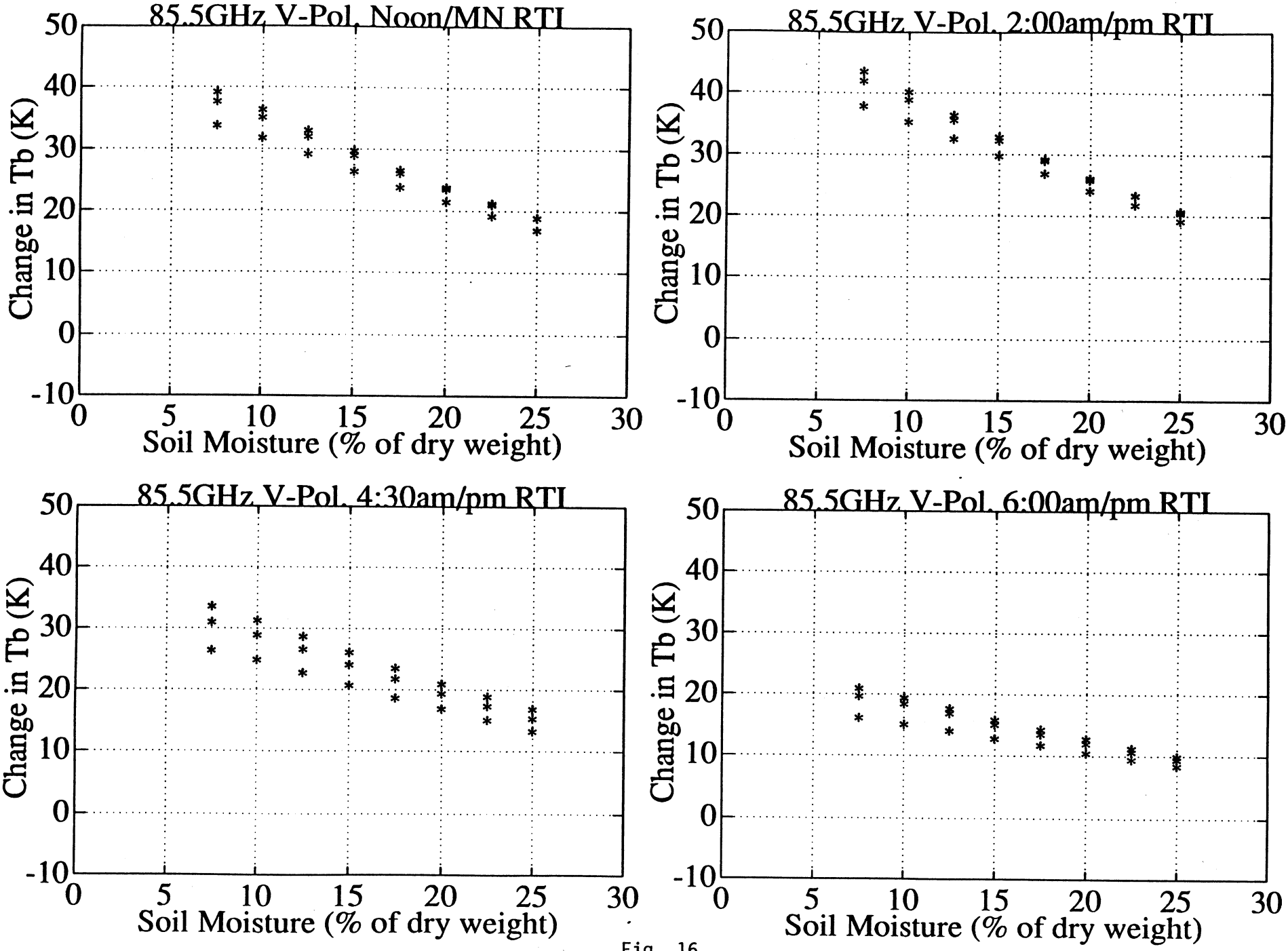
85.5GHz V-Pol, Noon/MN RTI
85.5GHz V-Pol, 2:00am/pm RTI
85.5GHz V-Pol, 4:30am/pm RTI
85.5GHz V-Pol, 6:00am/pm RTI
Change in Tb (K)
Soil Moisture (% of dry weight)
50
40
30
20
10
0
-10
0
5
10
15
20
25
30

Fig. 16

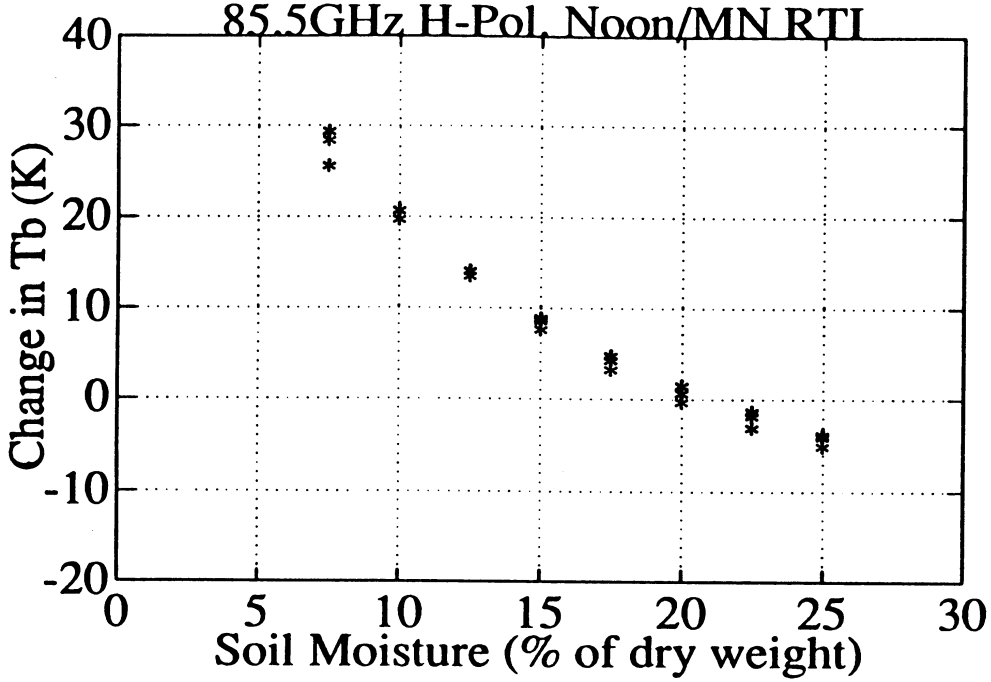
85.5GHz H-Pol, Noon/MN RTI
Change in Tb (K)
Soil Moisture (% of dry weight)
40
30
20
10
0
-10
-20
0
5
10
15
20
25
30

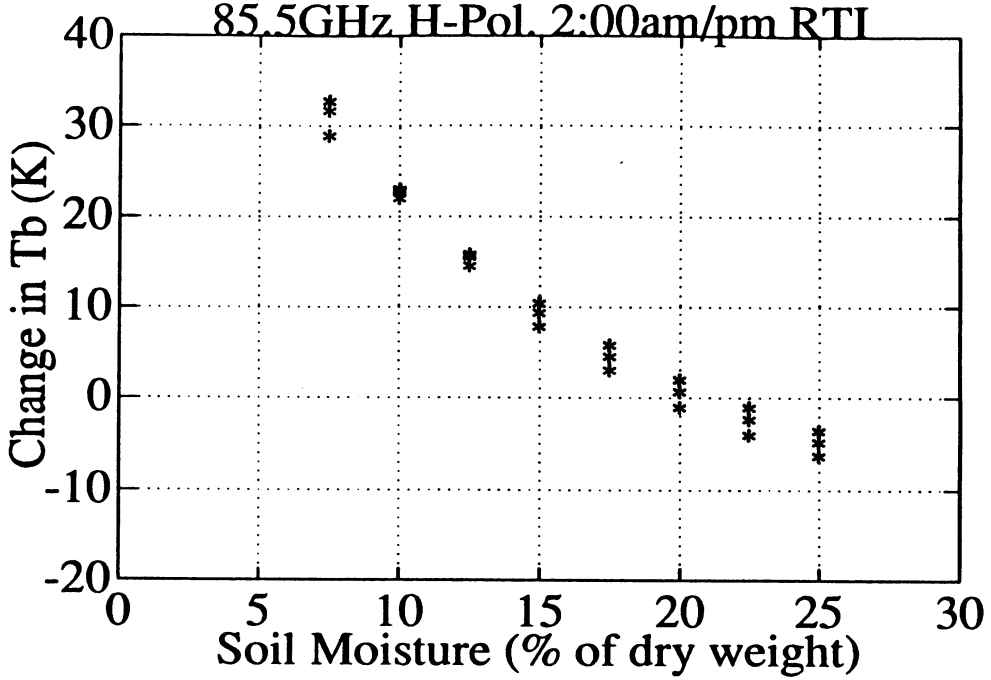
85.5GHz H-Pol, 2:00am/pm RTI
Change in Tb (K)
Soil Moisture (% of dry weight)
40
30
20
10
0
-10
-20
0
5
10
15
20
25
30

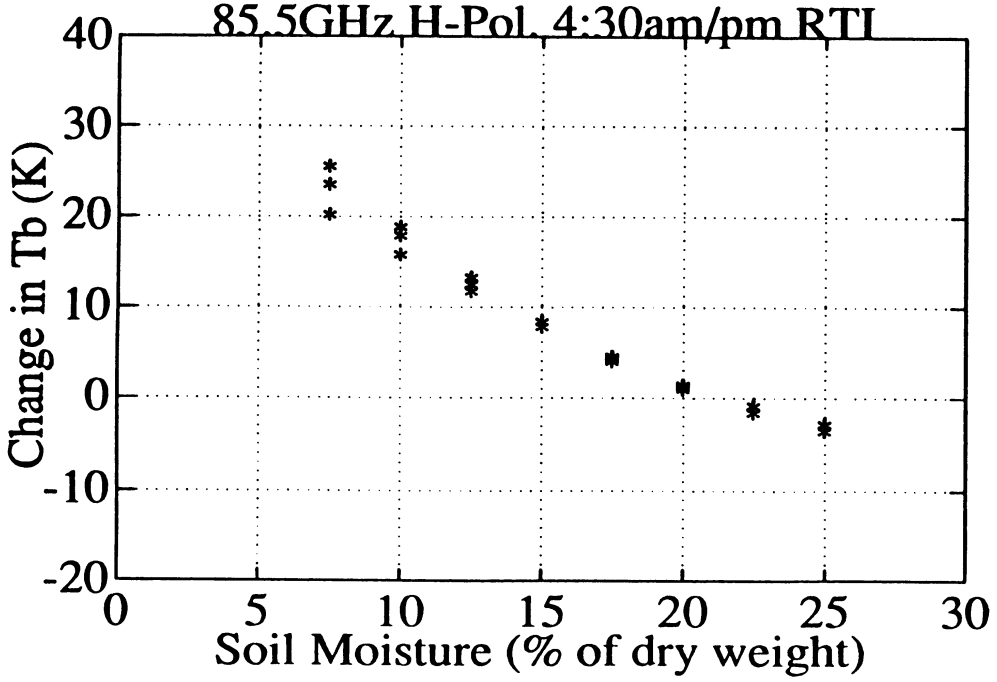
85.5GHz H-Pol, 4:30am/pm RTI
Change in Tb (K)
Soil Moisture (% of dry weight)
40
30
20
10
0
-10
-20
0
5
10
15
20
25
30

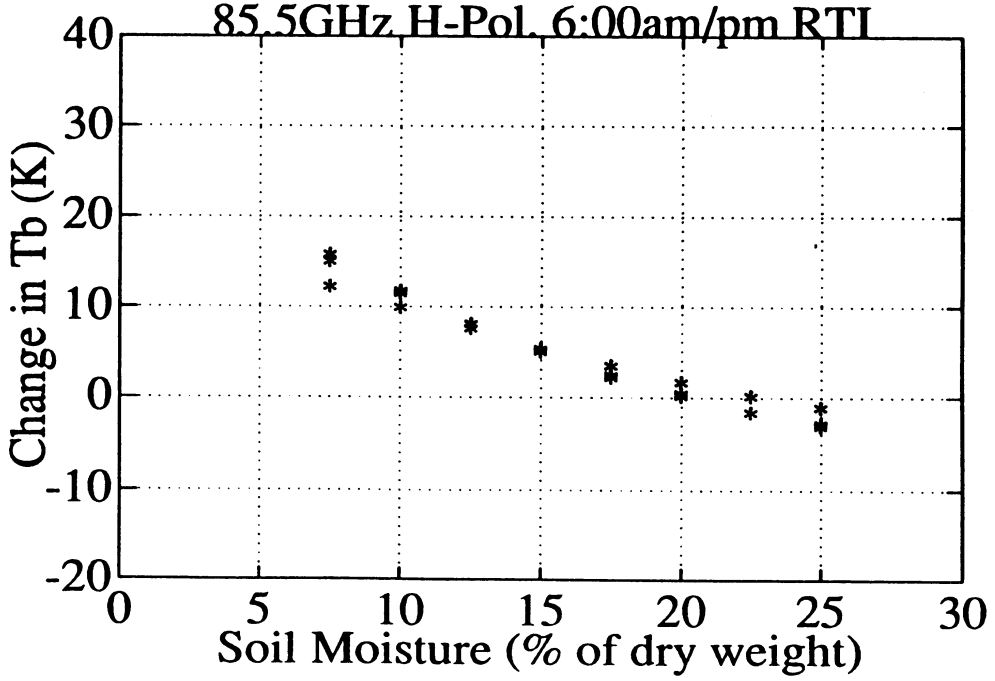
85.5GHz H-Pol, 6:00am/pm RTI
Change in Tb (K)
Soil Moisture (% of dry weight)
40
30
20
10
0
-10
-20
0
5
10
15
20
25
30

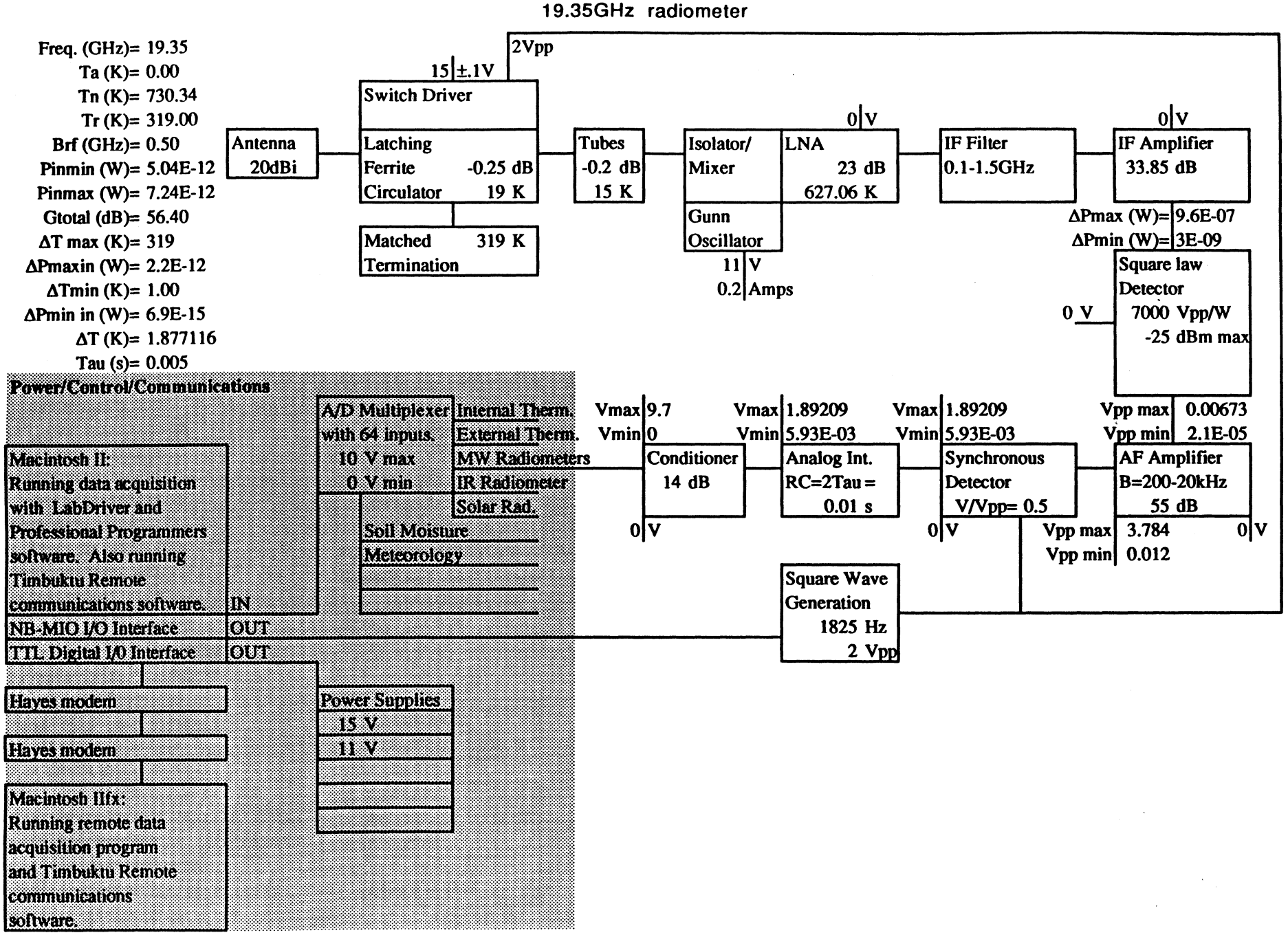
19.35GHz radiometer
Freq. (GHz)= 19.35
Ta (K)= 0.00
Tn (K)= 730.34
Tr (K)= 319.00
Brf (GHz)= 0.50
Pinmin (W)= 5.04E-12
Pinmax (W)= 7.24E-12
Gtotal (dB)= 56.40
ΔT max (K)= 319
ΔPmaxin (W)= 2.2E-12
ΔTmin (K)= 1.00
ΔPmin in (W)= 6.9E-15
ΔT (K)= 1.877116
Tau (s)= 0.005
2Vpp
15 ±.1V
Switch Driver
Antenna 20dBi
Latching Ferrite Circulator -0.25 dB 19 K
Matched Termination 319 K
Tubes -0.2 dB 15 K
Isolator/ Mixer
Gunn Oscillator
11 V
0.2 Amps
0 V
LNA 23 dB 627.06 K
IF Filter 0.1-1.5GHz
0 V
IF Amplifier 33.85 dB
ΔPmax (W)= 9.6E-07
ΔPmin (W)= 3E-09
Square law Detector
0 V
7000 Vpp/W
-25 dBm max
Vpp max 0.00673
Vpp min 2.1E-05
AF Amplifier B=200-20kHz 55 dB
Vpp max 3.784
Vpp min 0.012
0 V
Synchronous Detector V/Vpp= 0.5
0 V
Vmax 1.89209
Vmin 5.93E-03
Analog Int. RC=2Tau = 0.01 s
Vmax 1.89209
Vmin 5.93E-03
Conditioner 14 dB
0 V
Vmax 9.7
Vmin 0
A/D Multiplexer with 64 inputs. 10 V max 0 V min
Internal Therm.
External Therm.
MW Radiometers
IR Radiometer
Solar Rad.
Soil Moisture
Meteorology
Square Wave Generation 1825 Hz 2 Vpp
Power/Control/Communications
Macintosh II: Running data acquisition with LabDriver and Professional Programmers software. Also running Timbuktu Remote communications software.
IN
NB-MIO I/O Interface
OUT
TTL Digital I/O Interface
OUT
Hayes modem
Hayes modem
Macintosh IIfx: Running remote data acquisition program and Timbuktu Remote communications software.
Power Supplies
15 V
11 V

Fig. 18

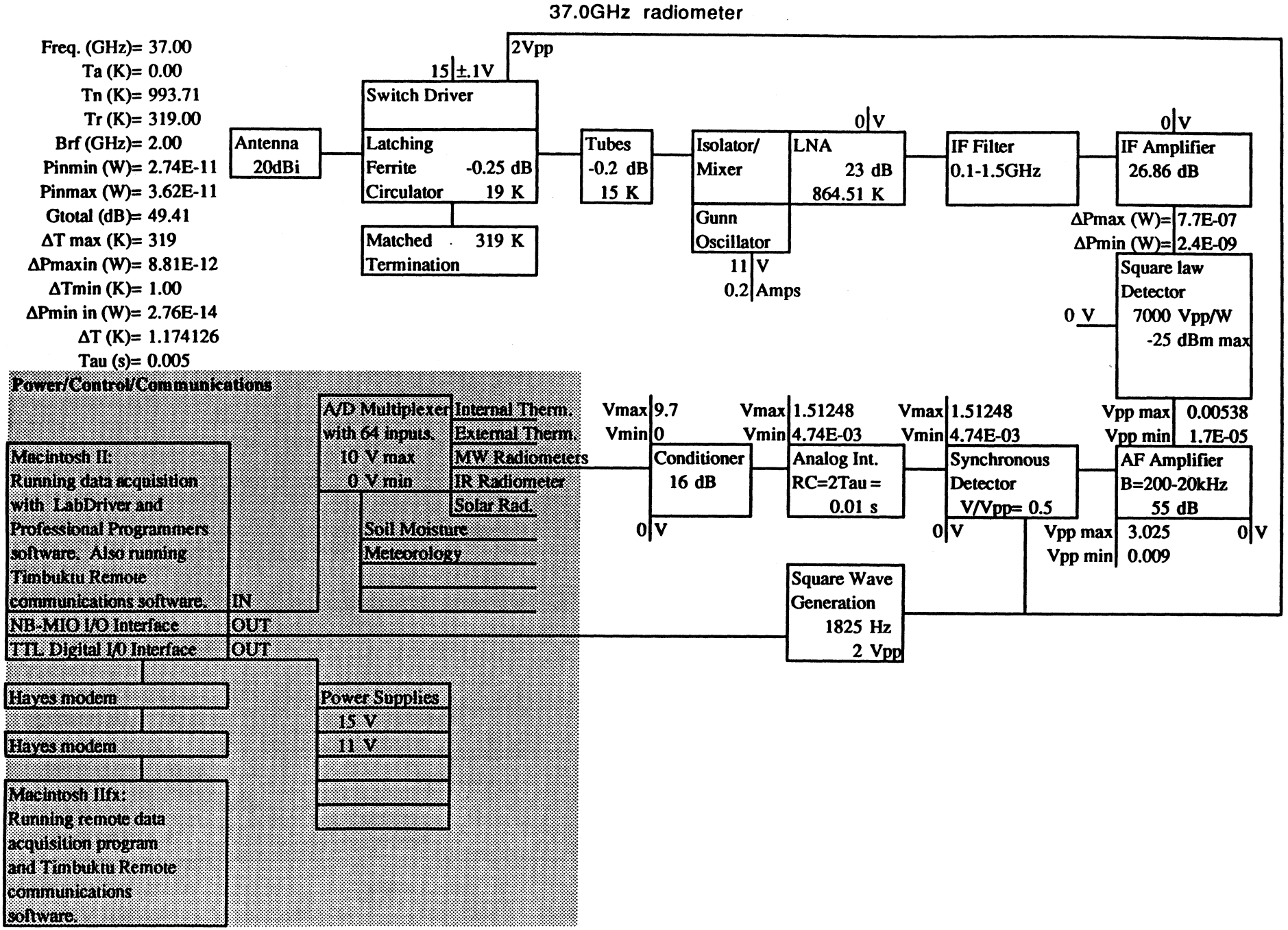
37.0GHz radiometer
Freq. (GHz)= 37.00
Ta (K)= 0.00
Tn (K)= 993.71
Tr (K)= 319.00
Brf (GHz)= 2.00
Pinmin (W)= 2.74E-11
Pinmax (W)= 3.62E-11
Gtotal (dB)= 49.41
ΔT max (K)= 319
ΔPmaxin (W)= 8.81E-12
ΔTmin (K)= 1.00
ΔPmin in (W)= 2.76E-14
ΔT (K)= 1.174126
Tau (s)= 0.005
2Vpp
15 ±.1V
Switch Driver
Antenna 20dBi
Latching Ferrite Circulator -0.25 dB 19 K
Matched Termination 319 K
Tubes -0.2 dB 15 K
0 V
Isolator/ Mixer
LNA 23 dB 864.51 K
Gunn Oscillator
11 V
0.2 Amps
IF Filter 0.1-1.5GHz
0 V
IF Amplifier 26.86 dB
ΔPmax (W)= 7.7E-07
ΔPmin (W)= 2.4E-09
Square law Detector 7000 Vpp/W -25 dBm max
0 V
Vpp max 0.00538
Vpp min 1.7E-05
Power/Control/Communications
A/D Multiplexer with 64 inputs. 10 V max 0 V min
Internal Therm.
External Therm.
MW Radiometers
IR Radiometer
Solar Rad.
Soil Moisture
Meteorology
Vmax 9.7
Vmin 0
Conditioner 16 dB
0 V
Vmax 1.51248
Vmin 4.74E-03
Analog Int. RC=2Tau = 0.01 s
Vmax 1.51248
Vmin 4.74E-03
Synchronous Detector V/Vpp= 0.5
0 V
AF Amplifier B=200-20kHz 55 dB
Vpp max 3.025
Vpp min 0.009
0 V
Square Wave Generation 1825 Hz 2 Vpp
Macintosh II: Running data acquisition with LabDriver and Professional Programmers software. Also running Timbuktu Remote communications software.
IN
NB-MIO I/O Interface
OUT
TTL Digital I/O Interface
OUT
Hayes modem
Hayes modem
Macintosh IIfx: Running remote data acquisition program and Timbuktu Remote communications software.
Power Supplies
15 V
11 V

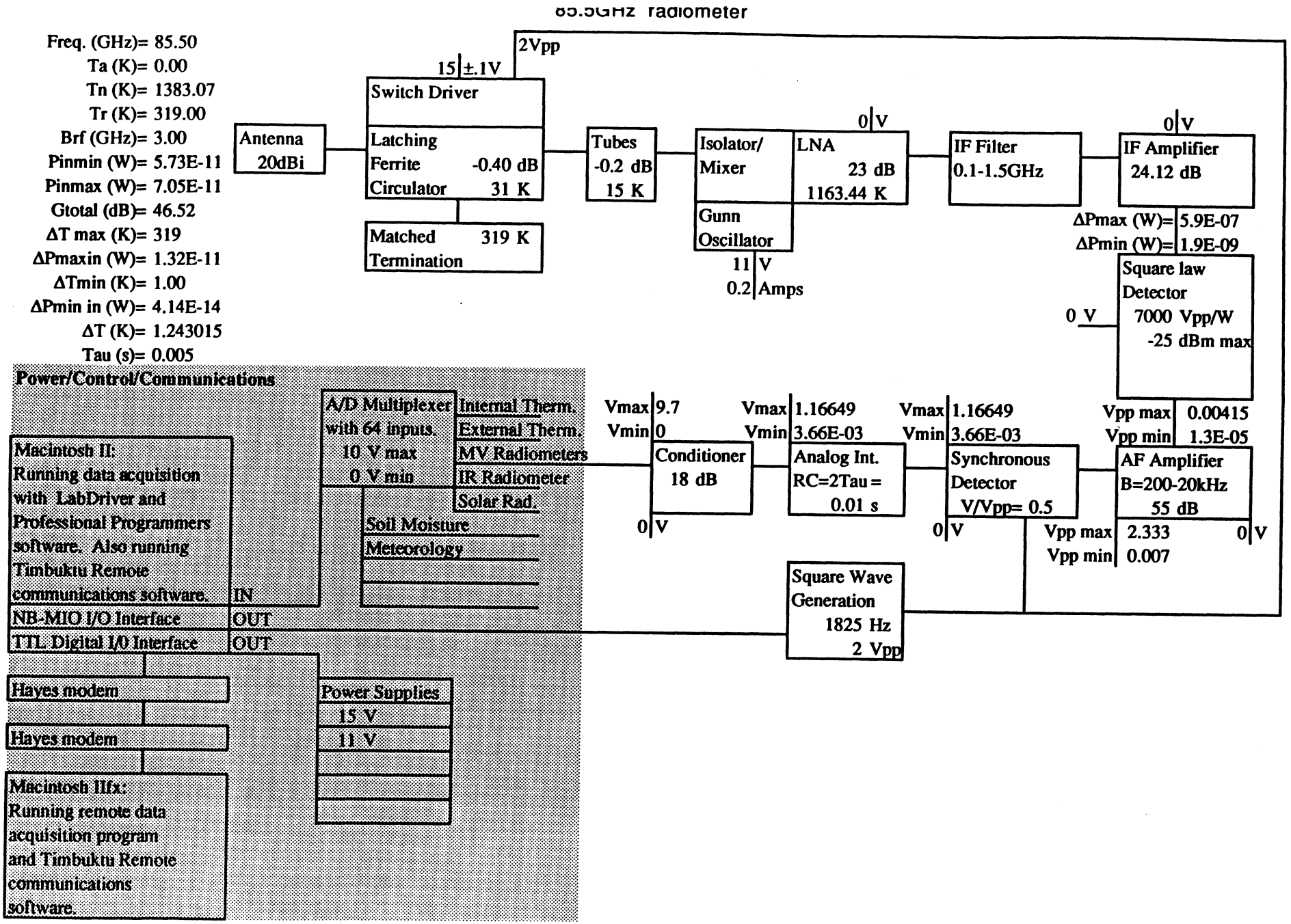
85.5GHz radiometer
Freq. (GHz)= 85.50
Ta (K)= 0.00
Tn (K)= 1383.07
Tr (K)= 319.00
Brf (GHz)= 3.00
Pinmin (W)= 5.73E-11
Pinmax (W)= 7.05E-11
Gtotal (dB)= 46.52
ΔT max (K)= 319
ΔPmaxin (W)= 1.32E-11
ΔTmin (K)= 1.00
ΔPmin in (W)= 4.14E-14
ΔT (K)= 1.243015
Tau (s)= 0.005
Antenna 20dBi
15 ±.1V
2Vpp
Switch Driver
Latching Ferrite Circulator -0.40 dB 31 K
Matched Termination 319 K
Tubes -0.2 dB 15 K
Isolator/ Mixer
Gunn Oscillator
11 V
0.2 Amps
0 V
LNA 23 dB 1163.44 K
IF Filter 0.1-1.5GHz
0 V
IF Amplifier 24.12 dB
ΔPmax (W)= 5.9E-07
ΔPmin (W)= 1.9E-09
Square law Detector
0 V
7000 Vpp/W
-25 dBm max
Power/Control/Communications
A/D Multiplexer with 64 inputs. 10 V max 0 V min
Internal Therm.
External Therm.
MV Radiometers
IR Radiometer
Solar Rad.
Soil Moisture
Meteorology
Macintosh II: Running data acquisition with LabDriver and Professional Programmers software. Also running Timbuktu Remote communications software.
IN
NB-MIO I/O Interface
OUT
TTL Digital I/0 Interface
OUT
Hayes modem
Hayes modem
Macintosh IIfx: Running remote data acquisition program and Timbuktu Remote communications software.
Power Supplies
15 V
11 V
Vmax 9.7
Vmin 0
Conditioner 18 dB
0 V
Vmax 1.16649
Vmin 3.66E-03
Analog Int. RC=2Tau = 0.01 s
Vmax 1.16649
Vmin 3.66E-03
Synchronous Detector V/Vpp= 0.5
0 V
Vpp max 0.00415
Vpp min 1.3E-05
AF Amplifier B=200-20kHz 55 dB
Vpp max 2.333
Vpp min 0.007
0 V
Square Wave Generation 1825 Hz 2 Vpp

Fig. 20

Radiobrightness of Diurnally Heated, Freezing Soil

ANTHONY W. ENGLAND, SENIOR MEMBER, IEEE

Abstract—Freezing and thawing soils exhibit unique radiometric characteristics. To examine these characteristics, diurnal insolation is modeled as one-dimensional heating of a moist soil half-space during a typical fall at a northern Great Plains site (Bismarck, ND). The one-dimensional heat flow equation is nonlinear because both the enthalpy (the change in internal energy with temperature at constant pressure) and the thermal conductivity of freezing soils are nonlinear functions of temperature. The problem is particularly difficult because phase boundaries propagate in time, and because soils, particularly clay-rich soils, freeze over a range of temperatures rather than at 0°C—that is, they possess diffuse phase boundaries. A modified Chernous'ko method was used to integrate the heat flow equation to obtain monthly thermal models during a typical September through December period. Diurnal radiobrightness curves at 10.7, 18, and 37 GHz were computed for each month. The 37-GHz radiobrightness best tracks soil surface temperature; the 10.7–37-GHz spectral gradient of thawed soils is strongly positive; the spectral gradient of frozen soils is slightly negative; and the midnight-to-noon spectral gradient is shifted by approximately +0.1 K/GHz by diurnal changes in the surface temperature and the thermal gradient. These observations support the use of the scanning multichannel microwave radiometer 37-GHz radiobrightness and its 10.7–37-GHz spectral gradient as discriminants in a frozen soil classifier for high latitude prairie.

I. Introduction

THE QUANTITY and physical state (i.e., frozen or liquid) of moisture in soil can be estimated from satellite radiobrightness signatures. A large body of literature links moisture content to radiobrightness [1]–[6]. Whether or not moisture in the soil is frozen affects the rate of energy transfer to the atmosphere by limiting evapotranspiration and affects the rainfall or snowmelt runoff potential by reducing the infiltration capacity of the soil. Zuerndorfer *et al.* [7] produced freeze/thaw maps of the northern Great Plains from Nimbus 7 scanning multichannel microwave radiometer (SMMR) data. This paper is an examination of the theoretical basis for microwave radiometric, frozen soil classification.

For the purposes of this paper, moist soil is defined as frozen when its dielectric properties are essentially those of dry soil. This characteristic of frozen soil is discussed in the section on radiobrightness. Fig. 1(a) and (b) illustrate the observational basis for a frozen soil classifier. A 37-GHz radiobrightness below about 247 K indicates frozen soil, and one above about 247 K indicates thawed soil for Bismarck, ND. However, regions near the Missouri River, Sakakawea and Devils Lakes, the Red River Valley, and in the wake of a regional rainfall often appear anomalously cold at 37 GHz because of exceptional wetness for the northern Great Plains. The confusing factor is that 37 GHz radiobrightness, while least sensitive to moisture of the SMMR frequencies, is, nevertheless, darkened by moisture. A second discriminant—the 10.7–37 GHz spectral gradient, i.e., $\partial T_b/\partial f$ where T_b is radiobrightness temperature at frequency f—generally resolves the ambiguity between frozen and wet soils because frozen soils have negative spectral gradients, and cool moist soils have positive spectral gradients. Note, also, that Fig. 1(a) and (b) exhibit an upward shift in the spectral gradient between midnight and noon of about 0.1 K/GHz. A valid theoretical model should replicate the behavior of the 37-GHz radiobrightness, the dominant characteristics of the 10.7–18–37-GHz spectral gradient, and the diurnal shifts in the spectral gradient during the September through December months in the northern Great Plains.

Manuscript received November 13, 1989; revised March 14, 1990. This work was partially supported by NASA Interdisciplinary Research Program Grant NAG5-852.

The author is with the Radiation Laboratory, Department of Electrical Engineering and Computer Science, University of Michigan, Ann Arbor, MI 48109-2122.

IEEE Log Number 9036332.

II. One-Dimensional Heat Flow

The one-dimensional heat flow equation for temperature T (K), depth z (m), and time t (s) is [8]

$$\partial E(T)/\partial t = -\partial F(z, t)/\partial z \tag{1}$$

where $E(T)$ is the enthalpy ($J \cdot m^{-3}$) and $F(z, t)$ is the heat flux density ($W \cdot m^{-2}$) (T is a function of z and t). Heat flux density is linearly related to the temperature gradient $\partial T/\partial z$ by

$$F(z, t) = -K(T)(\partial T/\partial z) \tag{2}$$

where $K(T)$ is thermal conductivity ($W\text{-}m^{-1}\text{-}K^{-1}$). That is,

$$\frac{\partial E(T)}{\partial t} = \frac{\partial}{\partial z}\left(K(T)\frac{\partial T}{\partial z}\right). \tag{3}$$

With respect to a reference temperature T_0, $E(T)$ is generally the linear function

$$E(T) = \rho c_p\{T - T_0\} \tag{4}$$

where ρ is density ($kg\text{-}m^{-3}$), and c_p is specific heat at constant pressure ($J\text{-}kg^{-1}\text{-}K^{-1}$). If $K(T)$ is constant, (3) becomes the parabolic linear differential equation

$$\partial T/\partial t = \kappa(\partial^2 T/\partial z^2) \tag{5}$$

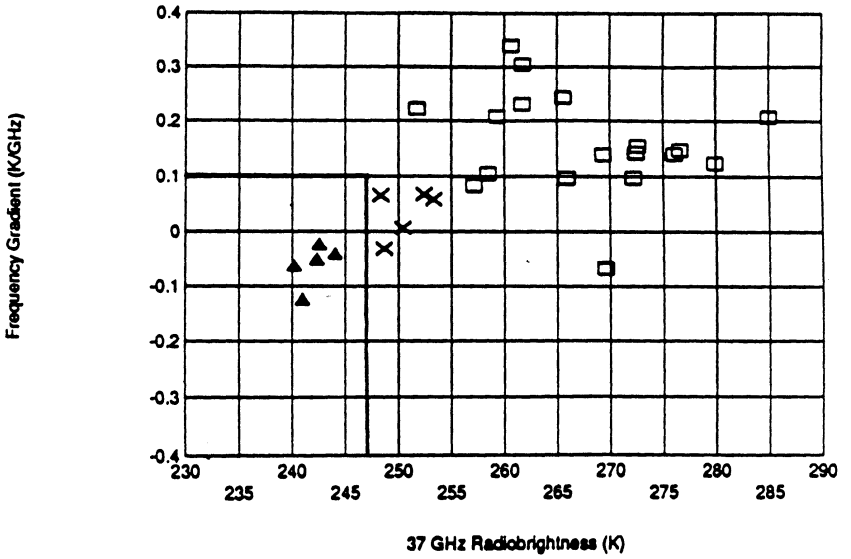

(a)

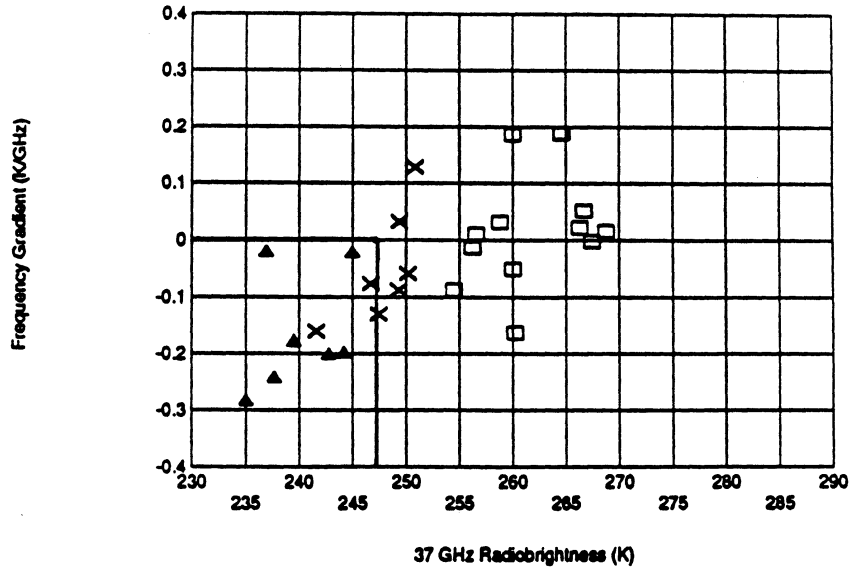

(b)

Fig. 1. Frequency gradient versus SMMR 37-GHz brightness temperature, Bismarck, ND. Data were collected from 8/1/84 through 12/31/84. Shown with Bismarck data are clustering decision thresholds for frozen, mixed, or thawed surface. Based upon ground data, solid triangles are frozen, open boxes are thawed, and ×'s are mixed pixels (personal communication from Zuerndorfer, modified from Zuerndorfer *et al.* [7]). (a) Day. (b) Night.

where κ is thermal diffusivity (m^2/s)

$$\kappa = K/\rho c_p. \tag{6}$$

Equation (5) can be solved analytically by either the harmonic or the Laplace methods [8], or by a finite difference numerical method. Watson used the Laplace method [9], [10], and Kahle used the finite difference method [11] to develop thermal models for the diurnal insolation of rock and soil. Their models relate day–night differences in thermal infrared temperature to rock and soil type. However, if soils freeze or thaw diurnally, then (3) is neither linear nor amenable to either the Watson or the Kahle methods.

Equation (3) looks simpler with the substitution of variables

$$u = \int_{T_0}^{T} K(\tau)\, d\tau \tag{7}$$

so that $u = u(T)$ and (3) becomes

$$\partial E(T)/\partial t = \partial^2 u/\partial z^2. \tag{8}$$

This one-dimensional nonlinear (in T) heat flow equation is called Stefan's problem [12], and there are three ways to solve it: the finite difference method [13], the moving boundary method [14], and the isotherm propagation or

Chernous'ko method [15]. The finite difference method for nonlinear problems suffers from uncertain convergence properties. The moving boundary method involves seeking analytical solutions to the linear regions on either side of moving phase boundaries. This method is particularly awkward if the phase change occurs over a finite depth, as in freezing soils, rather than at a plane interface, or if there are multiple freezing isotherms, as in the periodic heating case. The original Chernous'ko method also has difficulty with the periodic heating case.

Chernous'ko [15] replaced $E(T)$ with the piecewise constant approximation $H(T)$, shown schematically in Fig. 2(a), so that

$$H(T) = E(T_n), \qquad \text{for } T_n \le T < T_{n+1} \tag{9}$$

where T_n denotes isotherm n ordered by increasing depth. While these isotherms can be any temperature, integer values of Kelvin were used in the model. The slope of the linear portions of $E(T)$ below 268 K and above 273 K are the ρc_p for frozen and moist soils, respectively. The increased slope between 268 and 273 K is a linear approximation to an energy term that includes the latent heat of melting of moisture in the soil. In this example, melting occurs over 5 K. For sandy soils, the range might be 1 K; for some clay soils, it might approach 10 K [16].

In terms of $H(T)$, (9) becomes

$$\partial H(T)/\partial t = \partial^2 u/\partial z^2. \tag{10}$$

Locally constant H requires that u be a linear function of z between isotherms T_n and T_{n+1}, i.e.,

$$u = u_n + \frac{u_{n+1} - u_n}{z_{n+1} - z_n}(z - z_n), \qquad \text{for } (z_n < z < z_{n+1}) \tag{11}$$

where z_n is the depth of isotherm T_n.

If the value of $H(T)$ at $z > z_n$ is denoted by H^+, and $H(T)$ at $z < z_n$ is H^-, then (10) can be integrated at constant time along path a–b in Fig. 3,

$$\frac{\partial}{\partial t}\int_a^b H(T)\,dz = \left(\frac{\partial u}{\partial z}\right)_{b,t} - \left(\frac{\partial u}{\partial z}\right)_{a,t} \tag{12}$$

to yield

$$\frac{\partial}{\partial t}\left[H^+(b - z_n) + H^-(z_n - a)\right] = \left(\frac{\partial u}{\partial z}\right)_{b,t} - \left(\frac{\partial u}{\partial z}\right)_{a,t}. \tag{13}$$

From (11), because z_n is the only function of time on the left of (13),

$$\frac{dz_n}{dt} = \frac{1}{(H^- - H^+)}\left\{\left(\frac{u_{n+1} - u_n}{z_{n+1} - z_n}\right) - \left(\frac{u_n - u_{n-1}}{z_n - z_{n-1}}\right)\right\}. \tag{14}$$

Equation (14) is the ordinary, linear differential equation that Chernous'ko used to propagate each isotherm in time.

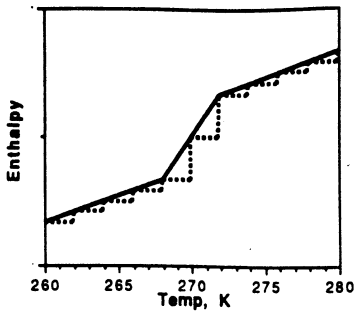

(a)

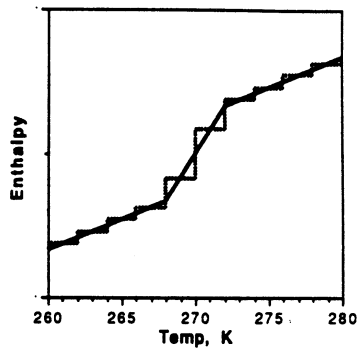

(b)

Fig. 2. Enthalpy versus temperature. $E(T)$ and $H(T)$ are approximations to moist soil enthalpy during freezing. (a) $H(T)$ represents Chernous'ko's, piecewise constant model. Asymmetry of $H(T)$ at each isotherm produces dissimilar heating and cooling performance. (b) $H(T)$ is modified model. Symmetry in $H(T)$ at each isotherm produces necessary similarity for heating and cooling. Solid line: $E(T)$. Dotted line $H(T)$.

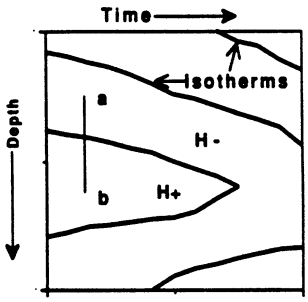

Fig. 3. Integration path at constant time. Piecewise constant approximation to $H(T)$ means that enthalpies, H^- and H^+, are constant between isotherms.

Equation (14) fails in the periodic heating problem because of an asymmetry in $H(T)$ between heating and cooling. For example, consider the propagation of isotherm z_n where $T_{n-1} < T_n = T_{n+1}$. In this case, $H^+ > H^-$ and

$$\frac{dz_n}{dt} = \frac{-1}{(H^- - H^+)}\left\{\left(\frac{u_n - u_{n-1}}{z_n - z_{n-1}}\right)\right\}. \tag{15}$$

However, if $T_{n-1} > T_n = T_{n+1}$, then $H^+ = H^-$ and dz_n/dz in (14) is undefined. This asymmetry can be ameliorated by substituting the piecewise constant $H(T)$

shown schematically in Fig. 2(b), i.e.,

$$H(T) = \begin{cases} \dfrac{E(T_n) + E(T_{n+1})}{2}, & \text{for } T_n < T < T_{n+1} \\ E(T_n), & \text{for } T = T_n \\ \dfrac{E(T_{n-1}) + E(T_n)}{2}, & \text{for } T_{n-1} < T < T_n \end{cases} \quad (16)$$

Isotherm propagation with this alternative approximation for $E(T)$ will be referred to as the modified Chernous'ko method.

III. Boundary Conditions

Watson [9] and Kahle [11] used boundary conditions for the energy flux $F_{net}(z)$,

$$F_{net}(0) = F_{sun} + F_{sky} + F_{wind} - F_{ground}$$
$$F_{net}(\infty) = 0 \quad (17)$$

where z at infinity means depths greater than the penetration of the diurnal thermal pulse. The parameters that comprise these boundary conditions for Bismarck, ND, are described in Table I. F_{sun} is insolation reduced by cloud cover, atmospheric absorption, albedo, and the cosine of the zenith angle. F_{sky} is sky brightness plus a small correction for cloud cover. F_{wind} is a small correction for sensible heat transfer between ground and air used by Kahle [11]. F_{ground} is gray-body emission from the soil's surface.

Topography, evapotranspiration, and sublimation are ignored in this model. Of these simplifications, evapotranspiration is potentially most limiting because, under some conditions, it can be a large upward term in the energy balance equation. However, it is a difficult process to model accurately. Until experimental radiometric data are available for freezing and thawing soils, it is better to note that a potentially important process is being ignored than to model the process poorly. Some justification exists for omitting evapotranspiration. During fall and early winter, lower thermal temperatures and dormant ground vegetation lead to lower evaporation rates. Also, thermal infrared emissivity e is assumed constant ($= 0.95$). Changes in moisture content do alter the thermal infrared emissivity of bare soil. However, the implicit model is of dormant prairie vegetation over a moist or frozen soil. How the effective thermal infrared emissivity will vary is not clear. Again, without experimental data, e is best assumed to be constant.

The process of propagating subsurface isotherms is begun with a constant subsurface temperature. An initial temperature that equals the equilibrium temperature at depth greatly reduces the computation time needed for a solution to converge. Such an initial temperature T_{0g} satisfies

$$e\sigma T_{0g}^4 = \frac{1}{24}\int_{24h}(F_{sun} + F_{sky})\,dt \quad (18)$$

TABLE I
Boundary Parameters

F_{sun}	solar irradiance $= f_1 S_0(1 - A)M(\phi)\cos\phi$
F_{sky}	sky irradiance $= \sigma T_{sky}^4 + f_2$
F_{wind}	sensible heat transfer from air to ground $\rho_a c_a C_d (W + 2)(T_{air} - T_{ground})$
F_{ground}	$e\sigma T_g^4$
S_0	solar constant $= 1385$ W/m^2
A	albedo
$M(\phi)$	approximate atmospheric transmissivity $1.0\text{-}0.2(\cos\phi)^{-0.5}$ [9], [10]
ϕ	zenith angle
$\cos\phi$	$\cos\lambda\cos\delta(-\cos(2\pi\ \text{hour}/24) + \sin\lambda\sin\delta)$ if >0, otherwise $\cos\phi = 0$
λ	local latitude
δ	declination $= -23.433° \cos(2\pi\ \text{month}/12)$
f_1	$\approx (1 - \text{cl})$ where cl is average land cover (approximation is that some is regained through f_2)
f_2	irradiance from clouds, approximated as half average solar irradiance lost in cloud term, f_1 $(\text{cl}/2)S_0(1 - A)\{\int M(\phi)\cos\phi\,dt\}/24$
σ	Stefan-Boltzmann constant $= 5.6696\text{E-}8$ W-m^{-2}-K^{-4}
T_{air}	average air temperature $T_{0air} - T_{del}\cos(2\pi(\text{hour} - 2)/24)$ [11]
T_{0air}	monthly average air temperature (e.g., see Fig. 6) $T_0 - T_1\cos(2\pi(\text{month} - \theta_{lag})/12)$
T_{del}	diurnal variation (from meteorological reports)
T_{sky}	$T_{air}(0.61 + 0.05w^{0.5})^{0.25}$ (Brunt's formula, from Kahle [11])
w	water vapor pressure, mmHg
ρ_a	air density at surface $= 1.25$ kg/m^3
c_a	specific heat of dry air $= 1.0\text{E} + 3$ J/kg-K
C_d	drag coefficient $= 0.002 + 0.006(Z/5000)$, Z is elevation in meters [11]
W	wind velocity in m/s
e	thermal infrared emissivity
T_g	soil surface temp from solution to heat flow equation

where e is thermal infrared emissivity and σ is the Stefan–Boltzmann constant. Initial isotherms at temperature T_{0g} were assigned at 1 cm depth intervals to a depth of 50 cm. Propagation time intervals could be varied but were typically 6 s. That is, every 6 s for 24 h, each of the 50 isotherms was propagated according to (14). The time interval was chosen to be short enough so that no isotherms crossed. If an isotherm propagated to within a preassigned distance Δ (e.g., $\Delta = 1$ mm), of an identical isotherm (dissimilar isotherms tend to move apart), or to within Δ of the surface, that isotherm was dropped, and the remaining isotherms were renumbered. Following isotherm propagation, the surface thermal gradient was established through a combination of $F_{net}(0)$ and (2) for the depth interval between the most shallow isotherm and the surface. This thermal gradient fixed a new surface temperature. If the temperature difference between the new surface temperature and the first isotherm was greater than $\delta u = u_1 - u_0$ (e.g., >1 K), then a new isotherm was assigned at a proportional depth between the surface and the previously first isotherm, and, again, the isotherms were renumbered. A 51st isotherm was assigned a temperature equal to that of the 50th isotherm so that $F_{net}(\infty) = 0$. However, because the initial temperature was the equilibrium temperature, the thermal pulse never reached the 50th isotherm. After each 24-h period, surface temperatures at 1-min intervals were compared with equiva-

lent temperatures for the previous 24-h iteration. The process was repeated until none of the 60 × 24 temperatures differed for any 24-h interval by more than 0.001 K. Convergence generally required between 8 and 11 iterations.

IV. Radiobrightness

The radiative transfer equation [22] for the microwave spectral intensity $I_\lambda^-(z, \mu')$ at free-space wavelength λ_0, at depth z in soil (Fig. 4), and in direction $\mu' = \cos\theta'$ (μ' positive means upward) is

$$\mu' \frac{dI_\lambda^-(z, \mu')}{dz} + 2\beta I_\lambda^-(z, \mu') = \frac{E}{4\pi} \tag{19}$$

where the absorption coefficient 2β in terms of the real part of the relative permittivity ϵ' and the loss tangent ($\tan\delta$) is

$$2\beta = (2\pi\sqrt{\epsilon'}\tan\delta)/\lambda_0. \tag{20}$$

The volume emissive power E in the Rayleigh–Jeans approximation is

$$E = 4\pi\epsilon' 2\beta C_\lambda T(z) \tag{21}$$

where $T(z)$ is thermal temperature, and C_λ is a parameter dependent only upon λ_0^{-4}. If $T(z)$ is replaced by its first-order approximation, $T(z) = T_g + (\partial T/\partial z)_0 z$, then the complete solution to (19) for upwelling radiation, evaluated at $z = 0$ (just below the interface), is

$$I_\lambda^-(0, \mu') = \epsilon' C_\lambda \left\{ T_g + \frac{\mu'}{2\beta}\left(\frac{\partial T}{\partial z}\right)_0 \right\}. \tag{22}$$

The intensity just above the interface, normalized by C_λ, is the radiobrightness T_b (measured in Kelvin) and is given by $T_b = e(\lambda, \theta) I_\lambda^-(z, \mu')/\epsilon' C_\lambda$ where $e(\lambda, \theta)$ is the directional spectral emissivity and is the source of the emission polarization. The apparent brightness T_a that would be measured by a radiometer located immediately above the interface is the sum of T_b and the reflected sky brightness. From Snell's law, μ' below the interface is relatively near to unity for most satellite incidence angles (typically $\theta \approx 50°$). With only a slight loss of generality, we shall assume that $\mu' \approx 1$ so that polarization can be ignored and brightness temperature can be written

$$T_b = e(\lambda)\{T_g + z_e(\partial T/\partial z)_0\} \tag{23}$$

where $z_e = (2\beta)^{-1}$ has the dimension of length. The parameter z_e might be called the effective emitting depth. It is equivalent to one optical depth in optics, or to half the skin depth in electromagnetics. For moist soils or frozen soils, z_e is typically less than 1 cm (Fig. 9) so that it is reasonable to model the emissivity $e(\lambda)$ as the emissivity of a half-space having the dielectric properties of the soil in the depth interval between the surface and the first isotherm. The Fresnel reflection coefficient for $\mu' \approx 1$ (normal incidence) is

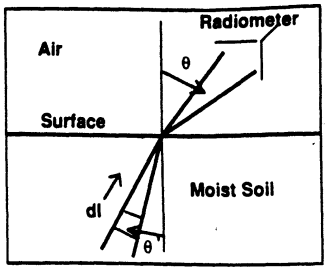

Fig. 4. Schematic of emission from moist soil. Because of transmissivity of soil, thermal microwave emission originates below its optical surface.

$$R = (\sqrt{\epsilon^*} - 1)/(\sqrt{\epsilon^*} + 1) \tag{24}$$

where complex $\epsilon^* = \epsilon'(1 - j\tan\delta)$. The emissivity $e(\lambda)$ is $1 - R\bar{R}$ where $\bar{R}$ is the complex conjugate of R.

The dielectric properties of typical freezing soils at microwave frequencies are given by Hoekstra and Delaney [16]. Fig. 5, from their paper, shows the variability in the complex dielectric constant for several moisture percentages in Groodrich clay and in Fairbanks silt. Note that the dielectric properties are essentially constant through freezing for a moisture content of 5% by weight. This insensitivity to temperature for small moisture contents occurs because the water is chemisorbed, or adsorbed, to the clay or sand interfaces within the soil [17] and bound water molecules are not free to rotate with an electromagnetic field. The dielectric properties of moist soil can be approximated as the sum of the dielectric properties of soil with bound water, plus the dielectric properties of the remaining free water. The dielectric properties of frozen soil are essentially those of soil with only bound water. For the soils in [16], about 7% by weight of the moisture is bound water. If we picture free water as occupying soil intensities (valid for $0.07 < m <$ saturation, where m is the weight fraction of water), then a reasonable approximation to the complex dielectric properties of moist soil is

$$\epsilon^* = \epsilon^*_{\text{soil}} + v_w(f\epsilon^*_{\text{water}} + (1 - f)\epsilon^*_{\text{ice}}) \tag{25}$$

where

- ϵ^*_{soil} complex dielectric constant of 7% moist soil,
- v_w volume fraction of free water or ice,
- $\epsilon^*_{\text{water/ice}}$ complex dielectric constant of water or of ice, respectively,
- f fraction of free water that is in the liquid state.

If ρ_{soil} is the density of 7% moist soil and ρ_{water} is the density of water (≈ 1), then the weight of water in 1 cm^3 is

$$M_w = 0.07\rho_{\text{soil}} + v_w\rho_{\text{water}} \tag{26}$$

and the total weight in 1 cm^3 is

$$M_{\text{tot}} = \rho_{\text{soil}} + v_w\rho_{\text{water}}. \tag{27}$$

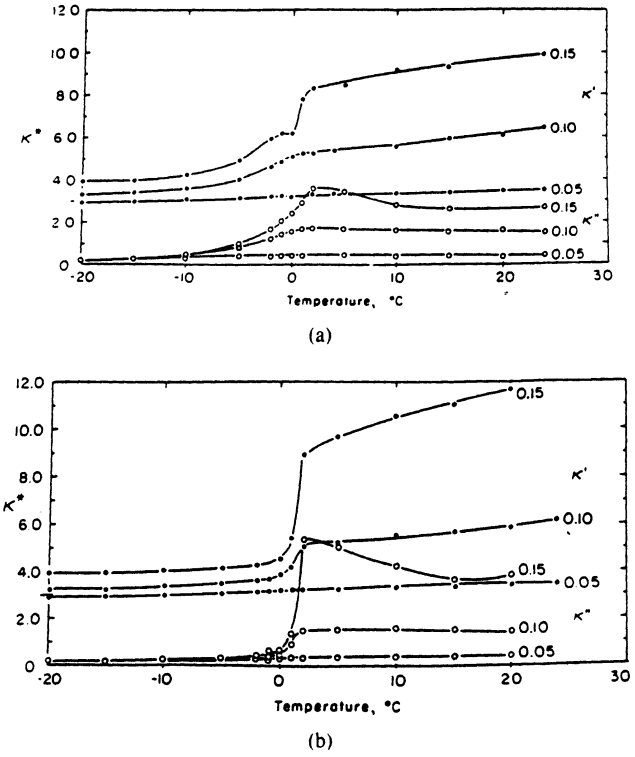

Fig. 5. Complex dielectric constant at 10 GHz as function of temperature at three water contents. (a) Goodrich clay. (b) Fairbanks silt (from Hoekstra and Delaney [16]).

The weight fraction of water m is $m = M_w/M_{tot}$ so that, in terms of m, (25) becomes

$$\epsilon^* = \epsilon^*_{soil} + \frac{(m - 0.07)}{(1 - m)} \rho_{soil} \{ f\epsilon^*_{water} + (1 - f)\epsilon^*_{ice} \} \tag{28}$$

where

$$\epsilon^*_{water} = n^2 + \frac{K_s - K_\infty}{1 + (j\omega\tau_1)^{1-\alpha}} + \frac{K_\infty - n^2}{1 + j\omega\tau_2}$$

([18], [19])

$n^2 = 1.8$,
$K_s = 295.68 - 1.2283T + 2.094 \times 10^{-3}T^2 - 1.41 \times 10^{-6}T^3$,
$K_\infty = 4.2$,
$\alpha = 0.012$,
$\tau_1 = 5.62 \times 10^{-15} e^{3.01 \times 10^{-20}/kT}$ s,
$\tau_2 = 4.2 \times 10^{-14}$ s,
T temperature (K),
$k = 1.3806 \times 10^{-23}$ J/K, Boltzmann's constant,
ω angular frequency (rad/s),

and where

$\epsilon^*_{ice} = K_\infty + [(K_s - K_\infty)/(1 + j\omega\tau)]$,
$K_\infty = 3.2$,
$K_s = 3.2 + 20715/(T - 38)$ [20],
$\tau = 4.76 \times 10^{-16} e^{9.24 \times 10^{-20}/kT}$ [21].

Appropriate model parameters for prairie near Bismarck are listed in Table II. Parametric variables in these models are date and moisture content. While it might be argued that all parameters should be examined parametrically, the extensive computation required is not warranted by any possibility of inverting radiobrightness data to obtain more than moisture content or state.

TABLE II
PARAMETERS FOR BISMARCK, ND

Latitude	47°N
Months	September through December (i.e., 9-12)
Soil moisture	10, 15, 20% by weight
Cloud cover, cl	20%
Average winds, w	5 m/s
Albedo	0.2
Thermal IR emissivity e	0.95
Freeze interval	270-273 K
Dry soil density	1.5E + 3 kg/m^3
Dry soil specific heat	0.84E + 3 J/kg-K
Dry soil thermal conductivity	0.2 W/m-K
7% moist soil dielectric constant	3.3
7% moist soil loss tangent	0.23
Average air temperature, T_0	278.3 K (Fig. 6)
Annual air temperature variation, T_1	16.9 K
Temperature phase lag, θ_{lag}	1.12 months
Diurnal temperature variation, T_{del}	5 K
Water vapor pressure, w	0.76 mmHg

V. Observations

Temperature versus depth profiles at midnight, 6:00 A.M., noon, and 6:00 P.M. for Bismarck, ND, are shown in Fig. 7. The gross features of these profiles are relatively independent of moisture content and month. Among these four profiles, surface temperatures are coldest at 6:00 A.M. (predawn) and hottest at noon, as expected, and thermal pulses at depth are most pronounced at 6:00 P.M. Thermal gradients at the surface are always positive at midnight, 6:00 A.M., and 6:00 P.M., and they are always negative at noon. Note that the effect of freezing and thawing during October through December is a general compression of the temperature profile. That is, the apparent thermal inertia would be greater during freezing and thawing.

Fig. 8 shows diurnal surface temperatures for September through December. The September curves, because temperatures are above freezing, look like the curves for diurnally heated, moist soils [9]-[11]. While moisture tends to reduce the day-night temperature difference, the effect is small. The October curves are very different. The daytime peak is lower because of reduced insolation, but nighttime curves are "held up" by the latent heat of fusion of soil moisture. The effects are similarly pronounced in November and December except that daytime peaks appear suppressed. The cause is the same—daytime radiant heat goes into melting soil ice rather than into raising soil temperature. Again, an observable effect would be a strong increase in the apparent thermal inertia of freezing and thawing soils.

Effective emitting depths z_e, as functions of microwave frequency, moisture content, and time-of-day are shown

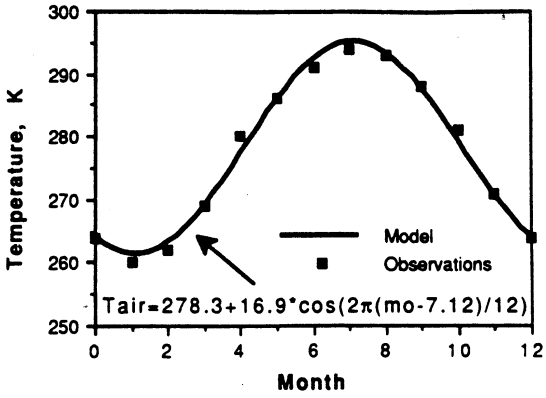

Fig. 6. Monthly average air temperatures for Bismarck, ND (from National Weather Service data). "Model" refers to first-order Fourier component.

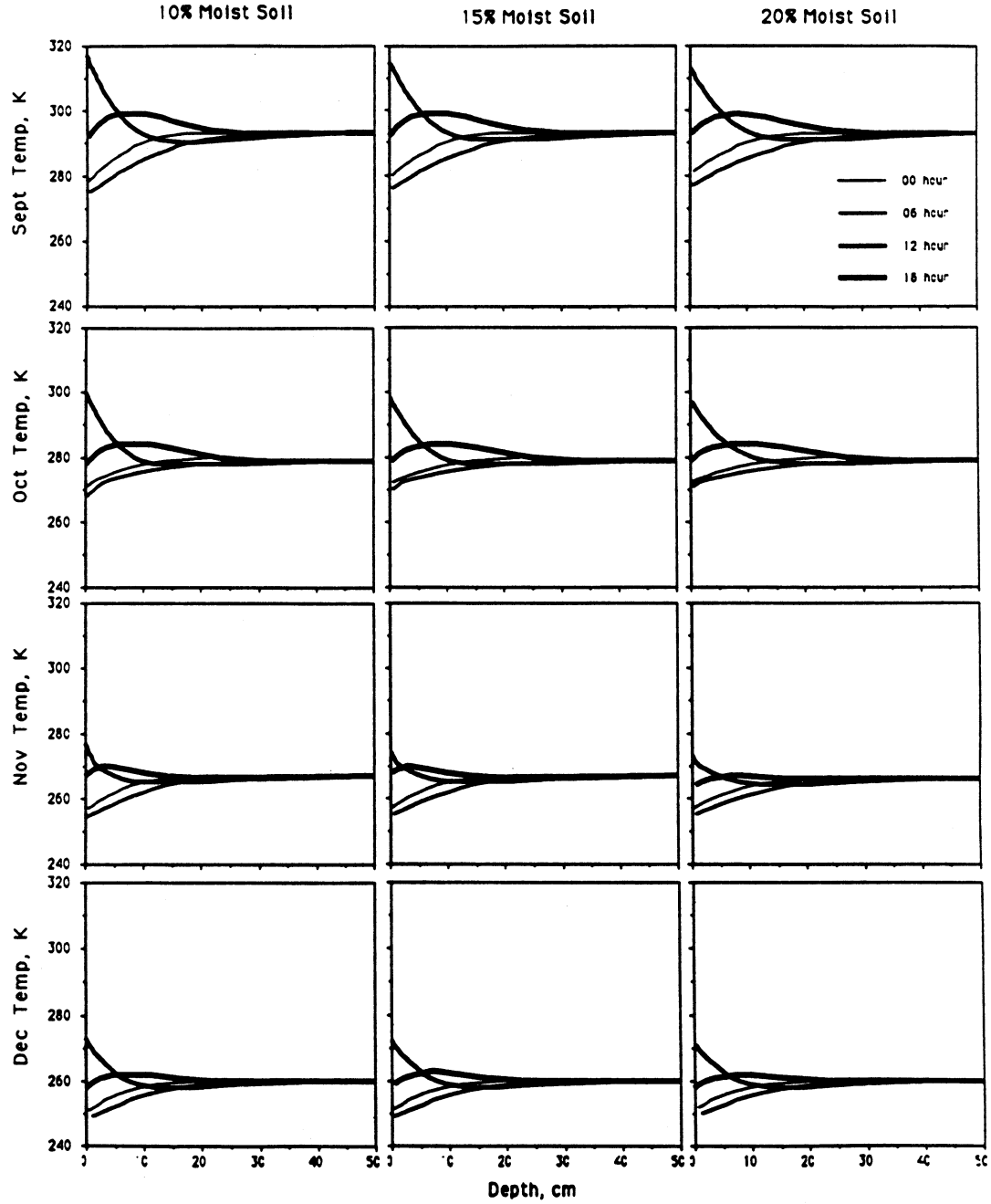

Fig. 7. Temperature versus depth profiles for Bismarck, ND. Curves represent midnight, 6:00 A.M., noon, and 6:00 P.M. for three moisture contents.

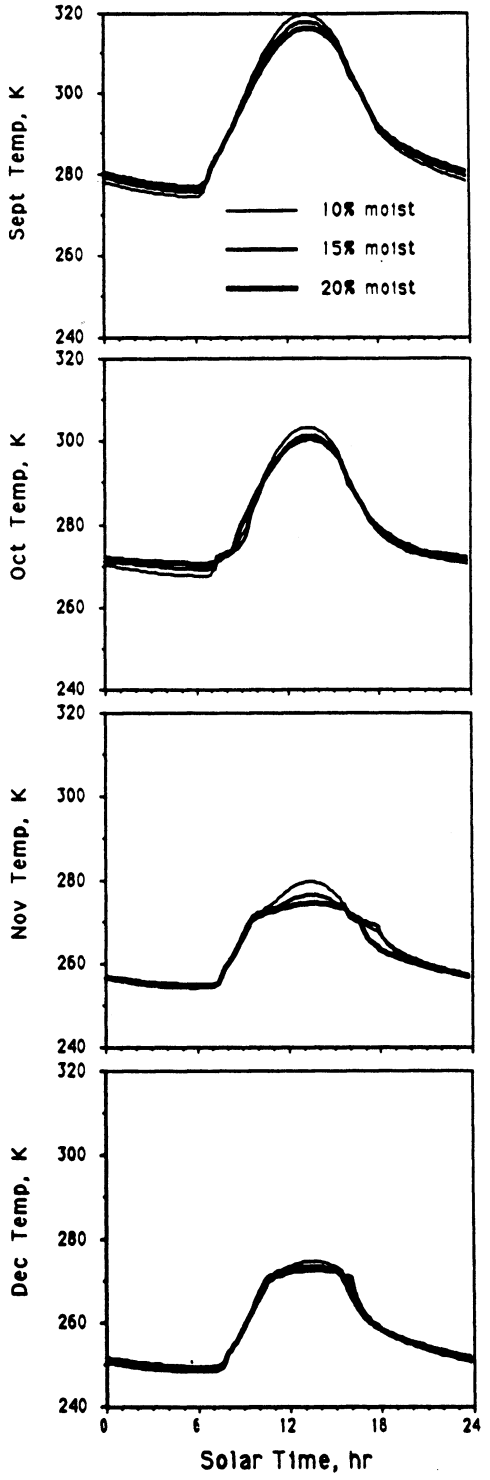

Fig. 8. Diurnal soil surface temperatures at Bismarck, ND. Curves represent moisture contents by weight.

in Fig. 9. The variability with frequency is caused by the Debye relaxation processes in water and ice [16], [17]. The September curves show the effects of moisture: the emitting depth of moist soil decreases with frequency, decreases with moisture content, and increases with insolation (maximum soil surface temperature) for frequencies below the primary relaxation frequency of water. The curves for October are dramatically different because ice in soil is effectively transparent to microwaves. Note that, for these model parameters, October near Bismarck is cold enough to freeze 10% and 15% moist soils completely but not sufficiently cold to freeze 20% moist soil completely. The relatively smooth transitions between frozen and thawed emitting depths result from the assigned 3° freezing range of soil in this model. A reduced freezing range would cause a more abrupt transition.

The curves for November and December are mutually similar. Their major features are that the widths of the

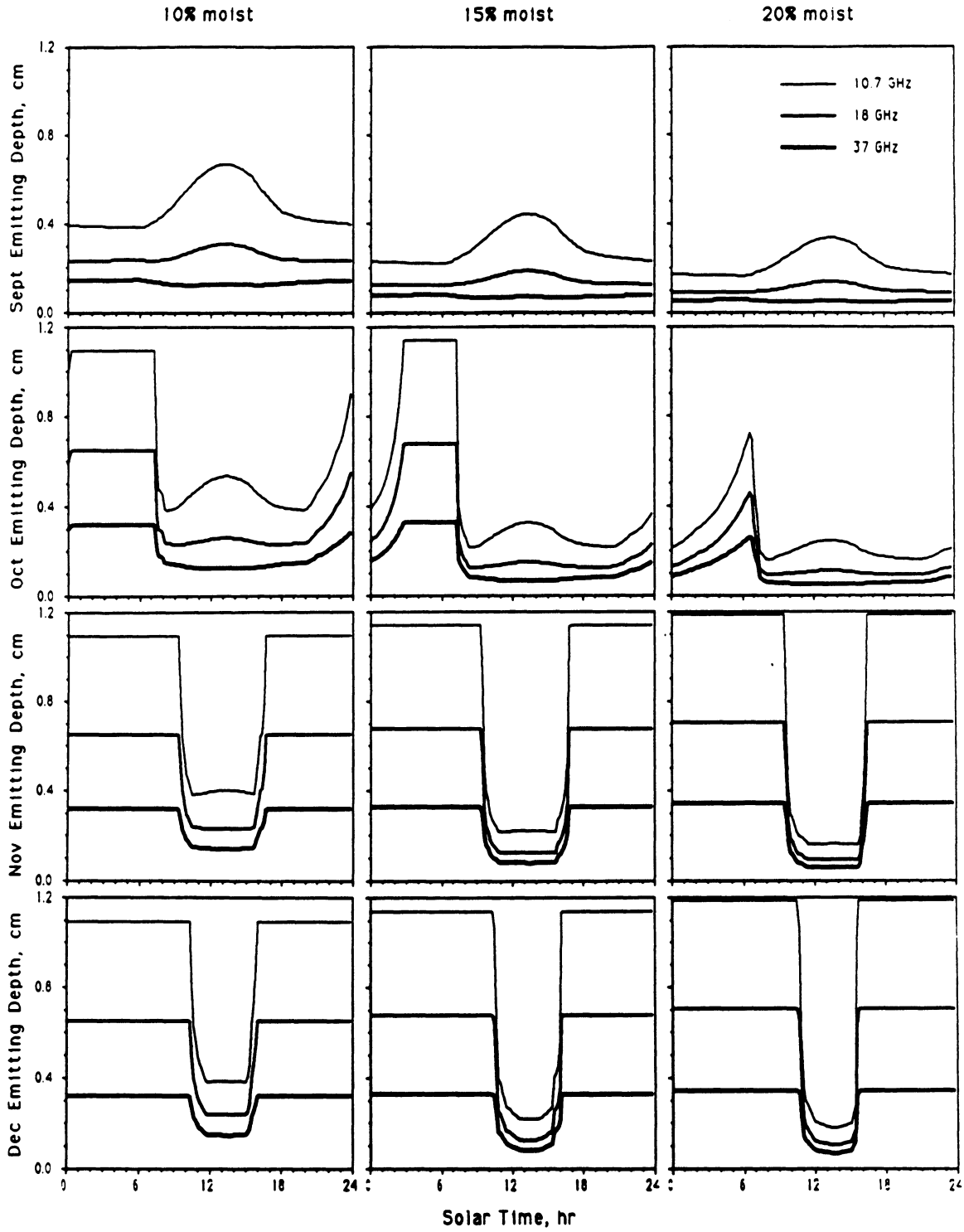

Fig. 9. Effective emitting depth versus time of day. Effective emitting depth is equivalent to optical depth in optics, or to 1/2 skin depth in electromagnetics. Curves represent effective emitting depths for three microwave frequencies—10.7, 18, and 37 GHz.

daytime melt period diminish slightly with increased moisture content because more of the daytime insolation must go into melting ice before temperatures rise. The slight increase in emitting depths with water content for the frozen periods occurs because the effective loss tangent for ice-filled soil is less than that of 7% moist soil. The significant features of these curves are that microwave thermal emission originates much deeper in frozen soils than in moist soils, and that, for the SMMR frequencies, frozen soil emitting depths are roughly 1 cm and less. Therefore, frozen soil thermal gradients that are significant over depths of 1 cm should influence the SMMR spectral gradient.

Radiobrightness curves at the 10.7-, 18-, and 37-GHz SMMR frequencies as functions of moisture content and time of day are shown in Fig. 10. The September (moist soil) brightness decreases with moisture content, and increases with microwave frequency. The frozen soil

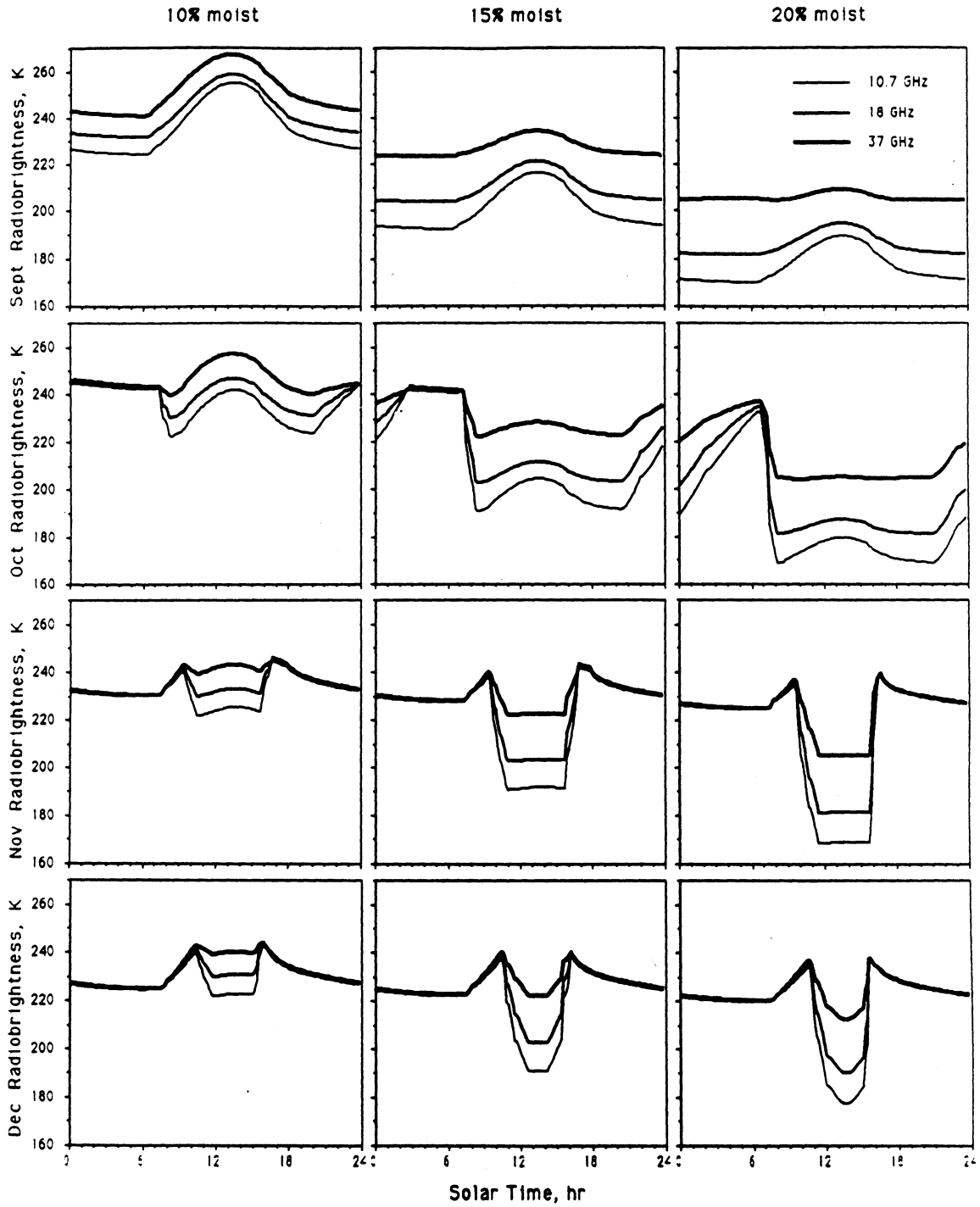

Fig. 10. Radiobrightness versus time of day. Curves represent brightness for three moisture contents and at three microwave frequencies.

brightness curves during October through December are generally high and are relatively independent of microwave frequency. Midnight–noon differences are always positive for moist soils and generally negative for diurnally thawing soils. While none of these soil models remain completely frozen throughout the day, a choice of parameters that avoids midday thawing would exhibit a positive midnight–noon shift in the spectral gradient. Of the three frequencies, the 37-GHz radiobrightness is least affected by moisture content or by freezing and thawing. That is, the 37-GHz radiobrightness most closely follows thermal temperature. It is this property that justifies its use as one of two discriminants in an SMMR frozen soil classifier [7].

Radiobrightness spectral gradients as functions of moisture content and time of day are shown in Fig. 11. The moist soil model gradients are always strongly positive, and the frozen soil model gradients are weakly negative. This unambiguous correlation for low 37-GHz radiobrightnesses is the reason that spectral gradient was

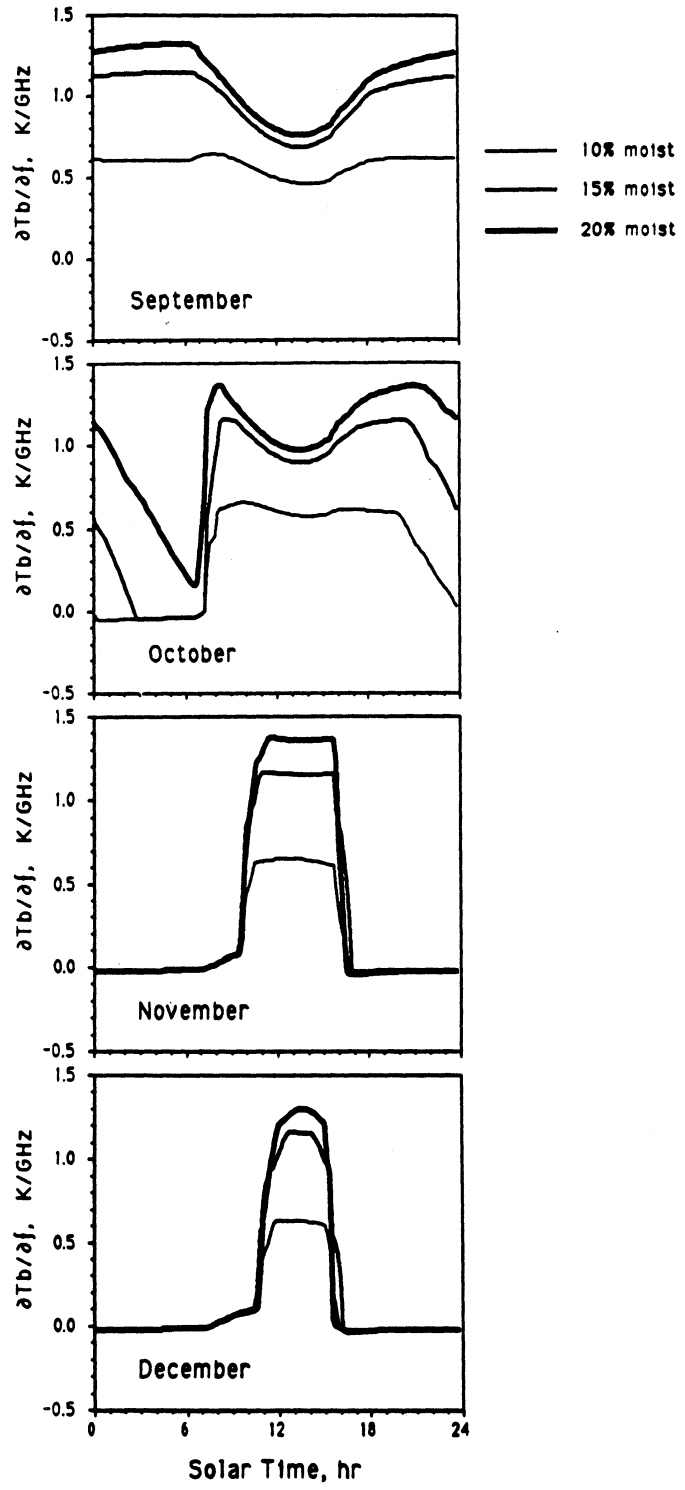

Fig. 11. Radiobrightness spectral gradient versus time of day. Curves represent three moisture contents. Gradients are computed as least squares linear regression of radiobrightness at 10.7, 18, and 37 GHz.

chosen as a second discriminant in the SMMR, frozen soil classifier.

The midnight and noon surface thermal gradients in Fig. 7 are typically +1.5 and −3.5°/cm, respectively. This −5°/cm midnight-noon shift in the thermal gradient corresponds to a +0.1-K/GHz shift in the spectral gradient of frozen soil. This is consistent with the observed +0.1-K/GHz shift in the SMMR data (Fig. 1).

VI. Discrepancies

Model results are highly consistent with the SMMR observations reported by Zuerndorfer *et al.* [7]. However, there are three discrepancies: frozen soil spectral gradients are observed between 0 and −0.3 K/GHz while the model predicts −0.03 K/GHz; the SMMR midnight-noon differences in spectral gradient for thawed soils av-

erage +0.2 K/GHz, while the model predicts that thawed soil differences should be weakly negative; and the SMMR moist soil spectral gradient can be negative on hot (summer) days, while the model predicts positive gradients.

While these discrepancies are ancillary to our objective of examining the performance of the 37-GHz radiobrightness and the 10.7–18–37-GHz spectral gradient as discriminants in a frozen soil classifier, they do suggest that the model is incomplete. Most importantly, it ignores volume scatter darkening by prairie grasses and crop stubble, and by inhomogeneities within the frozen soil. The scattering albedo ω_0 is a measure of the strength of volume scatter darkening. The parameter was developed by Chandrasekhar [22] to describe darkening in planetary atmospheres, and has been applied by England [23], [24] among others to describe darkening in frozen soils, ice, snow, and dry, planetary regoliths. It has become a parameter in most theories of wave propagation and scattering, e.g., Ishimaru [25]. For single scattering,

$$\omega_0 = N\sigma_s/(N\sigma_s + 2\beta) \tag{29}$$

where N is the number of scatterers per unit volume, σ_s is the scattering cross section for a single scatterer, and 2β is the power loss coefficient defined in (20). For spherical scatterers whose diameters are small fractions of a wavelength (Rayleigh scatterers),

$$\sigma_s \alpha \lambda^{-4}. \tag{30}$$

so that ω_0 increases with decreasing wavelength to yield a negative spectral gradient of radiobrightness, i.e., a "law of darkening." This short wavelength darkening is the likely cause of the strongly negative spectral gradient observed in SMMR data for frozen terrain.

The thawed soil, midnight–noon spectral gradient difference, and the hot-day spectral gradient may be influenced by diurnal movement of soil moisture (evapotranspiration?). Such variations in moisture are not included in either the thermal model nor the radiation model. Without more complete experimental data, any explanation of these effects would be little more than speculation.

VII. Conclusion

A modified Chernous'ko method for solving Stefan's problem yields an acceptably rapid convergence to a solution for the thermal structure of diurnally insolated, moist, and frozen soil. The modification involves an alternative piecewise constant enthalpy-temperature approximation that has an odd component of temperature in the vicinity of each isotherm. With this modification, solutions exhibit the expected symmetry for heating and cooling.

Among the 10.7-, 18-, and 37-GHz SMMR frequencies, both the SMMR observations and the models show that the 37-GHz radiobrightness best tracks the thermal temperature of the soil's surface, and that the 10.7–18–37-GHz spectral gradient is always negative for frozen soils. Therefore, the "and" condition, that the 37-GHz radiobrightness be below some threshold and that the spectral gradient be negative, should be an effective classifier of frozen soil.

References

[1] W. J. Burke, T. Schmugge, and J. F. Paris, "Comparison of 2.8- and 21-cm microwave radiometer observations over soils with emission model calculations," *J. Geophys. Res.*, vol. 84, pp. 287–294, 1979.

[2] J. R. Wang, T. J. Schmugge, W. I. Gould, W. S. Glazar, and J. E. Fuchs, "A multifrequency radiometric measurements of soil moisture content over bare and vegetated fields," *Geophys. Res. Let.*, vol. 9, pp. 416–419, 1982.

[3] T. J. Schmugge, "Remote sensing of soil moisture: Recent advances," *IEEE Trans. Geosci. Remote Sensing*, vol. GE-24, pp. 12–22, 1983.

[4] P. J. Camillo and T. J. Schmugge, "Correlating rainfall with remotely sensed microwave radiation using physically based models," *IEEE Trans. Geosci. Remote Sensing*, vol. GE-22, pp. 415–423, 1984.

[5] T. J. Schmugge, P. E. O'Neill, and J. R. Wang, "Passive microwave soil moisture research," *IEEE Trans. Geosci. Remote Sensing*, vol. GE-24, pp. 12–22, 1986.

[6] T. J. Schmugge, "Remote sensing applications in hydrology," *Rev. Geophys.*, vol. 25, pp. 148–152, 1987.

[7] B. W. Zuerndorfer, A. W. England, M. C. Dobson, and F. T. Ulaby, "Mapping freeze/thaw boundaries with SMMR data," *J. Agricultural Forest Meteorol.*, to be published.

[8] H. S. Carslaw and J. C. Jaeger, *Conduction of Heat in Solids*, 2nd ed. New York: Oxford, 1959.

[9] K. Watson, "Geologic application of thermal infrared images," *Proc. IEEE*, pp. 128–137, Jan. 1975.

[10] K. Watson, L. C. Rowan, and T. W. Offield, "Application of thermal modeling in the geologic interpretation of IR images," in *Remote Sensing*, K. Watson and R. Regan, Eds., Geophysics Reprint Series, no. 3. Soc. Exploration Geophysicists, 1983.

[11] A. B. Kahle, "A simple thermal model of the Earth's surface for geologic mapping by remote sensing," *J. Geophys. Res.*, vol. 82, pp. 1673–1680, 1977.

[12] G. W. Evans, "A note on the existence of a solution to a problem of Stefan," *Quart. Appl. Math.*, vol. 9, pp. 185–193, 1951.

[13] H. G. Landau, "Heat conduction in a melting solid," *Quart. Appl. Math.*, vol. 8, pp. 81–94, 1950.

[14] J. Douglas and T. M. Gallie, Jr., "On the numerical integration of a parabolic differential equation subject to a moving boundary condition," *Duke Math. J.*, vol. 22, pp. 557–571, 1955.

[15] F. L. Chernous'ko, "Solution of non-linear heat conduction problems in media with phase changes," *Int. Chem. Eng. J.*, vol. 10, pp. 42–48, 1970.

[16] P. Hoekstra and A. Delaney, "Dielectric properties of soils at UHF and microwave frequencies," *J. Geophys. Res.*, vol. 79, pp. 1699–1708, 1974.

[17] P. Hoekstra and W. T. Doyle, "Dielectric relaxation of surface adsorbed water," *J. Colloid Interface Sci.*, vol. 36, pp. 513–521, 1971.

[18] J. B. Hasted, "Dielectric properties of water and aqueous solutions," in *Dielectric and Related Molecular Processes*. London: Chem. Soc., 1972, pp. 121–162.

[19] J. B. Hasted, *Aqueous Dielectrics*. London: Chapman and Hall, 1973.

[20] R. H. Cole and O. Worz, "Dielectric properties of ice," in *Physics of Ice*, N. Riehl, B. Bullemer, and H. Englehardt, Ed. New York: Plenum, 1969, pp. 456–554.

[21] P. R. Camp, W. Kiszenick, and D. Arnold, "Electrical conduction in ice," in *Physics of Ice*, N. Riehl, B. Bullemer, and H. Englehardt, Eds. New York: Plenum, 1969, pp. 450–470.

[22] S. Chandrasekhar, *Radiative Transfer*. New York: Dover, 1960, p. 6.

[23] A. W. England, "Thermal microwave emission from a scattering halfspace," *Radio Sci.*, vol. 9, pp. 447–454, 1974.

[24] ——, "Thermal microwave emission from a scattering layer," *J. Geophys. Res.*, vol. 80, pp. 4484–4496, 1975.

[25] A. Ishimaru, *Wave Propagation and Scattering in Random Media, I*. New York: Academic, 1978, p. 11.

Anthony W. England (M'87-SM'89) received the B.S. degree in earth sciences, the M.S. degree in geology and geophysics in 1965, and the Ph.D. degree in geophysics in 1970 from the Massachusetts Institute of Technology, Cambridge.

He has undertaken heat flow measurements throughout the Southwest; participated in and led geomagnetic and gravimetric studies in Montana and Antarctica, respectively; participated in radar sounding studies of temperature glaciers in Washington and Alaska, and of polar glaciers in Antarctica; and has investigated theoretically and experimentally the microwave radiometric signatures of snow, ice, and frozen ground and of planetary surfaces and atmospheres. He was Deputy Chief of the Office of Geochemistry and Geophysics of the U.S. Geological Survey. He was a NASA Scientist-Astronaut in 1967, served as Mission Scientist for Apo lo's 13 and 16, and flew as a Mission Specialist on Space Shuttle Cha lenger's Spacelab 2 Mission in 1985—a solar astronomy and plasma phys ics mission. He has been Program Scientist for NASA's Space Station, an an Adjunct Professor at Rice University. He is currently Professor of Elec trical Engineering and Computer Science at the University of Michigan Ann Arbor, where he teaches and conducts research in Earth and planetar microwave remote sensing. He was an Associated Editor for the *Journa of Geophysical Research*. He served on the Earth Science Panel of th NRC's Space Science Board and on several federal committees concerne with Antarctic policy, nuclear waste containment, and federal science an technology.

Dr. England is a member of the American Geophysical Union, and th Administrative Committee of IEEE's Geoscience and Remote Sensing So ciety.

Submitted to IEEE Geosci + Rem Sens.

RADIOBRIGHTNESS DECISION CRITERIA FOR FREEZE/THAW BOUNDARIES

B. Zuerndorfer and A. W. England

Radiation Laboratory

Department of Electrical Engineering and Computer Science

The University of Michigan

Ann Arbor, MI 48109

September 14, 1990

Abstract -- A freeze indicator, based on a low 37 GHz radiobrightness and a low 10.7, 18, and 37 GHz radiobrightness spectral gradient, has been used to classify frozen surfaces in the northern Great Plains. By modeling the radiometer beampatterns as Gaussian, freeze/thaw boundaries can be located at the (fine) resolution of the 37 GHz channel. The performance of the freeze indicator, and subsequent boundary location estimate, depends on the accuracy of the boundary decision criteria. We show that decision criteria based upon clustering and unsupervised classification yield good performance. We also present a simple algorithm for registering coarse-resolution freeze indicator boundaries to equivalent boundaries in fine-resolution 37 GHz radiobrightness images.

1 INTRODUCTION

Soil moisture contributes to the energy exchange between the air and the ground through latent heats of fusion and vaporization. The processes of thawing frozen ground or of evaporating soil moisture cause soil thermal inertias to appear anomalously high. There is a large body of literature about deriving soil moisture from radiobrightness [e.g., 1-7]. In addition, moisture state can also be inferred from radiobrightness. Using data from the Nimbus-7 Scanning Multichannel Microwave Radiometer (SMMR) for a test area that included North Dakota and parts of the surrounding states and southern Canada, Zuerndorfer et. al. [9] showed that a combination of low 37 GHz radiobrightness, $T_B(37)$, and a low spectral gradient of radiobrightness, $\partial T_B(f)/\partial f$ where f is frequency, becomes an effective *freeze indicator*, or discriminant, for classifying frozen terrain. Frozen surfaces appear cold at 37 GHz, and exhibit a negative spectral gradient that we shall argue is largely caused by volume scatter darkening at the shorter wavelengths.

This two parameter freeze indicator (FI) has been applied to SMMR data from the greater North Dakota test area. The spectral gradient is a linear, least-square fit to the 10.7, 18, and 37 GHz radiobrightnesses. A surface is classified as frozen only if both T_B (37) and $\partial T_B(f)/\partial f$ are sufficiently low. A *freeze map* is generated by displaying the FI for each pixel location.

A fundamental problem with the FI algorithm is that radiobrightness measurements from different frequency channels with different spatial resolutions are required to estimate a spectral gradient. To make each radiobrightness value refer to a common area on the ground, data from each channel are compensated to a common spatial resolution so that spatial averaging is identical at all frequencies. Without a priori surface information, the resolution of data at all frequencies are compensated to the (coarse) resolution of the lowest frequency data used in the spectral gradient estimate, and fine-resolution information is lost. Subsequently, all identified freeze/thaw boundaries are localized to the accuracy of the coarse-resolution data. However, by modelling the radiometer

beampatterns as Gaussian, results from scale-space theory [24] can be used to register coarse-resolution freeze/thaw boundaries to fine-resolution 37 GHz boundaries (i.e., to 37 GHz radiobrightness threshold crossings) [10].

A second fundamental problem occurs because diurnal insolation produces temperature gradients within the surface that alter SMMR noon and midnight spectral gradients [11]. In addition, time lags between air and surface temperatures, or poorly compensated heating/cooling of the SMMR instrument by sunlight and Earth shadow [12], may also produce offsets in measurements made at noon and midnight. Decision criteria for classifying surfaces, and identifying freeze/thaw boundaries, must accommodate these day/night differences.

In this paper, we first examine the characteristics of frozen and thawed surfaces in decision space. Frozen and thawed surfaces are classified, and freeze/thaw boundaries located, through clustering and a standard unsupervised classification algorithm. The procedure differs from our previous work in that clustering and classification are unsupervised, and the noon and midnight SMMR measurements are clustered separately. Second, we discuss the appropriateness of Gaussian beamshape modelling, and we demonstrate a simple, automated technique for extrapolating freeze/thaw boundary estimates from the coarse spatial resolution of the freeze map to the fine spatial resolution of the 37 GHz channel.

2 BACKGROUND

2.1 Freeze Indicator

Freezing influences the radiobrightness temperature of the surface, T_B, through parameters in the approximation [11],

$$T_B(f) = e(f)T_0 + \Delta T_B(f) \tag{1}$$

where,

$$\Delta T_B(f) \equiv e(f)\left(\frac{\partial T}{\partial z}\right)_0 z_e(f),$$

$e(f)$ is the emissivity at microwave frequency f, T_0 is the surface temperature, $(\partial T/\partial z)_0$ is the surface thermal gradient, and $z_e(f)$ is the optical thickness of the surface at frequency f. When compared to thawed surfaces, frozen surfaces exhibit signatures of {1} lower thermal temperatures, T_0, {2} higher emissivity, $e(f)$, {3} larger optical thickness, $z_e(f)$, and {4} decreasing radiobrightness, $T_B(f)$.

Signatures {1} and {2} are well understood, but are generally ambiguous indicators of frozen surfaces. Ambiguities arise because changes in radiobrightness that result from freezing the surface may be either positive or negative, depending upon the surface moisture content. For example, a very dry soil emissivity of 0.9 will yield a 9° decrease in radiobrightness for a decrease in soil temperatures from +5° C to -5° C. Because the soil is dry, there is relatively little change in soil emissivity with freezing. In moist soils, freezing causes an increase in soil emissivity because water molecules in frozen plants and soils are not free to align themselves with microwave electric fields. This constraint upon the rotational freedom of water causes a decrease in the real part of the dielectric constant, $\varepsilon'(f)$. A typical soil emissivity would increase from 0.8 to 0.9 with freezing, so that a decrease in soil temperatures from +5° C to -5° C would produce a 19° increase in $T_B(f)$. Because $T_B(f)$ can either increase or decrease with freezing, misclassification will results if $T_B(f)$ at a single frequency were solely used to discrimination between frozen soils and soils that are warmer or drier. These variations in emissivity with freezing are most pronounced at lower microwave frequencies.

Signature {3} arises because freezing reduces the imaginary part of the dielectric constant, $\varepsilon''(f)$, proportionally more than it does the real part, $\varepsilon'(f)$. Reduced $\varepsilon''(f)$ means reduced absorption, so that thermally emitted photons originate deeper within emitting media. Thus, the effective depth of emission,[1] or optical thickness $z_e(f)$, becomes a larger fraction of the free-space wavelength, λ_0

---

1 $(1\text{-}e^{-1})$ of the total emission originates above $z_e(f)$.

[13-16]. The effective emission depth of moist soils is typically 10% of the free-space wavelength. Frozen soils have effective emission depths that may be 30% or more of free-space wavelengths. As a result, the subsurface temperature gradient of frozen soil contributes more to radiobrightness than does an equivalent gradient in thawed soil. The contribution can be several degrees at the lower microwave frequencies.

Table 1 shows the contribution of thermal gradient on radiobrightness, $\Delta T_B(f)$, and on spectral gradient, $\Delta(\partial T_B/\partial f)$, as a function of soil moisture content and time of day (noon vs midnight). The data of Table 1 are derived from a model of typical soil near Bismark, North Dakota for September 22 [11]. The model used an incidence angle of 53.1° and radiometer frequencies of 10.7 GHz, 19.35 GHz, and 37.0 GHz. $\Delta T_B(f)$ is calculated at these frequencies[2], and $\Delta(\partial T_B/\partial f)$ is the least-square regression slope to the three $\Delta T_B(f)$ values. In the model, the soil contains 7% bound water, so that a soil moisture content of 10% has a mixing ratio of 0.03 free water. We see that thermal gradients exert the strongest influence on emissions from frozen, or dry, soil. The thermal gradient produced noon-to-midnight shift in spectral gradient, $\Delta(\partial T_B/\partial f)_{NM}$ is 0.12 K/GHz for frozen soil and, as will be shown, is consistent with SMMR observations.

2 Horizontal and vertical polarizations have been averaged for $\Delta T_B(f)$.

Table 1. Contributions of thermal gradient to radiobrightness and spectral gradients for noon and midnight data. Radiobrightnesses, $\Delta T_B(f)$, are in K and spectral gradients, $\Delta(\partial T_B/\partial f)$, are in K/GHz; $\Delta(\partial T_B/\partial f)_{NM}$ is $\Delta(\partial T_B/\partial f)$ at noon minus $\Delta(\partial T_B/\partial f)$ at midnight.

	$\Delta T_B(f)$, NOON				$\Delta T_B(f)$, MIDNIGHT				
moisture content, %	10.7 GHz	19.35 GHz	37.0 GHz	$\Delta\left(\frac{\partial T_B}{\partial f}\right)$	10.7 GHz	19.35 GHz	37.0 GHz	$\Delta\left(\frac{\partial T_B}{\partial f}\right)$	$\Delta\left(\frac{\partial T_B}{\partial f}\right)_{NM}$
7 (Frozen)	-3.5	-1.8	-1.0	0.091	1.3	0.7	0.4	-0.028	0.12
10	-2.3	-1.0	-0.5	0.061	0.6	0.4	0.3	-0.013	0.07
15	-1.4	-0.6	-0.3	0.039	0.3	0.2	0.1	-0.007	0.05
20	-1.0	-0.4	-0.2	0.029	0.2	0.1	0.1	-0.005	0.03
25	-0.8	-0.3	-0.1	0.023	0.2	0.1	0.1	-0.003	0.03

As a consequence of signatures {1}, {2}, and {3}, the 37 GHz SMMR radiobrightness is more strongly correlated with air temperature than are the 10.7 GHz and 18 GHz SMMR radiobrightnesses. That is, the 37 GHz radiobrightness should serve effectively as one discriminant among frozen and thawed soils.

If soil is modeled as a diurnally heated, homogeneous halfspace, the spectral gradients of radiobrightness are always positive for thawed soils, and are slightly negative (typically -0.1 K/GHz for frozen soils) [11]. However, observed spectral gradients in frozen soils -- signature {4} -- may be more negative than -1.0 K/GHz. The likely cause of such strongly negative gradients is an increased darkening at shorter wavelengths caused by volume scattering within the frozen soil. In the more transparent emitting media, such as frozen soil or dry snow, the greater average thermal photon path length provides a greater opportunity for volume scattering of photons. Scattering is more severe at shorter wavelengths because soils and plants appear increasingly heterogeneous at the scales of these wavelengths [14,17]. Thus, a negative spectral gradient should correlate with frozen soil, and the radiobrightness spectral gradient should serve as a second discriminant among frozen and thawed soils.

2.2 SMMR Data

The data in Figures 1-3 are derived from SMMR radiobrightness measurements made from August 1984 to December 1984 over seven meteorological sites. These sites -- Miles City, MT; Bismarck, Fargo, and Williston, ND; and Aberdeen, Huron, and Rapid City, SD -- are within a test area that includes North Dakota, about half of each neighboring state, and part of Canada. The radiobrightness data are averages of horizontally and vertically polarized SMMR radiobrightness measurements. All data have been compensated to the (coarse) resolution of the 10.7 GHz channel, and are spatially interpolated to the latitude and longitude of each meteorological site using a bi-cubic approximation to a sinc function [34].

Scatter diagrams of $T_B(37)$ as a function of meteorological air temperature (Figures 1a and 1b) show a nominal tracking of air temperature by $T_B(37)$. However, there is an approximate 4° decrease between the noon and the midnight regression lines caused by air temperatures that lag surface temperatures. A simple regression model for $T_B(37)$ would be,

$$T_B(37) = e(37)\,[T_{AIR} + T_{BIAS}(t)] \tag{2}$$

where,

$e(37) \equiv$ 37 GHz Emissivity

$T_{AIR} \equiv$ Air Temperature (K)

$T_{BIAS}(.) \equiv$ Temperature Bias (K)

$t \equiv$ Time,

so that,

$$T_{BIAS}(12) - T_{BIAS}(0) = \frac{4}{e(37)} \approx 4.35K, \tag{3}$$

where t=0 for midnight and t=12 for noon.

Equivalent scatter diagrams of $\partial T_B/\partial f$ as a function of air temperature are shown in Figures 2a and 2b for noon and midnight SMMR data, respectively. The values of $\partial T_B/\partial f$ are the slopes of linear-least-square regressions, as functions of frequency, to SMMR 10.7, 18, and 37 GHz radiobrightnesses at each meteorological site. The data of Figures 2a and 2b show the predicted decrease in spectral gradient with decreasing air temperature (i.e., as surfaces freeze). There are also the anticipated 0.1 K/GHz increase in noon gradients relative to midnight gradients caused by diurnal heating and cooling. In addition, a negative tendency in $\partial T_B/\partial f$ is observed at noon for high air temperatures. This may be caused by volume scattering by dried surface vegetation. Heat and plant senescence in late-summer decrease the moisture in the vegetation canopy. This dry vegetation will act as a scattering layer -- particularly at higher microwave frequencies.

These data (Figures 1 and 2) yield scatter diagrams of $\partial T_B/\partial f$ as a function of $T_B(37)$ (Figures 3a and 3b). In Figures 3a and 3b, data labelled as "frozen" have air temperatures less than 270 K, and "thawed" data have air temperatures greater than 274 K. Data labelled as "mixed" have air temperatures between 270 K and 274 K, inclusive. While air temperature is an imperfect indicator of frozen terrain, we see that low $T_B(37)$ and $\partial T_B/\partial f$ correspond to frozen surfaces.

2.3 Freezing Terrain and Snow Pack

Snow packs produce emission darkening and negative spectral gradients [17], and trace amounts of snow were often observed whenever freezing occurred. It might be argued that our observed negative spectral gradients are caused purely by the snow pack. Figures 4a and 4b show $\partial T_B(f)/\partial f$ as a function of $T_B(37)$ and snow cover for those noon and midnight SMMR data that correspond to air temperatures less than 271 K. The figures show the expected trend towards decreasing $\partial T_B(f)/\partial f$ and decreasing $T_B(37)$ with increasing snow depth. However, there is such variability with snow depth that other phenomena must occur.

The results of McFarland et. al. [26] indicate that snow depths of 2 cm or less show only slight darkening, particularly over dry soil. Some of our data show rather strong darkening at snow depths of under 2.5 cm. Burke et. al. [27] used emissive darkening at 37 GHz to locate snow boundaries on bare soil, but could not determine snow boundaries over regions of frozen ground. These observations suggest that emission darkening of frozen terrain is occurring.

While the snow studies of [26] and [27] were not explicitly concerned with frozen terrain, Wegmüller measured soil temperatures and the radiobrightness of frozen terrain (at 3.1 GHz, 4.5 GHz, 7.2 GHz, and 10.6 GHz) [33]. During his study period, the ground was snow-free and the soil froze to a depth of roughly 5 cm during early-morning hours. The 7.2 and 10.2 GHz penetration depths in frozen soil were calculated as 2.0 cm and 1.2 cm, respectively, so that the early-morning 7.2 GHz and 10.6 GHz radiobrightnesses were produced by frozen terrain. A plot of vertically polarized radiobrightness versus time-of-day [33, Figure 1] shows the 10.6 GHz radiobrightness falling below the 7.2 GHz radiobrightness during the early-morning. Moreover, the temperature differential between the 10.6 and 7.2 GHz radiobrightnesses increased from midnight to dawn (as the ground froze).

Clearly, freezing terrain is a source of emission darkening. However, snow packs, frozen soil , and dry or frozen vegetation are all potential sources of volume scattering. We hope to differentiate amoung these through on-going research.

3 PROCESSING

Clustering determines decision criteria for coarse-resolution classification, and the location of freeze/thaw boundaries. The location of these freeze/thaw boundaries can be refined by imposing spatial constraints.

3.1 Data Clustering

The decision criteria for $T_B(37)$ and $\partial T_B/\partial f$ were based on clustering and unsupervised classification. Unsupervised classification, rather than supervised classification, is used because of the dearth of accurate ground measurements in our test area. Seven air temperature and eleven soil temperature recording sites provided the ground data for the entire test area. Soil temperatures were measured at 5 cm depth and were made at dawn and dusk, whereas SMMR overflights were at noon and midnight.

To increase the number of data available for clustering beyond that used for Figures 1-3, all data from SMMR satellite passes that covered more than 67% of the test area were incorporated in the scatter diagrams of Figures 5-6. Sixteen noon SMMR passes and thirteen midnight passes met this criterion during our August to December test period. As before, the 18 and 37 GHz averages of vertical and horizontal polarized radiobrightness data were resolution compensated to the (coarse) resolution of the 10.7 GHz channel, but unlike the data of Figures 1-3, these compensated data were re-sampled on a 97.5 km grid (i.e., at the resolution of the 10.7 GHz channel). Spectral gradients were computed as the slopes of least-square linear regressions to the 10.7, 18, and 37 GHz radiobrightnesses. Scatter diagrams for the noon and midnight data are shown by month in Figures 5a and 5b, respectively.

Migrating means clustering determined cluster centroids for the data of Figures 5a and 5b [18,19]. On the basis of ground measurements and the data of Figures 1-3, surfaces were classified into three distinct types -- frozen, hot (and dry), and wet (and cool) -- and a fourth type that we call mixed. A frozen surface is characterized by relatively low spectral gradient and a low 37 GHz radiobrightness. Due to the influence of liquid water in the surface, a wet surface is characterized by a high spectral gradient [11] and low 37 GHz radiobrightness [20]. A hot surface has relatively less surface moisture, producing a "dry" surface dielectric constant similar to a frozen surface. Moreover, the relaxation frequency of free-water increases with temperature, further reducing the

spectral gradients of hot surfaces. As a result, a hot surface has a relatively low spectral gradient and a high 37 GHz radiobrightness. A mixed surface has a combination of frozen, wet, and hot characteristics.

Prior to freezing, a surface region is a combination of wet (and cool) and hot (and dry). As freezing begins, the region includes locally frozen surfaces, and would be classified as mixed. A *freeze/thaw criteria* lies within the mixed surface cluster in decision space, and represents maximum $T_B(37)$ and $\partial T_B/\partial f$ values along the freeze/thaw boundary. That is, any surface point on the freeze/thaw boundary has at least one component, $T_B(37)$ or $\partial T_B/\partial f$, equal to that of the freeze/thaw criteria. Equivalently, the FI algorithm [9] requires any surface point classified as frozen to have spectral gradient and 37 GHz radiobrightness less than those of the freeze/thaw criteria.

Cluster centroids determined for the data of Figures 5a and 5b are given in Table 2. Due to SMMR recording problems, limited midnight data were available during December of our test period. Within this limitation, the frozen surface cluster centroid has a lower spectral gradient and 37 GHz radiobrightness at noon than at midnight. Furthermore, because there were few wet surfaces at midnight during the test period, the wet and mixed surface types were inseparable for the midnight data.

Table 2. Cluster centroid in decision space

	NOON DATA		MIDNIGHT DATA	
Surface Type	37 GHz (K)	Gradient (K/GHz)	37 GHz (K)	Gradient (K/GHz)
Frozen	227	-.43	234	-.35
Hot	277	0.11	258	-.01
Wet	238	0.37		
Mixed	250	0.14	243	0.015

Bivariate normal distributions were fit to the cluster data. All data within three standard deviations of a cluster centroid were classified using a Mahanalobis minimum distance classifier (maximum likelihood classification). No preferential weightings of surface types were used.

Constant-deviation, single-class ellipses were drawn in decision space for frozen, hot, and wet surfaces (at noon) and for frozen and hot surfaces (at midnight) using the classified data. The freeze/thaw criteria was determined by allowing the deviation of all ellipses to expand equally until all ellipses intersected. The resulting classification ellipses for noon and midnight SMMR data are shown in Figures 6a and 6b, respectively. The corresponding freeze/thaw criteria in decision space are shown in Table 3.

Table 3. Freeze/thaw criteria in decision space; σ are standard deviations of data within the ellipses.

	37 GHz(K)	Refined 37 GHz(K)	Gradient(K/GHz)	Deviation at Intersection
Noon	252	249	0.0625	3.1 σ
Midnight	247	244	-0.044	2.55 σ

3.2 Refining the Decision Criteria

The $T_B(37)$ boundary pixels have 37 GHz radiobrightnesses that equal the $T_B(37)$ component of the freeze/thaw criteria. If we view the freeze/thaw criteria derived from clustering as initial estimates for determining the freeze/thaw boundary, we suggest the boundary can be refined by requiring a minimum scatter of $T_B(37)$ along that boundary. This constraint ensures boundaries in $T_B(37)$ images correspond closely to FI boundaries.

The $T_B(37)$ component of the freeze/thaw criteria, T_{37}, is adjusted to minimize the sum square error, SSE, in,

$$SSE = \sum_{i=1}^{N} [T_{Bi}(37) - T_{37}]^2, \tag{4}$$

where,

$N \equiv$ number of $T_B(37)$ boundary pixels

$T_{Bi}(37) \equiv$ 37 GHz radiobrightness at the i^{th} boundary pixel.

Equivalently, the refined T_{37} is the average 37 GHz radiobrightness on the boundary. The process is first-order since we do not reiterate SSE minimization with the refined criteria. The refined T_{37} for midnight data from October 24 (Figures 8 and 10) and for noon data from December 11 (Figures 9 and 11), are shown in Table 3.

3.3 Boundary Localization

Spectral gradients are regression slopes to SMMR 37 GHz, 18 GHz, and 10.7 GHz radiobrightness measurements. The nominal resolutions of these channels are 30 km, 60 km, and 97.5 km, respectively. Without compensating for the resolution differences between the channels, the spectral gradient estimates can be in error. For example, a non-zero gradient estimate can result from radiobrightnesses that are spatially variant but are locally constant over frequency. To avoid such errors, the image data were compensated to one common resolution -- the (coarse) resolution of the lowest frequency channel used in gradient estimation -- prior to clustering.

Freeze/thaw boundaries combine 37 GHz threshold crossings and spectral gradient threshold crossings. Corresponding 37 GHz threshold crossings occur in fine-resolution 37 GHz images, but not all 37 GHz threshold crossings represent freeze/thaw boundaries. Some, as previously noted, are boundaries between moist and dry terrain. *Boundary localization* is a three-step process that identifies pixels in fine-resolution, 37 GHz images that correspond to freeze/thaw boundaries at coarse-resolution.

Step 1: Uncompensated 10.7 GHz, 18 GHz, and 37 GHz SMMR data are compensated to the resolution of the 10.7 GHz channel. Gaussian spatial filtering is appropriate for resolution compensation if the Fourier transform of the SMMR beampattern is (approximately) Gaussian

[22]. Antenna data for the Nimbus-7 SMMR antenna are limited, and some investigators have assumed an antenna pattern based upon a uniformly illuminated SMMR aperture [23]. Such an illumination would produce beamwidths that are much narrower than those specified for the SMMR [21]. Alternatively, we assume that the Seasat SMMR beampattern [30] approximates the Nimbus-7 SMMR beampattern, and justify Gaussian filtering by showing that the Fourier transform of the Seasat SMMR beampattern is approximately Gaussian (Figure 7).

The Gaussian filters used to synthesize compensated data at resolution s_2 from uncompensated data at resolution s_1 are,

$$H(f,S) = e^{-\frac{1}{2}(2\pi f)^2 S^2} \tag{5}$$

where the filter width, S, is,

$$S \equiv (s_2^2 - s_1^2)^{1/2}, \quad s_2 > s_1,$$

and f is spatial frequency. Values of S for different configurations of resolution compensation are shown in Table 4.

Table 4. Filter bandwidths for resolution compensation

Nominal Resolution, s_1	Synthesized Resolution, s_2	Filter Bandwidth, S
30 km (Fine)	60 km (Medium)	51.96 km
30 km (Fine)	97.5 km (Coarse)	93.77 km
60 km (Medium)	97.5 km (Coarse)	78.885 km

Step 2: Using resolution compensated data, $T_B(37)$ and $\partial T_B/\partial f$ are calculated for each image pixel at coarse-resolution. Boundaries in coarse-resolution, 37 GHz images are identified where 37 GHz data satisfy the $T_B(37)$ freeze/thaw criteria. Pixels along these 37 GHz image boundaries with $\partial T_B/\partial f$ at or below that of the freeze/thaw criteria are identified as freeze/thaw boundary pixels.

Step 3: Fine-resolution, freeze/thaw boundaries are determined by identifying those pixels in fine-resolution, 37 GHz data that satisfy the $T_B(37)$ freeze/thaw criteria and correspond to coarse-resolution freeze/thaw pixels of step 2. This process involves tracking boundary locations in 37 GHz images as the amount of resolution compensation is reduced. The resulting boundary locations in the fine-resolution 37 GHz images are best estimates of freeze/thaw boundaries in the sense that they are directly traceable to the coarse-resolution boundaries generated by clustering and maximum likelihood classification. The key to this process is that Gaussian image degradation of step 1 uniquely permits recovery of some fine-resolution information, a result derived in scale-space theory [24,25,32].

4 RESULTS

4.1 SMMR Images

Unrefined freeze/thaw criteria (Table 3) were applied to SMMR data for midnight October 24 (Figure 8) and for noon December 11 (Figure 9). Refined freeze/thaw criteria were also applied to the October and December data (Figures 10 and 11, respectively). The dark pixels in the freeze maps[3] (Figures 8a, 9a, 10a, and 11a) correspond to surfaces with low FI value -- surfaces which are most likely frozen -- and freeze/thaw boundaries appear as a fuzzy white lines around these frozen

3 Freeze maps are composite $T_B(37)$ and $\partial T_B/\partial f$ coarse-resolution images, and all boundaries on freeze maps are freeze/thaw boundaries.

regions. The dark pixels in the the 37 GHz images (panels b, d, and f in Figures 8, 9, 10, and 11) correspond to surfaces of low 37 GHz radiobrightness. The fuzzy white lines around these dark regions are the boundary pixels that satify the $T_B(37)$ freeze/thaw criterion. Some or all of these boundaries correspond with the coarse-resolution freeze/thaw boundaries of the freeze maps. Similarly, the dark pixels in the spectral gradient images (Figures 8c, 9c, 10c, and 11c) correspond to surfaces with low spectral gradient, and the fuzzy white lines are boundary pixels that satify the $\partial T_B(f)/\partial f$ freeze/thaw criterion. In all images, regions of no data are shown as white.

Comparing the "unrefined" images of (Figures 8 and 9) with the "refined" images (Figure 10 and 11) shows that refined criteria generate coarse-resolution, 37 GHz boundaries that are located more closely to freeze map and spectral gradient boundaries. Moreover, refined fine-resolution, 37 GHz boundaries (Figures 10f and 11f) are more consistent with ground data than are unrefined 37 GHz boundaries (Figures 8f and 9f). Thus, freeze/thaw boundaries derived from refined criteria should be more accurate that those derived from unrefined criteria.

In the refined images of Figure 10, most sections of the coarse-resolution, 37 GHz boundary in the northwest corner of the test area (Figure 10b) correspond with boundaries of the freeze map (Figure 10a). These sections of 37 GHz boundary would be designated as freeze/thaw boundaries. None of the two other boundaries in Figure 10b correspond to any freeze map boundary, and are probably wet/dry boundaries. The freeze/thaw boundary in the coarse-resolution, 37 GHz radiobrightness image also corresponds to boundaries in medium-resolution and fine-resolution, 37 GHz images. That is, medium-resolution and fine-resolution freeze/thaw boundaries are the convoluted boundaries in the northwest corner of Figures 10d and 10f, respectively. Some boundaries are formed at fine-resolution that do not correspond to any boundary observed at coarse-resolution. These boundaries appear around dark radiobrightness "islands" in Figure 10f, and cannot be identified on the basis of the available information. Such boundaries are not part of the freeze/thaw boundary estimates.

In Figure 11, all coarse-resolution 37 GHz radiobrightness boundaries (Figure 11b) correspond the freeze map boundaries (Figure 11a), and all fine-resolution boundaries (Figure 11f) become freeze/thaw boundary estimates. Midnight and noon fine-resolution freeze/thaw boundaries (Figures 10f and 11f) are consistent with midnight and noon ground data (Figures 10e and 11e).

4.2 Automation

Figures 12 and 13 represent automated boundary localization for the October midnight and December noon SMMR data, respectively. Figures 12a and 13a repeat the freeze maps of Figures 10a and 11a, and Figure 12b and 13b show associated coarse-resolution, 37 GHz radiobrightness images. As before, 37 GHz boundaries are composed of pixels whose 37 GHz radiobrightness equals the $T_B(37)$ component freeze/thaw criteria. However, the 37 GHz boundaries in Figures 12b and 13b consist of (fuzzy) white and black sections. Pixels along white boundaries have spectral gradients that are less than or equal to the $\partial T_B(f)/\partial f$ component of the freeze/thaw criteria. That is, white boundaries are most likely to be freeze/thaw boundaries. Pixels along black boundaries have larger spectral gradients and are less likely to be freeze/thaw boundaries.

In medium-resolution, 37 GHz radiobrightness images (Figures 12c and 13c), white boundaries are 37 GHz boundaries that are migrations of white boundaries at coarse-resolution (Figures 12b and 13b). White boundaries at medium-resolution are (spatially) near white boundaries at coarse-resolution. Precise distances for boundary migration are calculated from ideal 37 GHz radiobrightness measurements and actual freeze/thaw boundary locations (i.e., radiobrightnesses and boundary locations hypothetically measured infinitesimal resolution) [31]. Such ideal data is generally unavailable. However, using the midnight and noon SMMR data, a migration limit of $(s_2 - s_1)/4$ was determined for tracking a boundaries from coarser-to-finer resolution images; s_1 and s_2 are the resolutions of the finer and coarser resolution images, repectively (Table 4). As a result, white boundaries at medium-resolution (Figures 12c and 13c) must be within 9.325 km of white boundaries at coarse-resolution (Figures 12b and 13d); $s_1 = 60$ km and $s_2 = 97.5$ km. Repeating this

process, white boundaries at fine-resolution (Figures 12d and 13d) are 37 GHz boundaries that are within 7.5 km of white boundaries at medium-resolution (Figures 12c and 13c); $s_1 = 30$ km and $s_2 = 60$ km.

Frozen terrain is identified iteratively using fine-resolution, 37 GHz data. First, pixels along white, fine-resolution boundaries (Figures 12d and 13d) are identified as "frozen" pixels. Second, pixels whose 37 GHz radiobrightnesses are less than or equal to the $T_B(37)$ freeze/thaw criterion, and are contiguous to frozen pixels, are also identified as frozen. Third, the previous step is repeated until no additional pixels are identified as frozen. Fourth, the resulting collections of frozen pixels constitute regions of frozen terrain. Using this procedure, terrain identified as frozen are indicated by whitened regions in the northwest corner of the Figure 12e and the all but the southeast corner if Figure 13e. Because freeze/thaw boundaries must be closed contours, the final freeze/thaw boundary (i.e., the edge of the identified frozen region) contains boundary sections that did not, previously, show strong freeze/thaw boundary indications. Nonetheless, the final freeze/thaw boundaries of Figures 12e and 13e are the best fine-resolution estimates of the actual freeze/thaw boundaries using available data.

The images of Figure 14a through Figure 14i are the results of automation applied to data obtained at irregular intervals from October 24, 1984 through December 11, 1984. Time summaries of the data are given in Table 5. These images show the growth and contraction of ground-freeze from October 24 to November 5, and again from November 27 to December 9. After December 9, the area remains frozen through the end of December.

Table 5. Time summary for images of Figure 14a through Figure 14i; measurement interval is the time interval between present and previous measurements.

Figure	Measurement Date	Measurement Time-of-Day	Measurement Interval (Days)
14a	October 24	Midnight	-
14b	October 30	Midnight	6
14c	November 1	Noon	2.5
14d	November 5	Midnight	3.5
14e	November 27	Midnight	22
14f	November 29	Noon	2.5
14g	December 3	Midnight	3.5
14h	December 9	Midnight	6
14i	December 11	Noon	2.5

5 CONCLUSIONS

In Zuerndorfer et. al. [9], a freeze indicator algorithm was developed that used a low 37 GHz radiobrightness and low spectral gradient to classify frozen soil. In this paper, results of the freeze indicator were reviewed using SMMR radiobrightness data collected over the northern Great Plains from August to December, 1984. Effects of snow pack on radiobrightness are similar to that of frozen ground. However, our observations could not be explained by the presence of snow pack alone, and frozen ground was indicated.

Separate clustering of SMMR noon and midnight data yield reasonable discrimination criteria for the classification of frozen ground, and locating freeze/thaw boundaries. These decision criteria are improved by imposing the spatial constraint of consanguinity of the 37 GHz radiobrightness and spectral gradient along the freeze/thaw boundary, at coarse-resolution.

To avoid misclassification, the freeze indicator uses SMMR radiobrightness data at all frequencies are at a common (coarse) resolution. The coarse-resolution data results in the freeze indicator producing poor location estimates of freeze/thaw boundaries. Automated recovery of fine-resolution information is recovered through application of scale-space theory to improve the location estimates of freeze/thaw boundaries.

6 ACKNOWLEDGEMENT

The authors thank Dr. U. Wegmüller for sharing his work and early results. We greatly appreciate his friendly and stimulating correspondences.

REFERENCES

[1] Burke, W.J., T. Schmugge, and J.F. Paris, 1979, Comparison of 2.8- and 21-cm microwave radiometer observations over soils with emission model calculations, *JGR 84*, pp. 287-294.

[2] Wang, J.R., T.J. Schmugge, W.I. Gould, W.S. Glazar, and J.E. Fuchs, 1982, A multi-frequency radiometric measurement of soil moisture content over bare and vegetated fields, *Geophys. Res. Let. 9*, p. 416-419.

[3] Blanchard, B.J., and A.T.C. Chang, 1983, Estimation of soil moisture from Seasat SAR data, *Water Res. Bull. 19*, pp. 803-810.

[4] Schmugge, T.J., 1983, Remote sensing of soil moisture: Recent advances, *IEEE Trans. on Geosc. and Rem. Sens. GE-21*, pp. 336-344.

[5] Camillo, P.J., and T.J. Schmugge, 1984, Correlating rainfall with remotely sensed microwave radiation using physically based models, *IEEE Trans. on Geosc. and Rem. Sens. GE-22*, pp. 415-423.

[6] Schmugge, T.J., P.E. O'Neill, and J.R. Wang, 1986, Passive microwave soil moisture research, *IEEE Trans. on Geosc. and Rem. Sens. GE-24*, pp. 12-22.

[7] Grody, N.C., 1988, Surface identification using satellite microwave radiometers, *IEEE Trans. Geosc. and Rem. Sens.*, V. 26, pp. 850-859.

[8] Schmugge, T.J., 1987, Remote sensing applications in hydrology, *Rev. Geophys. 25*, pp. 148-152.

[9] Zuerndorfer, B.W., England, A.W., Dobson, C.M., and Ulaby, F.T., 1989, Mapping freeze/thaw boundaries with SMMR data, *J. Agriculture and Forest Meteorology*, in press.

[10] Zuerndorfer, B.W., England, A.W., and Wakefield, G.H., 1989, The radiobrightness of freezing terrain, *1989 IEEE Int. Geosci. and Remote Sensing Symp.*, Vancouver, Canada.

[11] England, A.W., 1990, Radiobrightness of diurnally heated, freezing soil, *IEEE Trans. Geosc. and Rem. Sens.*, GE-28, No. 4, pp. 464-476.

[12] Millman, A., 1988, Personnal communication, June 27, 1988.

[13] England, A.W., 1974, The effect upon microwave emissivity of volume scattering in snow, in ice, and in frozen soil, *Proc. URSI Spec Mtg on Microwave Scattering and Emission from the Earth*, Berne, Switzerland, 23-26 Sept., 1974.

[14] England, A.W., 1975, Thermal microwave emission from a scattering layer, *JGR 80*, pp. 4484-4496.

[15] England, A.W., 1976, Relative influence upon microwave emissivity of fine-scale stratigraphy, internal scattering, and dielectric properties, *Pageoph 114*, pp. 287-299.

[16] England, A.W., 1977, Microwave brightness spectra of layered media, *Geophysics 42*, pp. 514-521.

[17] Edgerton, A.T., A. Stogryn, and G. Poe, 1971, Microwave Radiometric Investigations of Snowpacks, Final Rept. 1285R-4 of Contract 14-08-001-11828 between Aerojet-General Corp., El Monte, CA, and the U.S. Geological Survey.

[18] Richards. J.A., 1986, *Remote Sensing Digital Image Analysis* , Springer-Verlag, Berlin.

[19] Clustering and classification was performed on a Sun-4 workstation using EASI software, version 4.1, from PCI, Inc. of Richmond Hill, Ontario (Canada).

[20] Hoehstra, P. and Delaney, A., 1974, Dielectric properties of soils at UHF and microwave frequencies, *J. Geophys. Res. 79*, pp. 1699-1708.

[21] NASA, 1978, The Scanning Multichannel Microwave Radiometer (SMMR) experiment, *The Nimbus-7 Users Guide*, The Landsat/Nimbus Project, Goddard Space Flight Center, NASA, p. 213-245.

[22] Bracewell, R. N., 1986, *The Fourier Transform and Its Applications*, McGaw-Hill.

[23] Chin, R.T., Yeh, C., and Olson, W.S., 1985, Restoration of multichannel microwave radiometric images, *IEEE Trans. Patt. Anal. Mach. Intell.*, PAMI-7, pp. 475-484.

[24] Witkin, A., 1983, Scale-space filtering, *Proc. Int. Joint. Conf. Artif. Intell.*, Karlsruhe, West Germany, p. 1019-1021.

[25] Yuille, A., and T. Poggio, 1986, Scaling theorems for zero crossings, *IEEE Trans. Patt. Anal. Mach. Intell.*, Vol. PAMI-8, No. 1, p. 15-25.

[26] McFarland, M.J., G.D. Wilke, and P.H. Harder, 1987, Nimbus 7 Investigation of snowpack properties in the northern great plains for the winter of 1978-1979, *IEEE Trans. on Geosc. and Rem. Sens. GE-25*, pp. 35-46.

[27] Burke, H.-H.K., C.J. Bowley, and J.C. Barnes, 1984, Determination of snowpack properties from satellite passive microwave measurements, *Remote Sensing Environ.*, Vol. 15, pp. 1-20.

[28] Kunzi, K.F., P. Subash, and H. Rott, 1982, Snow-cover parameters from Nimbus 7 Scanning Multichannel Microwave Radiometer (SMMR) data, *IEEE Trans. on Geosc. and Rem. Sens. GE-20*, pp. 452-467.

[29] Barton, D.K. and H.R. Ward, 1969, *Handbook of Radar Measurments*, Prentice-Hall, Inc., Englewood Cliffs, NJ.

[30] Njoku, E.G., J.M. Stacey, and F.T. Barath, 1980, The Seasat Scanning Multichannel Microwave Radiometer (SMMR): Instrument desription and performance, *IEEE Trans. Ocean Engin. OE-5*, pp. 100-115.

[31] Zuerndorfer, B. and G. H. Wakefield, 1990, Applications of scale-space filtering to signature analysis, *IEEE Trans. Acoust. Speech Signal Process.*, under review.

[32] Zuerndorfer, B. and G. H. Wakefield, 1990, Extensions of scale-space filtering to machine-sensing systems, *IEEE Trans. Patt. Anal. Mach. Intell.*, in press.

[33] Wegmüller, U., 1990, The effect of a frozen soil layer on the microwave signatures of bare soil, *Remote Sensing Environ.*, in press.

[34] Moik, J., 1980, *Digital Processing of Remotely Sensed Images*, NASA, NASA SP-431.

FIGURE CAPTIONS

Figure 1. $T_B(37)$ versus measured air temperature at meteorological sites in North Dakota and the surrounding region. Data were collected from 8/1/84 to 12/31/84.

(a) Noon data

(b) Midnight data

Figure 2. $\partial T_B/\partial f$ versus measured air temperature at meteorological sites in North Dakota and the surrounding region. Data were collected from 8/1/84 to 12/31/84.

(a) Noon data

(b) Midnight data

Figure 3. $\partial T_B/\partial f$ versus $T_B(37)$ at meteorological sites in North Dakota and the surrounding region. Data were collected from 8/1/84 to 12/31/84.

(a) Noon data

(b) Midnight data

Figure 4. $\partial T_B/\partial f$ versus $T_B(37)$ at meteorological sites in North Dakota and the surrounding region, for measured air temperature less than 271 K. Data were collected from 8/1/84 to 12/31/84 and sorted by snow depth.

(a) Noon data

(b) Midnight data

Figure 5. Scatter diagram of $\partial T_B/\partial f$ versus $T_B(37)$ throughout North Dakota and the surrounding region. Data were collected from 8/1/84 to 12/31/84.

(a) Noon data

(b) Midnight data

Figure 6. Single class ellipses of $\partial T_B/\partial f$ versus $T_B(37)$ throughout North Dakota and the surrounding region. Data were collected from 8/1/84 to 12/31/84.

(a) Noon data

(b) Midnight data

Figure 7. Spatial frequency response of Seasat SMMR beampattern versus Gaussian model.

Figure 8. A comparison of reported air and soil temperatures with images of North Dakota and the surrounding region. Boundaries were determined using unrefined freeze/thaw criteria. Data were collected at midnight, October 24, 1984.

(a) Freeze map at coarse-resolution

(b) 37 GHz radiobrightness at coarse-resolution

(c) Spectral gradient at coorse-resolution

(d) 37 GHz radiobrightness at medium-resolution

(e) Air and soil temperatures

(f) 37 GHz radiobrightness at fine-resolution

Figure 9. A comparison of reported air and soil temperatures with images of North Dakota and the surrounding region. Boundaries were determined using unrefined freeze/thaw criteria. Data were collected at noon, December 11, 1984.

(a) Freeze map at coarse-resolution

(b) 37 GHz radiobrightness at coarse-resolution

(c) Spectral gradient at coarse-resolution

(d) 37 GHz radiobrightness at medium-resolution

(e) Air and soil temperatures

(f) 37 GHz radiobrightness at fine-resolution

Figure 10. A comparison of reported air and soil temperatures with images of North Dakota and the surrounding region. Boundaries were determined using refined freeze/thaw criteria. Data were collected at midnight, October 24, 1984.

(a) Freeze map at coarse-resolution

(b) 37 GHz radiobrightness at coarse-resolution

(c) Spectral gradient at coorse-resolution

(d) 37 GHz radiobrightness at medium-resolution

(e) Air and soil temperatures

(f) 37 GHz radiobrightness at fine-resolution

Figure 11. A comparison of reported air and soil temperatures with images of North Dakota and the surrounding region. Boundaries were determined using refined freeze/thaw criteria. Data were collected at noon, December 11, 1984.

(a) Freeze map at coarse-resolution

(b) 37 GHz radiobrightness at coarse-resolution

(c) Spectral gradient at coarse-resolution

(d) 37 GHz radiobrightness at medium-resolution

(e) Air and soil temperatures

(f) 37 GHz radiobrightness at fine-resolution

Figure 12. Automated images of North Dakota and the surrounding region. Boundaries were determined using refined freeze/thaw criteria. Data were collected at midnight, October 24, 1984.

(a) Freeze map at coarse-resolution

(b) 37 GHz radiobrightness at coarse-resolution

(c) 37 GHz radiobrightness at medium-resolution

(d) 37 GHz radiobrightness at fine-resolution

(e) Classified frozen ground at fine-resolution

Figure 13. Automated images of North Dakota and the surrounding region. Boundaries were determined using refined freeze/thaw criteria. Data were collected at noon, December 11, 1984.

(a) Freeze map at coarse-resolution

(b) 37 GHz radiobrightness at coarse-resolution

(c) 37 GHz radiobrightness at medium-resolution

(d) 37 GHz radiobrightness at fine-resolution

(e) Classified frozen ground at fine-resolution

Figure 14. Automated images of classified frozen ground of North Dakota and the surrounding region. Data were collected at irregular intervals from 10/24/84 to 12/11/84.

(a) Midnight, 10/24/84

(b) Midnight, 10/30/84

(c) Noon, 11/1/84

(d) Midnight, 11/5/84

(e) Midnight, 11/27/84

(f) Noon, 11/29/84

(g) Midnight, 12/3/84

(h) Midnight, 12/9/84

(i) Midnight, 12/11/84

FIGURES

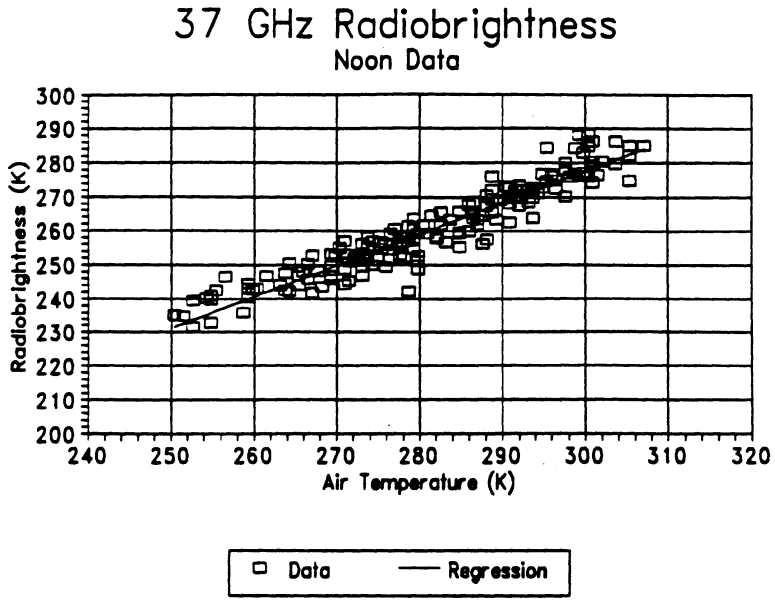

Fig. 1a

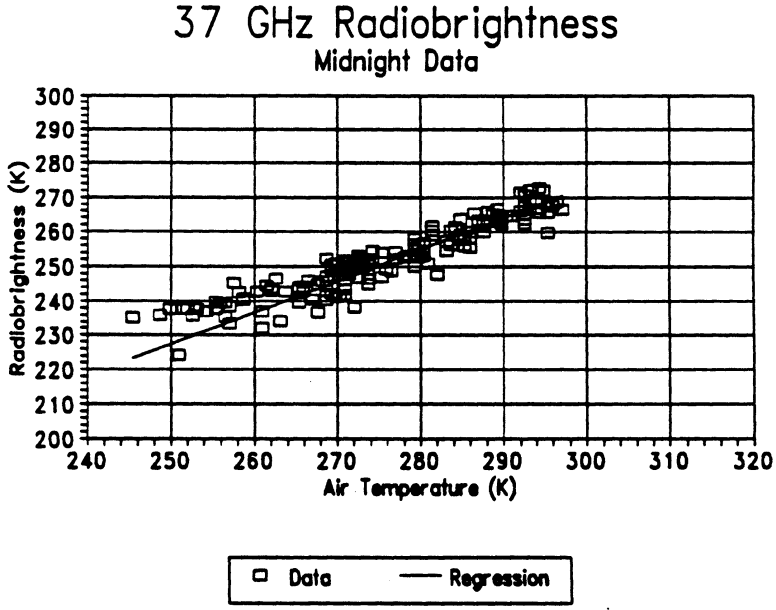

Fig. 1b

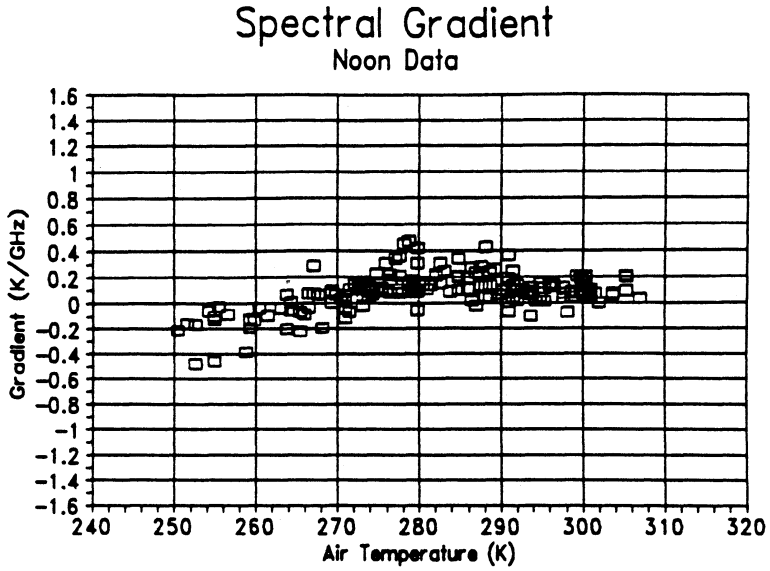
Spectral Gradient
Noon Data
Gradient (K/GHz)
1.6
1.4
1.2
1
0.8
0.6
0.4
0.2
0
-0.2
-0.4
-0.6
-0.8
-1
-1.2
-1.4
-1.6
240 250 260 270 280 290 300 310 320
Air Temperature (K)

Fig. 2a

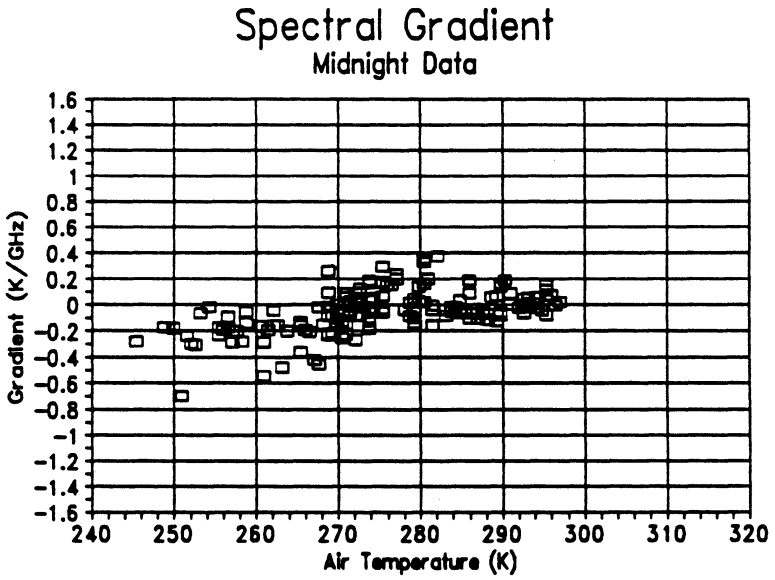
Spectral Gradient
Midnight Data
Gradient (K/GHz)
1.6
1.4
1.2
1
0.8
0.6
0.4
0.2
0
-0.2
-0.4
-0.6
-0.8
-1
-1.2
-1.4
-1.6
240 250 260 270 280 290 300 310 320
Air Temperature (K)

Fig. 2b

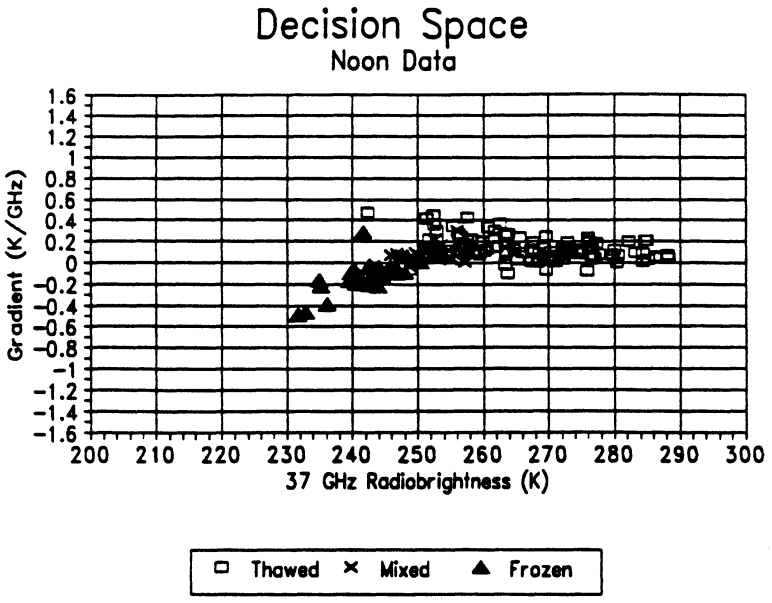
Decision Space
Noon Data
Gradient (K/GHz)
1.6
1.4
1.2
1
0.8
0.6
0.4
0.2
0
-0.2
-0.4
-0.6
-0.8
-1
-1.2
-1.4
-1.6
200 210 220 230 240 250 260 270 280 290 300
37 GHz Radiobrightness (K)
Thawed
Mixed
Frozen

Fig. 3a

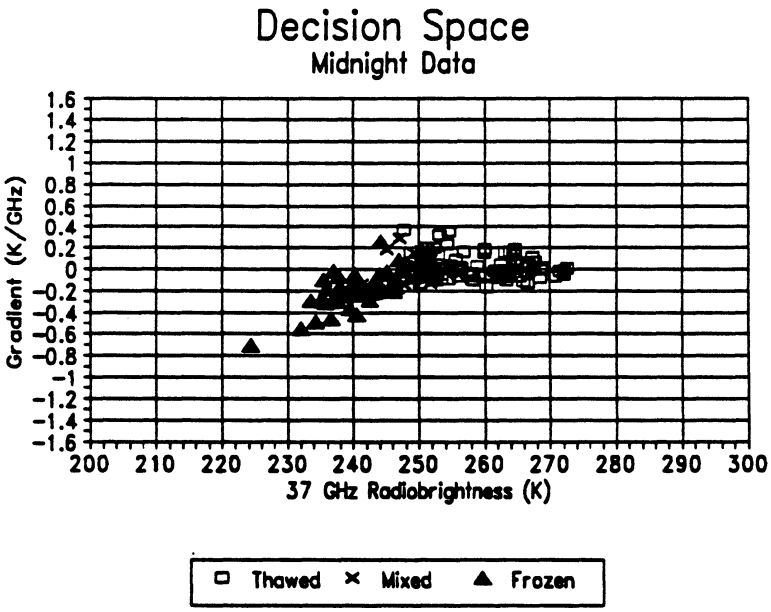
Decision Space
Midnight Data
Gradient (K/GHz)
1.6
1.4
1.2
1
0.8
0.6
0.4
0.2
0
-0.2
-0.4
-0.6
-0.8
-1
-1.2
-1.4
-1.6
200 210 220 230 240 250 260 270 280 290 300
37 GHz Radiobrightness (K)
Thawed
Mixed
Frozen

Fig. 3b

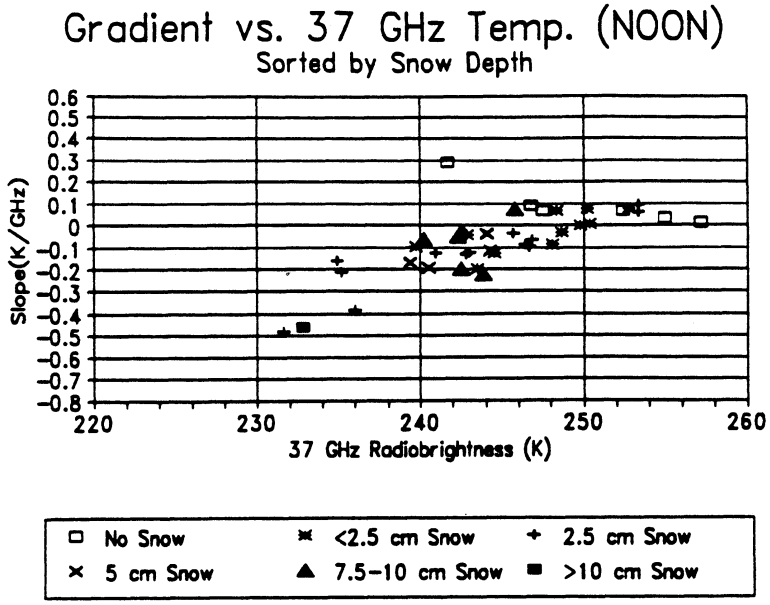
Gradient vs. 37 GHz Temp. (NOON)
Sorted by Snow Depth
Slope(K/GHz)
0.6
0.5
0.4
0.3
0.2
0.1
0
-0.1
-0.2
-0.3
-0.4
-0.5
-0.6
-0.7
-0.8
220
230
240
250
260
37 GHz Radiobrightness (K)
No Snow
<2.5 cm Snow
2.5 cm Snow
5 cm Snow
7.5-10 cm Snow
>10 cm Snow

Fig. 4a

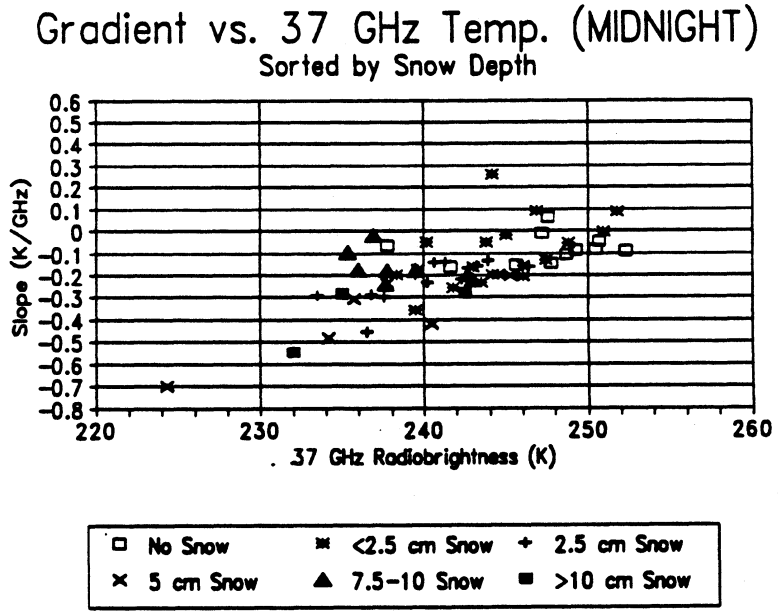
Gradient vs. 37 GHz Temp. (MIDNIGHT)
Sorted by Snow Depth
Slope (K/GHz)
0.6
0.5
0.4
0.3
0.2
0.1
0
-0.1
-0.2
-0.3
-0.4
-0.5
-0.6
-0.7
-0.8
220
230
240
250
260
37 GHz Radiobrightness (K)
No Snow
<2.5 cm Snow
2.5 cm Snow
5 cm Snow
7.5-10 Snow
>10 cm Snow

Fig. 4b

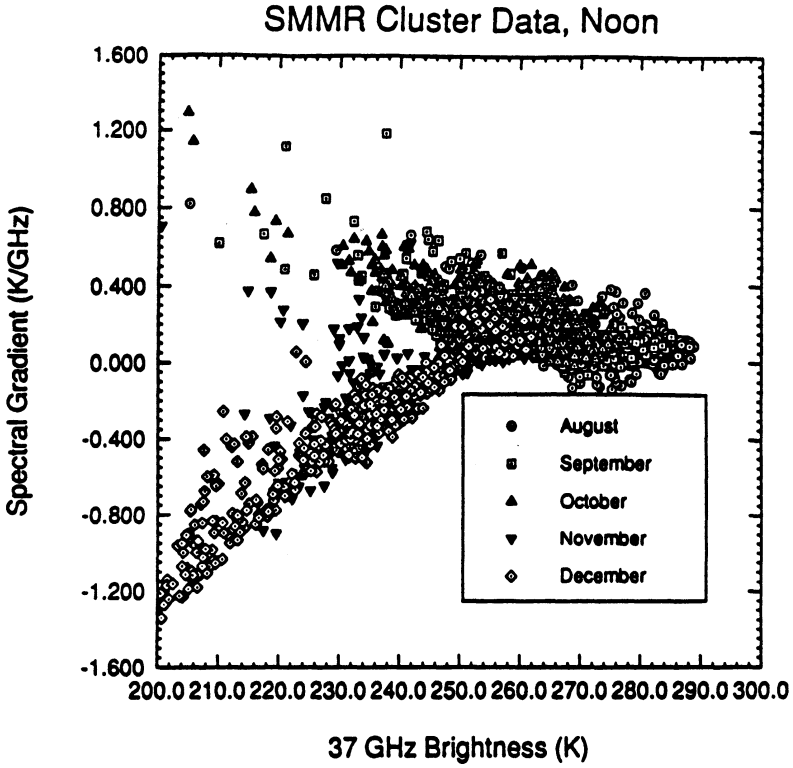
SMMR Cluster Data, Noon
Spectral Gradient (K/GHz)
1.600
1.200
0.800
0.400
0.000
-0.400
-0.800
-1.200
-1.600
200.0 210.0 220.0 230.0 240.0 250.0 260.0 270.0 280.0 290.0 300.0
37 GHz Brightness (K)
August
September
October
November
December

Fig. 5a

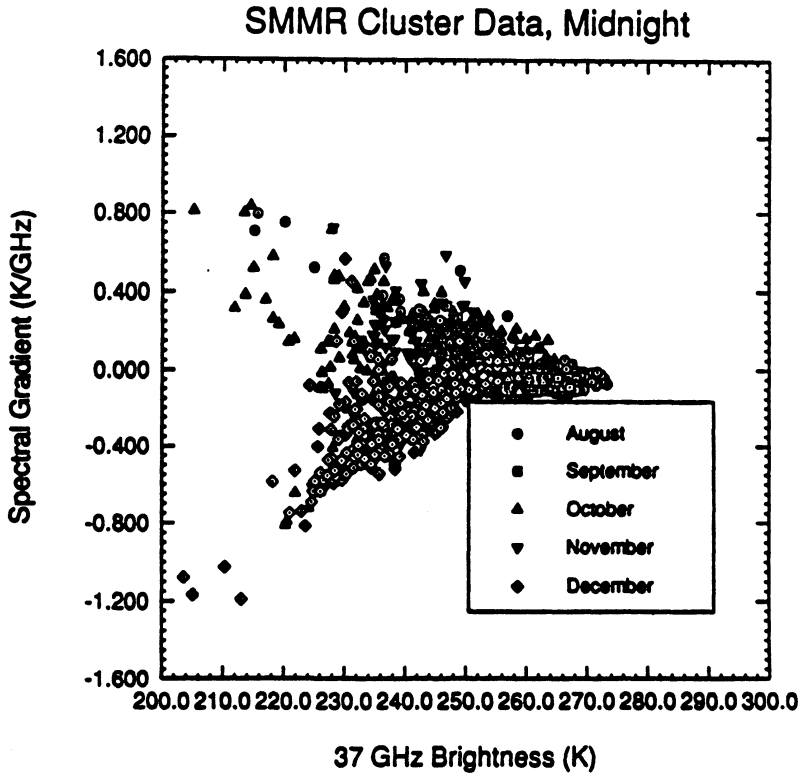
SMMR Cluster Data, Midnight
Spectral Gradient (K/GHz)
1.600
1.200
0.800
0.400
0.000
-0.400
-0.800
-1.200
-1.600
200.0 210.0 220.0 230.0 240.0 250.0 260.0 270.0 280.0 290.0 300.0
37 GHz Brightness (K)
August
September
October
November
December

Fig. 5b

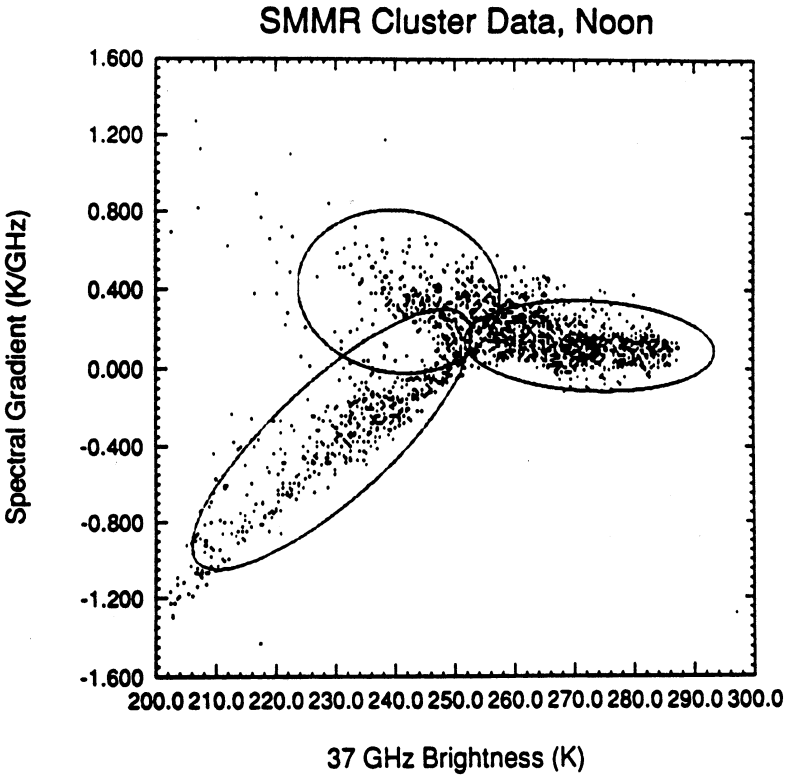
SMMR Cluster Data, Noon
Spectral Gradient (K/GHz)
1.600
1.200
0.800
0.400
0.000
-0.400
-0.800
-1.200
-1.600
200.0 210.0 220.0 230.0 240.0 250.0 260.0 270.0 280.0 290.0 300.0
37 GHz Brightness (K)

Fig. 6a

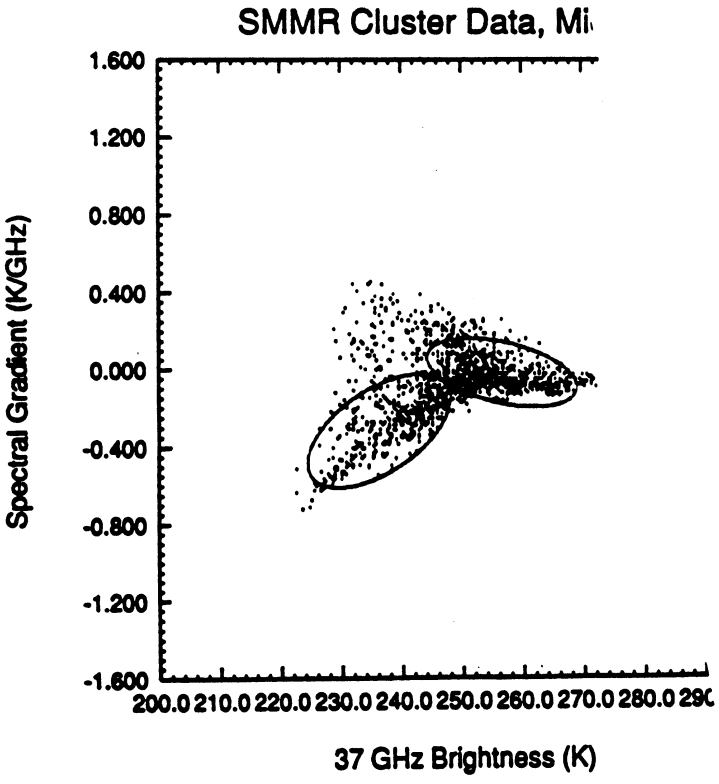
SMMR Cluster Data, Mi
Spectral Gradient (K/GHz)
1.600
1.200
0.800
0.400
0.000
-0.400
-0.800
-1.200
-1.600
200.0 210.0 220.0 230.0 240.0 250.0 260.0 270.0 280.0 29(
37 GHz Brightness (K)

Fig. 6b

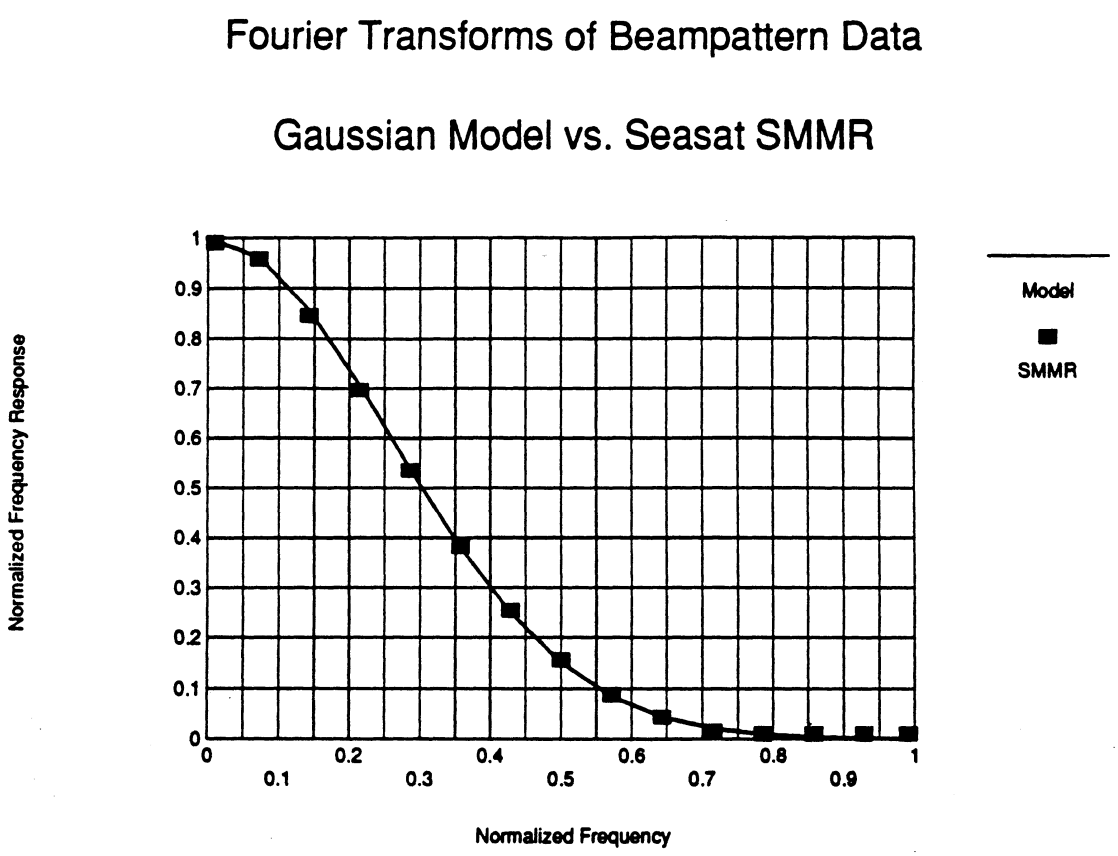
Fourier Transforms of Beampattern Data
Gaussian Model vs. Seasat SMMR
Normalized Frequency Response
1
0.9
0.8
0.7
0.6
0.5
0.4
0.3
0.2
0.1
0
0
0.1
0.2
0.3
0.4
0.5
0.6
0.7
0.8
0.9
1
Normalized Frequency
Model
SMMR

Fig. 7

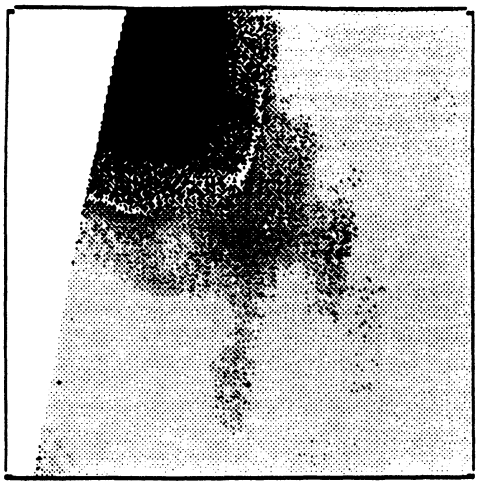

Fig. 8a

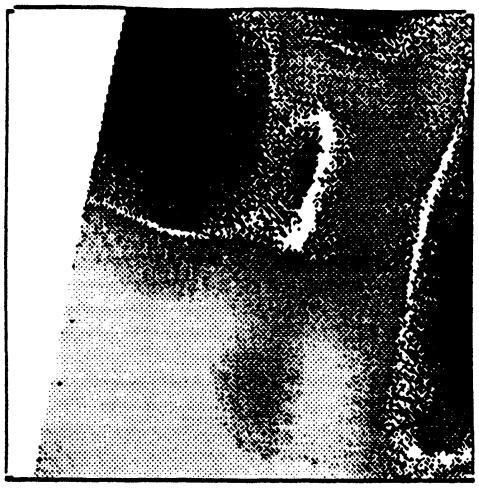

Fig. 8b

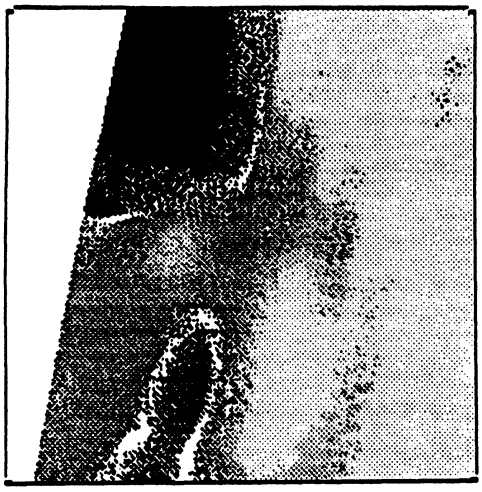

Fig. 8c

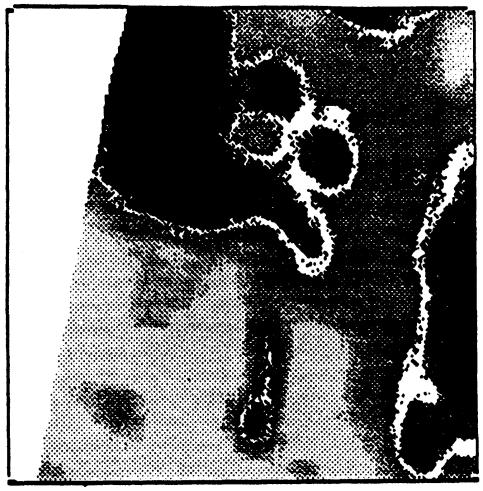

Fig. 8d

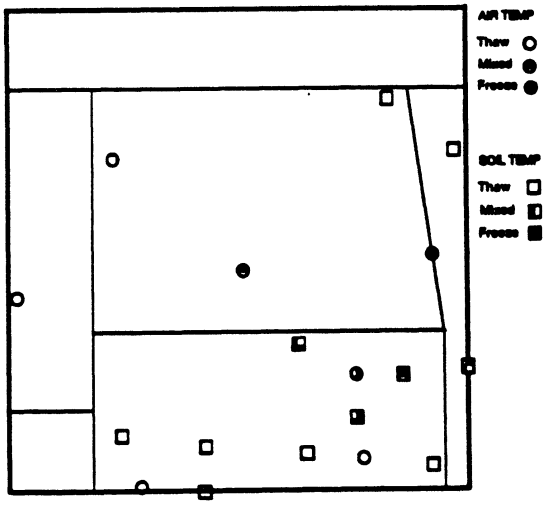

Fig. 8e

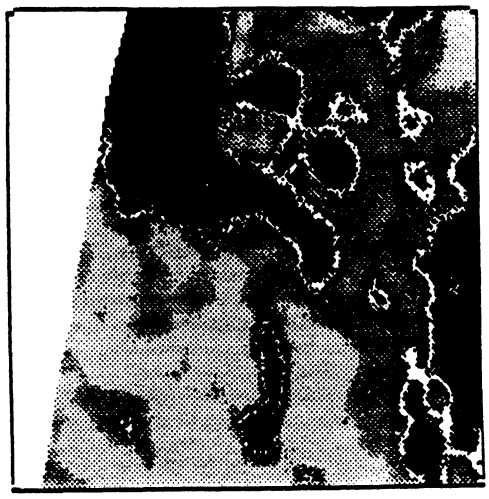

Fig. 8f

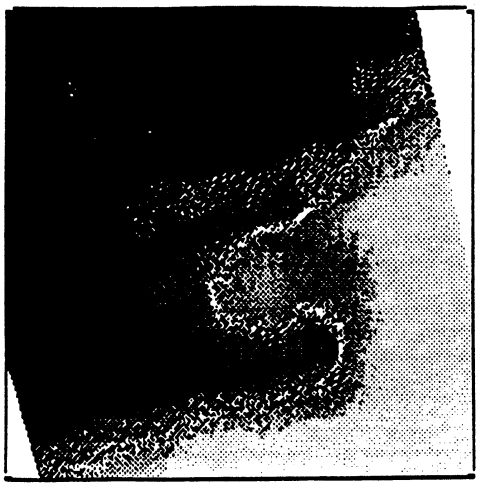

Fig. 9a

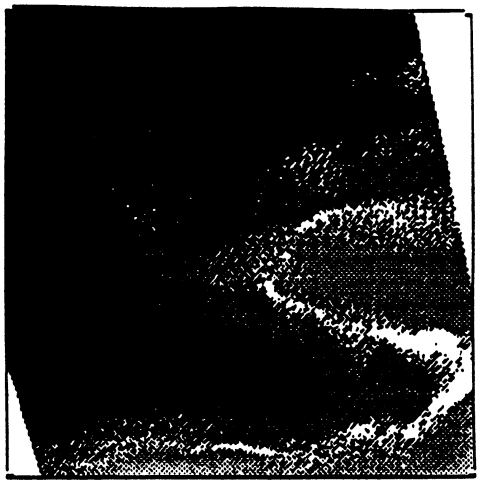

Fig. 9b

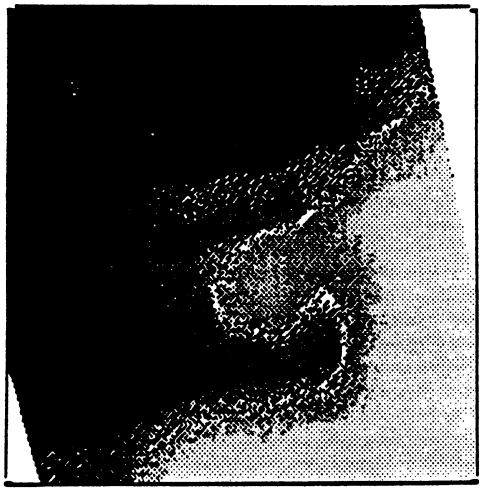

Fig. 9c

Fig. 9d

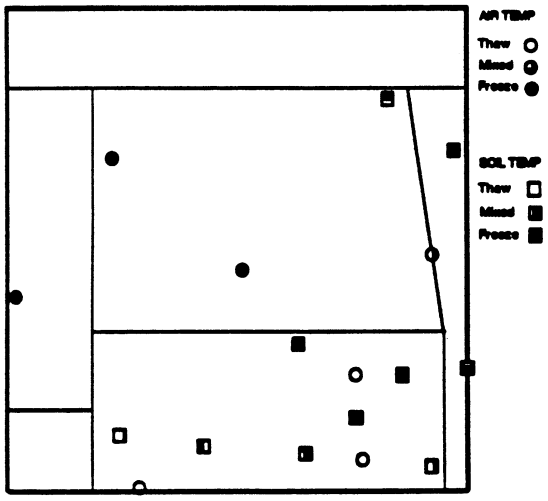

Fig. 9e

Fig. 9f

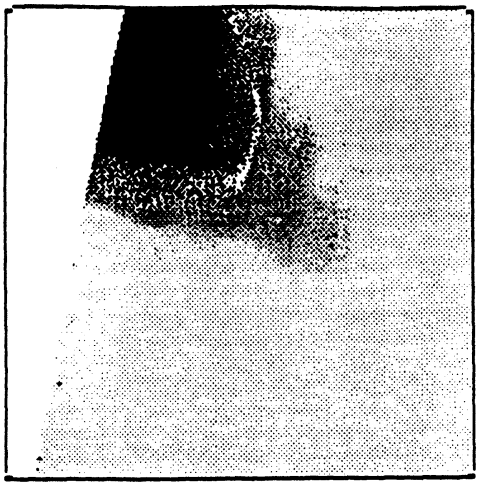

Fig. 10a

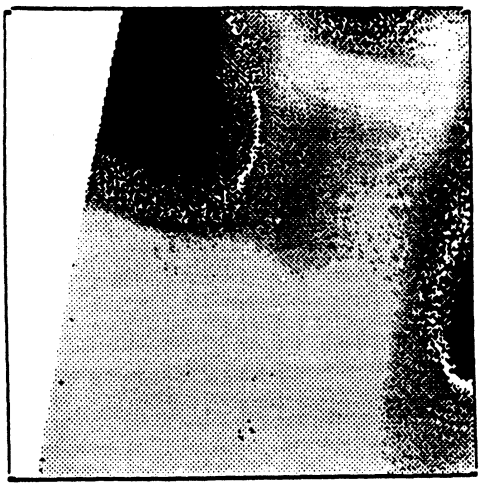

Fig. 10b

Fig. 10c

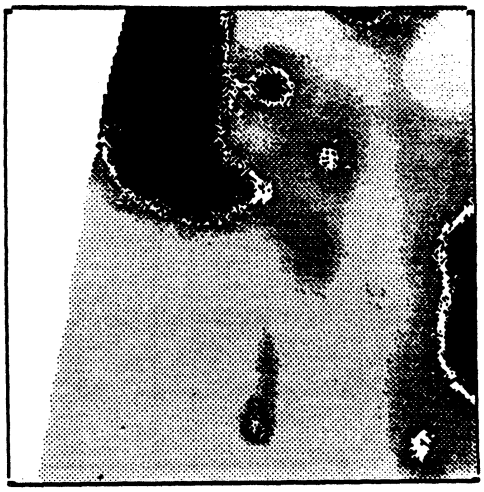

Fig. 10d

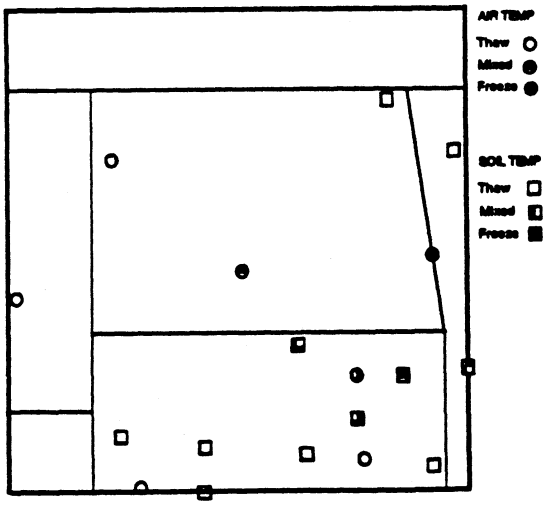

Fig. 10e

Fig. 10f

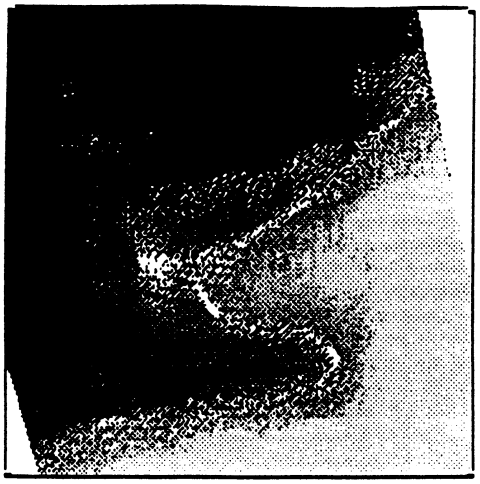

Fig. 11a

Fig. 11b

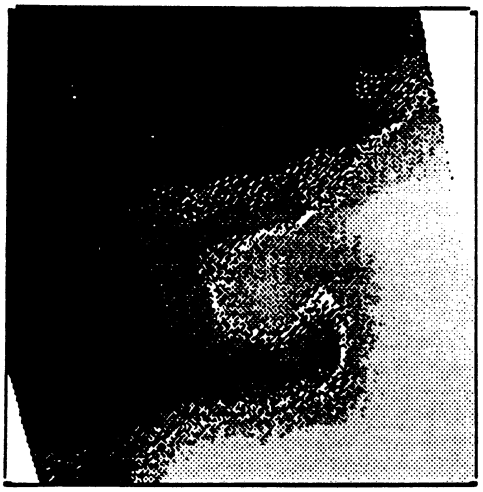

Fig. 11c

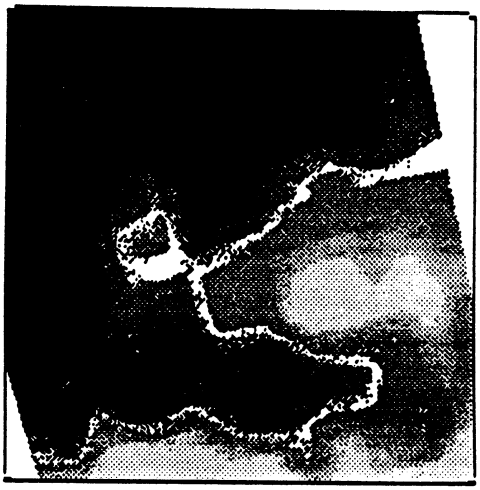

Fig. 11d

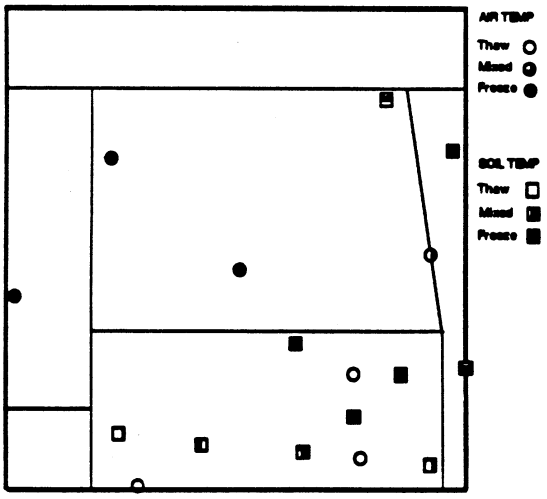

Fig. 11e

Fig. 11f

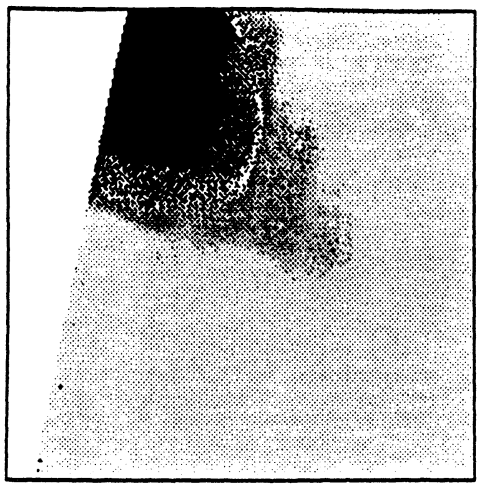

Fig. 12a

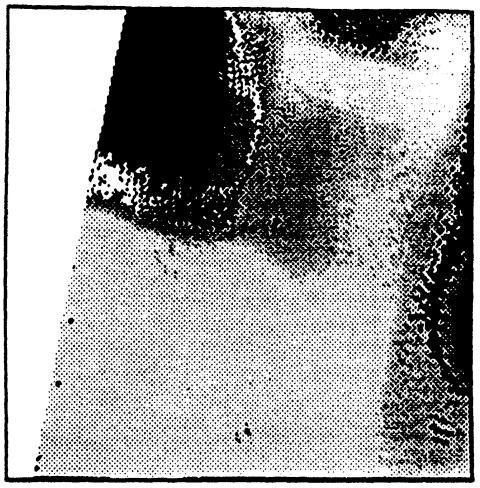

Fig. 12b

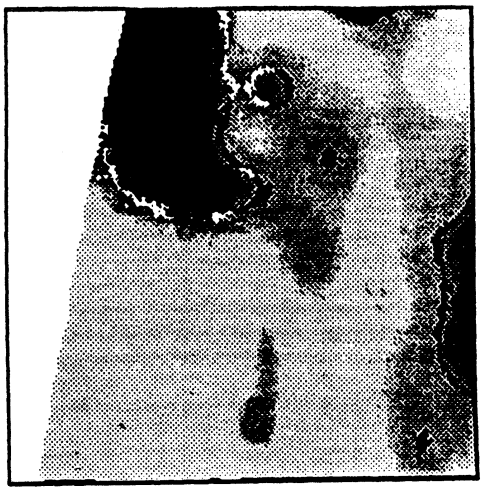

Fig. 12c

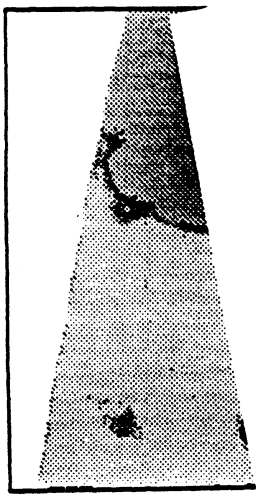

Fig. 12e

Fig. 12d

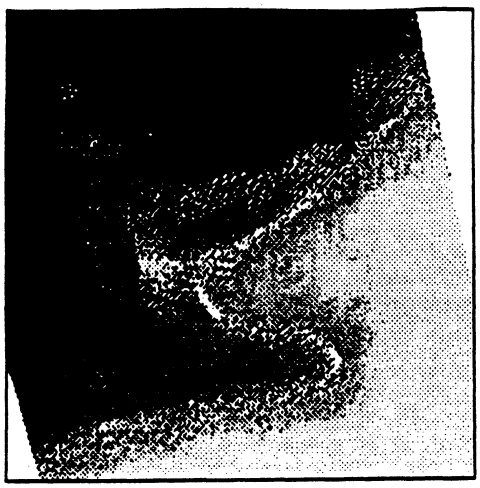

Fig. 13a

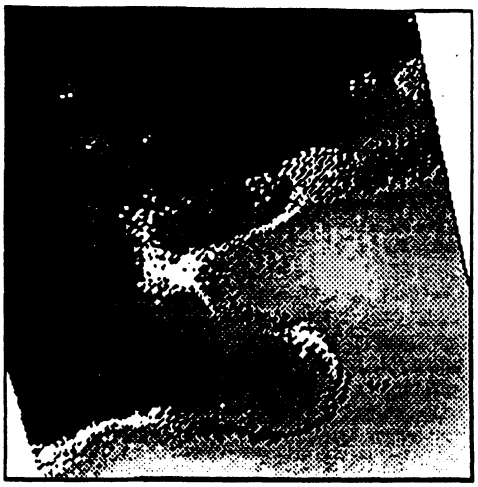

Fig. 13b

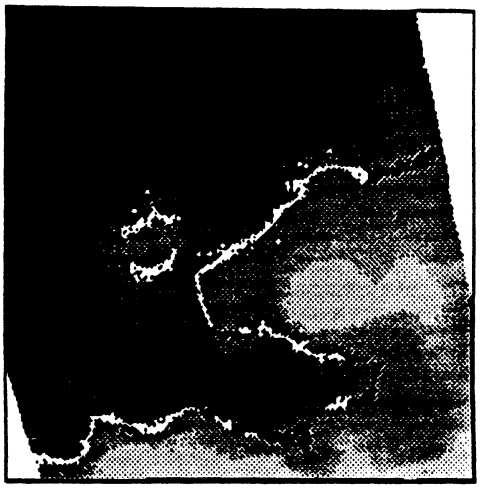

Fig. 13c

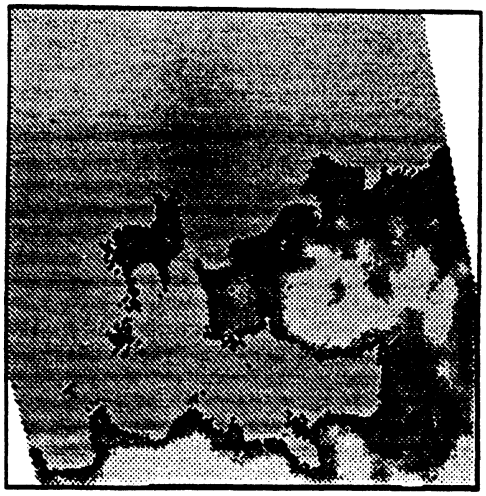

Fig. 13e

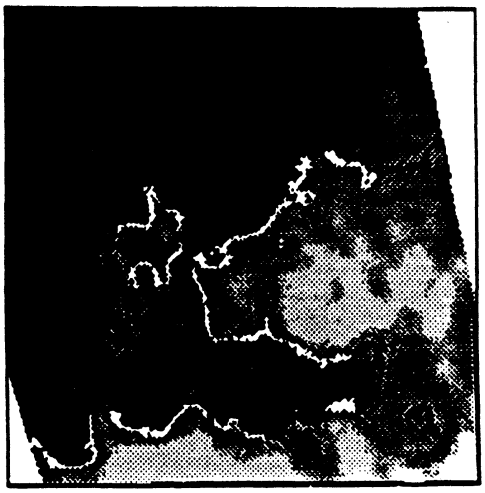

Fig. 13d

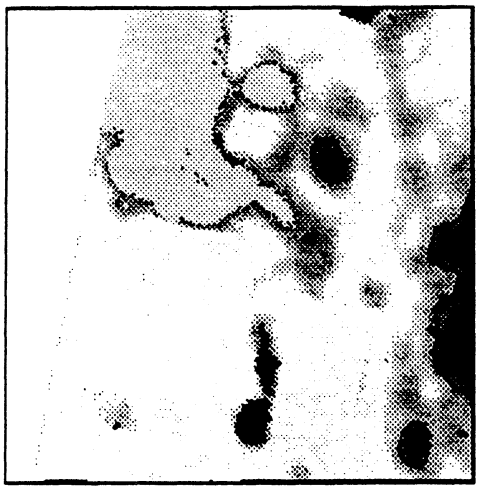

Fig. 14a

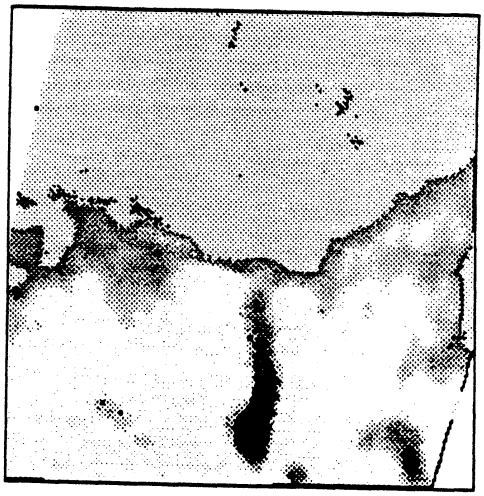

Fig. 14b

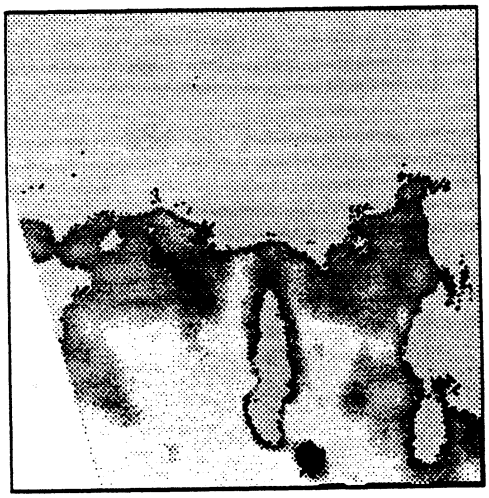

Fig. 14c

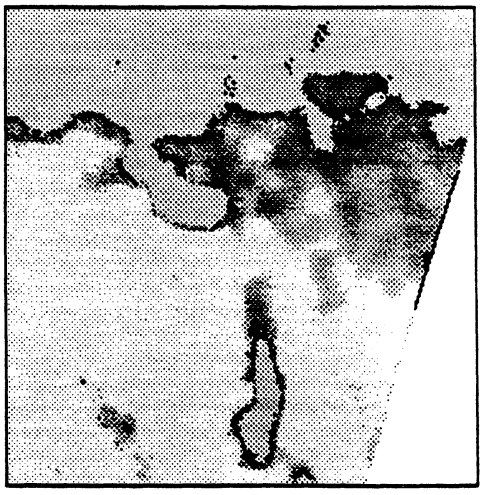

Fig. 14d

Fig. 14e

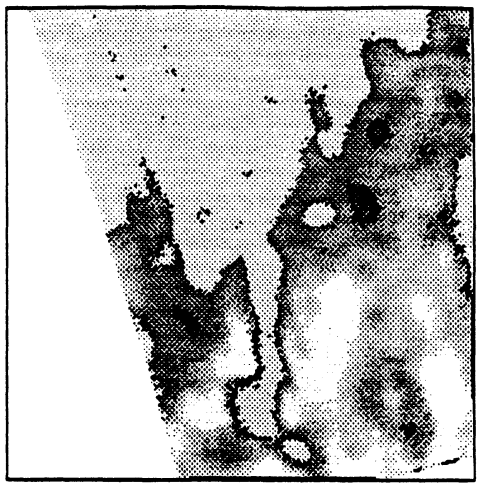

Fig. 14f

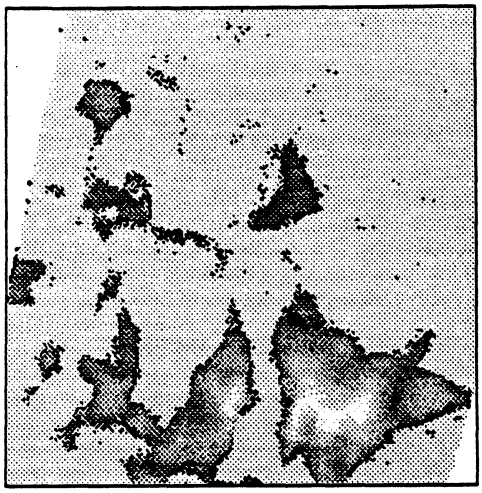

Fig. 14g

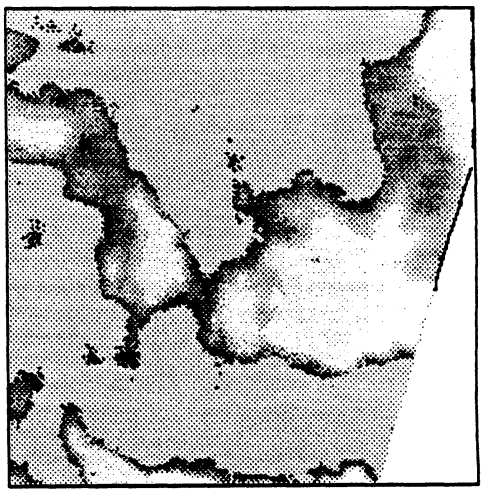

Fig. 14h

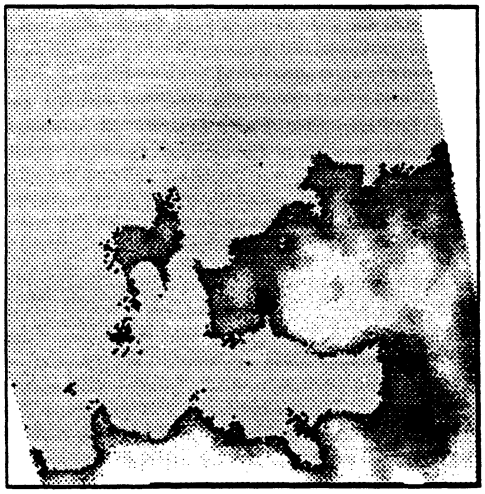

Fig. 14i

Proc. 1990 IEEE Int. Geosci. + Remote Sensing Symp. (IGARSS'90); College Park, MD

AN OPTIMIZED APPROACH TO MAPPING FREEZING TERRAIN WITH SMMR DATA

B. Zuerndorfer, A. W. England, F. T. Ulaby

Radiation Laboratory
Department of Electrical Engineering and Computer Science
The University of Michigan
Ann Arbor, MI 48109

Abstract-- A freeze indicator, based on a 37 GHz radiobrightness and a radiobrightness spectral gradient, has been shown to be an effective discriminant for classifying frozen surfaces [1] and in locating freeze/thaw boundaries [2]. The performance of this discriminant depends upon the accuracy with which decision boundaries can be established in decision space. In this paper, we show that decision boundaries that are based upon clustering and unsupervised classification yield good performance.

INTRODUCTION

Soil moisture contributes to the energy exchange between the air and the ground through latent heats of fusion and vaporization. Consequently, the processes of thawing frozen ground or of evaporating soil moisture cause soil thermal inertias to appear anomalously high. There is a large body of literature about deriving soil moisture from radiobrightness [e.g., 8,9]. Moisture state can also be inferred from radiobrightness [1]. Frozen soil classification is based upon a combination of 37 GHz radiobrightness and spectral gradient, $\partial T_b(f)/\partial f$, where $T_b(f)$ is the radiobrightness at frequency f. Frozen soils appear cold at 37 GHz, and exhibit a negative spectral gradient that is largely caused by volume scatter darkening at the shorter wavelengths.

This two parameter *freeze indicator* has been applied to data from the Scanning Multichannel Microwave Radiometer (SMMR) on Nimbus-7. For these data, the spectral gradient is a linear, least-square fit to the 10.7, 18, and 37 GHz radiobrightnesses. Conceptually, a surface is classified as frozen only if both the 37 GHz radiobrightness and the spectral gradient are sufficiently low. A *freeze map* is generated by displaying the freeze indicator for each pixel location. However, data processing is complicated by the very different spatial resolutions of the different SMMR frequency channels, and by differences between night and day SMMR radiobrightness measurements.

The different spatial resolutions of the SMMR channels require resolution compensation (equalization) to be performed prior to classification, so that spatial averaging is similar at all frequencies. Assuming that no a priori surface information is available, common practice for resolution compensation is to degrade the high frequency (fine-resolution) data to the resolution of the low frequency (coarse-resolution) data. As a result, fine-resolution information is lost. However, by using gaussian filtering in resolution compensation, the coarse-resolution freeze/thaw boundaries can be registered to fine-resolution 37 GHz boundaries (i.e., to 37 GHz radiobrightness threshold crossings) [2]. The fine-resolution, 37 GHz boundaries then provide improved location estimates of freeze/thaw boundaries.

Diurnal variations cause SMMR measurements of a single surface to be different at noon and midnight. For example, diurnal heating and cooling of the soil produce offsets in the measured spectral gradients between noon and midnight [3]. In addition, poorly compensated heating and cooling of SMMR by sunlight and Earth shadow may produce offsets in measurements made at noon and midnight [4]. Decision criteria for classifying soil, and identifying freeze/thaw boundaries, must accommodate these day/night differences.

In this paper, we show that frozen and thawed surfaces can be classified, and freeze/thaw boundaries located, through clustering and unsupervised classification. The procedure is "optimized" in the sense that noon and midnight SMMR measurements are clustered separately. Specifically, the 37 GHz radiobrightness and spectral gradient from SMMR measurements are grouped into frozen and thawed clusters for midnight and noon. The intersection of cluster regions for each time-of-day provides the necessary freeze/thaw boundary information to perform resolution extrapolation.

CLUSTER DATA

The data used for clustering was collected from August 1984 to December 1984 over a test area that includes North Dakota, about half of each neighboring state, and part of Canada. Unsupervised classification, rather than supervised classification, is used because of the dearth of accurate ground measurements in our test area. Supervised classification requires training with ground data as a reference [5]. The success of such training depends, in part, on the adequacy of the ground data. In our study, seven air temperature and eleven soil temperature recording sites provided the ground data for the entire test area. Soil temperatures were measured at 2 inches, or 5 cm, depth and were made at dawn and dusk, whereas SMMR overflights were at noon and midnight. The sparseness of ground sites and the differences between the times of soil temperature measurements and satellite overpasses precludes the ground data from being an accurate reference for the state of surface moisture in supervised classification training.

Data were selected from those SMMR satellite passes that covered more than 67% of the test area. Sixteen noon SMMR passes and thirteen midnight passes met this criterion during our August to December test period. The 18 and 37 GHz radiobrightness data were resolution compensated to the (coarser) resolution of the 10.7 GHz channel. The compensated surface data were re-sampled on a 97.5 Km grid (i.e., the resolution of the 10.7 GHz channel). Spectral gradients were computed as

CONCLUSIONS

We have shown that the separate clustering of SMMR noon and midnight data yields an optimized estimate of the location of freeze/thaw boundaries. While limited further improvements might be attained with more data in the scatter diagrams, significant improvements will depend upon better controlled air and soil temperature measurements.

REFERENCES

[1] Zuerndorfer, B.W., England, A.W., Dobson, C.M., and Ulaby, F.T. (1989); "Mapping freeze/thaw boundaries with SMMR data," *J. Agriculture and Forest Meteorology*; in press.

[2] Zuerndorfer, B.W., England, A.W., and Wakefield, G.H. (1989); "The radiobrightness of freezing terrain," *1989 IEEE Int. Geosci. and Remote Sensing Symp.*; Vancouver, Canada.

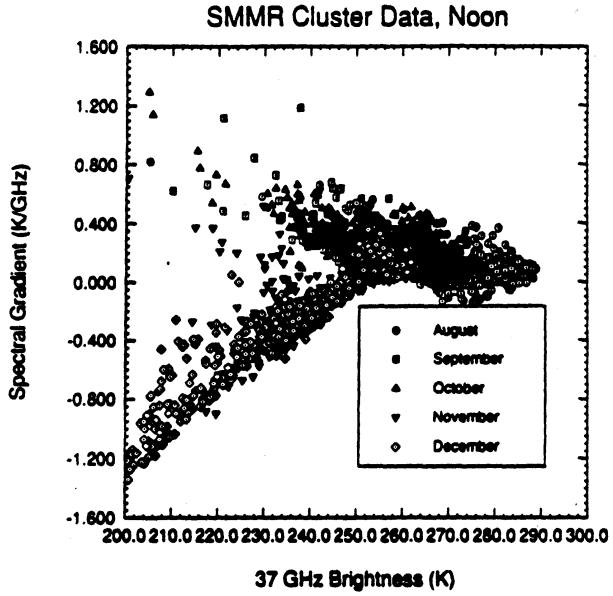

Figure 1. Scatter diagram of spectral gradient vs 37 GHz radiobrightness for noon SMMR data, 8/1/84-12/31/84.

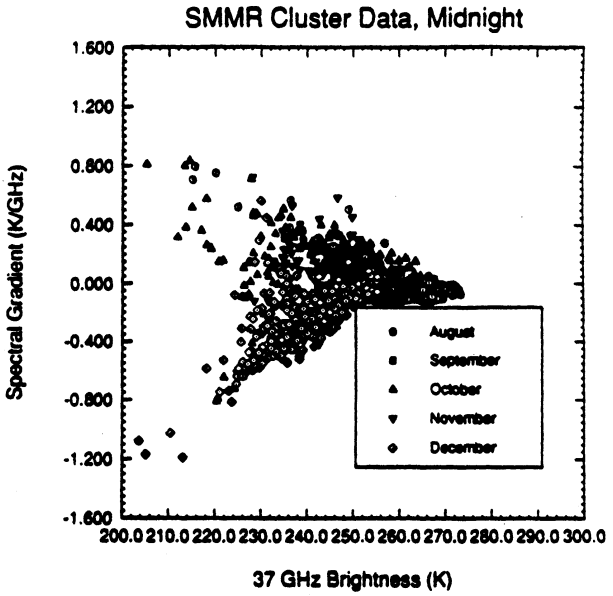

Figure 2. Scatter diagram of spectral gradient vs 37 GHz radiobrightness for midnight SMMR data, 8/1/84-12/31/84.

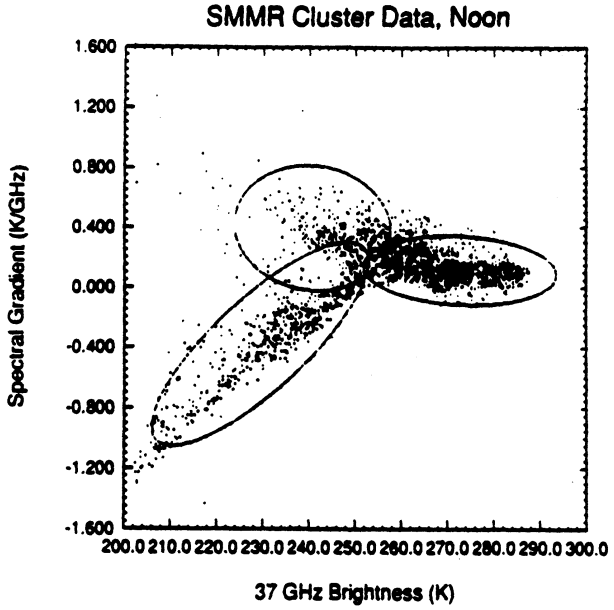

Figure 3. Single class ellipses for noon SMMR data, 8/1/84-12/31/84.

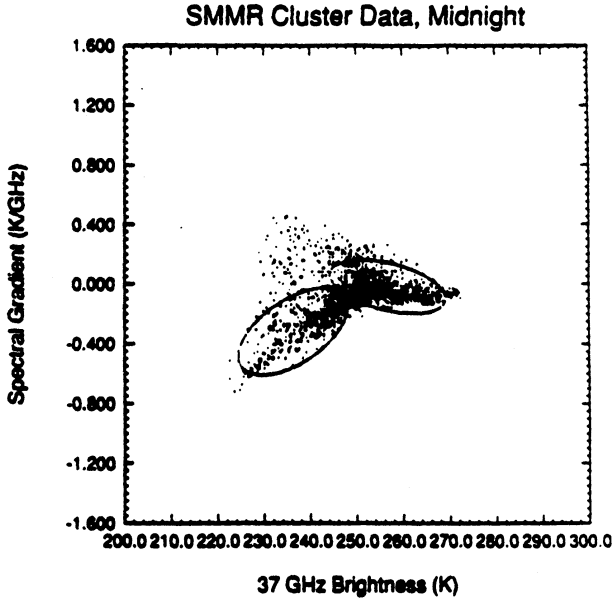

Figure 4. Single class ellipses for midnight SMMR data, 8/1/84-12/31/84.

Michigan Earth Grid version 1 (MEG1)
UNIFORM SPACING FORMAT
6/27/90

Characteristics:

1. MEG1 grid point spacing is uniform along rows of constant latitude and equals the spacing between rows, but individual points within each row and corresponding points in adjacent rows will not fall on a common meridian. That is, a simple rectilinear display of the data will not yield a Mercator-like image. Every useful display of the data will require a resampling program to map MEG1 into the desired projection.

2. MEG1 coordinates are designed to be nearly 25 km apart at the equator. 1/297 flattening of the oblate ellipsoidal Earth will render the grid points at the poles somewhat closer together.

3. MEG1 is based upon a polar, right-hand coordinate system with $\theta = 0$ the north pole, and $\phi = 0$ the 180^{o} meridian. The 180^{o} meridian was chosen because most people can visualize its location, and because this seam in our grid does not cross a major land mass. The first point in each row will be on the 180^{o} meridian, and successive points will progress toward the east (right-hand system). The spacing between the last point in a row and the first will vary between 0 and 25 km among rows. This will result in a ragged seam along the 180^{o} meridian.

4. Assuming an equatorial radius of 6,378.388 km, the Earth equatorial circumference is 40,076.594 km. A 25 km spacing yields 1604 grid points (including the zero point). We suggest that this be rounded to 1600 equally spaced points which yields a 25.048 km spacing along the equator. If M_{400} is number of points on the equatorial row (designated row n = 400), and m is the individual point designation, then $0 <= m < M_{400} = 1600$. For other than the equatorial row, $M_n = M_{400} - INT[M_{400}(1-\sin \theta_n)] = - INT[- M_{400} \sin \theta_n]$, where $\theta_n = \pi (n/800)$ radians (effectively the complement of latitude), and function INT means the largest integer that is less than or equal to the argument. Note that under this scheme, the pole rows are null sets.

6. We chose an identical spacing between rows so that, if N is the number of rows, N = 801, and, if n is the row number, $0 <= n <= 800$, n = 0 is the north pole, n = 400 is the equator, and n = 800 is the south pole.

7. The location of each MEG1 point, P_{nm}, is uniquely mapped from nm to lat-lon by:

$$Lat(P_{nm}) = 90\ (\ 1 - n/400),\ \text{degrees N if} > 0,\ \text{degrees S if} < 0.$$

$$Lon(P_{nm}) = 180\ (1 - 2m/M_n),\ \text{degrees W if} > 0,\ \text{degrees E if} < 0.$$

These equations can be inverted to provide a unique mapping from lat-lon to nm.

8 Assuming an 8 byte word per grid point for each satellite pass (7 bytes for the brightness channels and 1 byte for a time tag), and that we record at least 2 passes per day, then there are 16 bytes associated with each grid point per day. Total bytes per day becomes: 16 x N_{tot} where N_{tot} is the total number of grid points in MEG1. For an Earth's radius at the equator of r = 6,378.388 km, N_{tot} can be approximated:

$$N_{tot} = \frac{\text{approx. area of Earth's surface}}{\text{area associated with each grid point}}$$

$$= \frac{4\pi r^2}{25.048^2}$$

$$= \frac{4\pi\ 6378.388^2}{627.402}$$

$$= 814{,}865 \text{ grid points}$$

That is, the total daily byte requirement becomes: 16 x 814,865 = 13.038 Mbytes/day. If a CD holds 650 Mbytes, then 1 CD covers about 50 days. If northern and southern hemisphere data are produced on separate disks, and with some data compression so that null data (gaps of no coverage or 1 pass coverage) do not take up the full 16 byte allotment for each grid point, then it seems reasonable that 4 months of 1 satellite, two pass coverage could be recorded on 1 CD using the MEG1 format.

MEG1

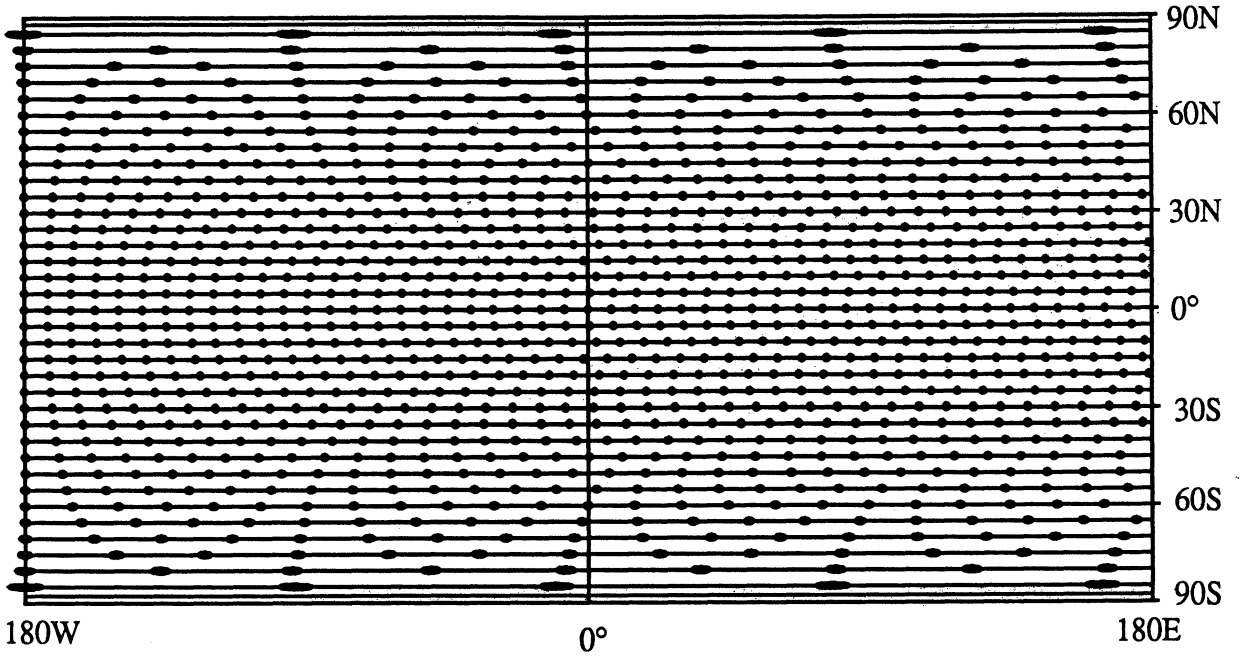

Example grid points.

Michigan Earth Grid version 4 (MEG4)

MERCATOR-LIKE FORMAT

6/28/90

Characteristics:

1. MEG4 coordinates are along constant latitude and longitude.

2. MEG4 coordinates are designed to be nearly 25 km apart at the equator. 1/297 flattening of the oblate ellipsoidal Earth will render the meridional grid points at the poles somewhat closer together. The density of grid points along a constant latitude decreases by 1/2 above 60^{o} N and S (cos 60 = 0.5) and again by 1/2 above 75^{o} N and S (cos 75 = 0.26) to limit the oversampling. These shift locations are convenient because Alaska falls almost entirely within the 60^{o}-75^{o} range, and 60^{o} N is a major division among the Canadian Provinces. There are no grid points above 87.6^{o} degrees latitude because the SSM/I does not cover the last 2.4^{o}.

3. MEG4 is based upon a polar, right-hand coordinate system with $\theta = 0$ the north pole, and $\phi = 0$ the 180^{o} meridian. The 180^{o} meridian was chosen because because most people can visualize its location, and because this seam in our grid does not cross a major land mass.

4. Point spacing is based upon the equatorial radius of 6,378.388 km and an equatorial circumference of 40,076.594 km. A 25 km spacing yields 1603.06 grid points. To preserve a simple relationship with the degree (assuming we don't want to use grads), we can resample either at 1/4 degree (15 minute) intervals which yields 1440 points at 27.831 km spacing at the equator, or at 1/5 degree (12 minute) intervals which yields 1800 points at 22.265 km spacing at the equator. We chose a hybrid of 15 minute sampling along constant latitude and 12 minute sampling along the meridians. This means that the aspect ratios of the latitude and longitude spacing between sample points are equal at 36^{o}, 66^{o}, and 78^{o} N and S latitude which permits easy, natural looking projections at these latitudes from MEG4 without resampling.

5. Rows in our grid are along circles of constant latitude. The first point in each row is on the 180^{o} meridian, and successive points progress toward the east (right-hand system). Between 0^{o} and +/-60^{o} latitude, there is 15 minute-of-longitude sampling so that $M_{<60}$ =

1440 points per row. Between +/-60° and +/-75° latitude, there is 30 minute-of-longitude sampling so that $M_{60\text{-}75} = 720$ points per row. Above +/-75° latitude, there is 1 degree-of-longitude sampling so that $M_{>75} = 360$ points per row. In each row, the point designation, m, spans the range $0 <= m < M_x$: x = <60, 60-75, >75.

6. We chose 12 minute-of-latitude spacing between rows so that, if N is the number of rows, N = 901, and, if n is the row number, 0 <= n<= 900, n = 0 is the north pole, n = 450 is the equator, and n = 900 is the south pole. Because the Defense Meteorological Satellites don't actually fly over the poles, the actual range of n would be 12 <= n <= 888, which corresponds to the highest latitude row being 2.4° from the poles.

7. Therefore, the location of each MEG point, P_{nm}, is uniquely mapped from nm to lat-lon by:

$Lat(P_{nm}) = 90 (1 - n/450)$, degrees N if > 0, degrees S if < 0.

$Lon(P_{nm}) = 180 (1 - m/720)$, degrees W if > 0, degrees E if < 0, for 150 <= n <= 750.
$Lon(P_{nm}) = 180 (1 - m/360)$, degrees W if > 0, degrees E if < 0, for 75 <= n < 150 & 750 < n <= 825.
$Lon(P_{nm}) = 180 (1 - m/180)$, degrees W if > 0, degrees E if < 0, for 12 <= n < 75 & 825 < n <= 888.

Each of these equations can be inverted to provide a unique mapping from lat-lon to nm.

8. Assuming an 8 byte word per grid point for each satellite pass (7 bytes for brightness channels and 1 byte for a time tag), and that we record at least 2 passes per day, then there are 16 bytes associated with each grid point per day. Total bytes per day becomes:

150 <= n <= 750:	16 x 1440 x 601	=	13.847 Mbyte/day
75 <= n < 150 & 750 < n <= 825:	2 x 16 x 720 x 75	=	1.728 Mbyte/day
12 <= n < 75 & 825 < n <= 888:	2 x 16 x 360 x 63	=	0.726 Mbyte/day
	TOTAL	=	16.301 Mbyte/day

If a CD holds 650 Mbytes, then 1 CD covers about 40 days. If northern and southern hemisphere data are placed upon separate disks, and if some efficiency is realized by, e.g., compressing null data (gaps of no coverage or 1 pass coverage where all 16 bytes are not required), then it should be possible to store 3 months of daily, two-pass data from one satellite on one CD. If two satellites are active, there might be separate disks for each satellite.

MEG4

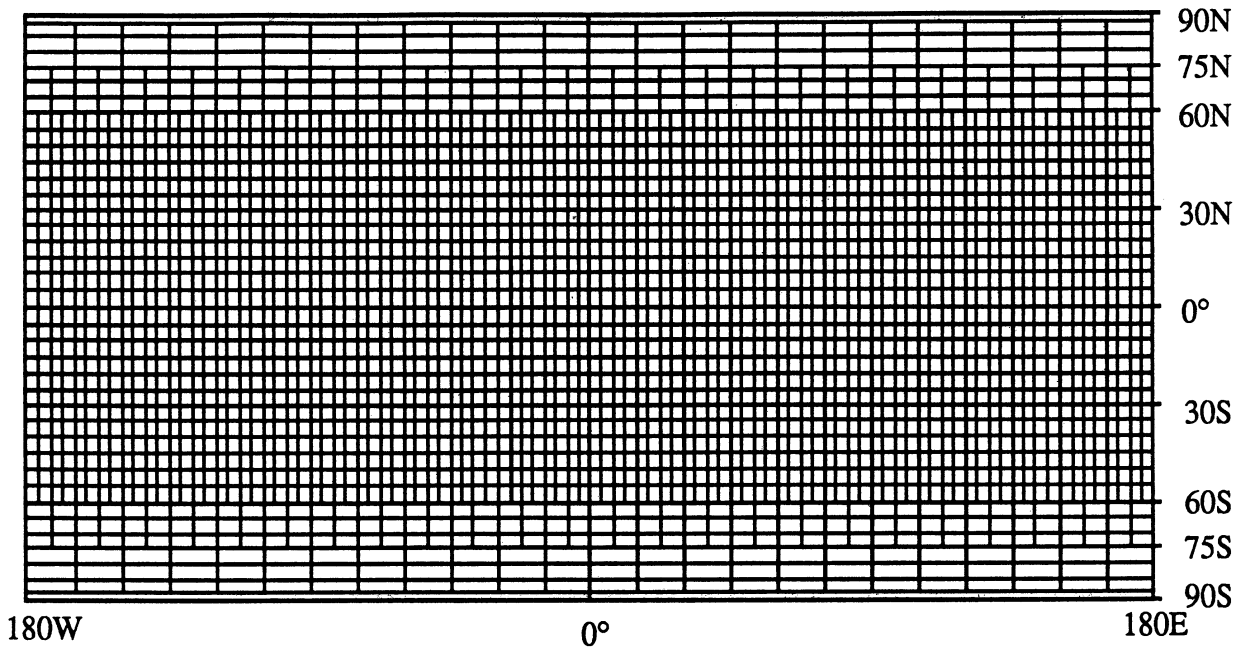

Example grid points lie at line intersections.